Sede Amministrativa Università degli Studi di Padova
Dipartimento di INGEGNERIA INDUSTRIALE

CORSO DI DOTTORATO DI RICERCA IN INGEGNERIA INDUSTRIALE
CURRICULUM INGEGNERIA MECCANICA
CICLO XXXIV

Severe plastic deformation by backward tube flowforming

Coordinatore: Ch.mo Prof. Giulio Rosati

Supervisore: Ch.mo Prof. Andrea Ghiotti

Dottorando: Tommaso Magro

Acknowledgements

In some moments the end of this experience seemed a mirage, however, this day has arrived: writing these sentences of thanks is the final touch of my thesis. It was a time of profound learning, not only on a scientific level but also on a personal level. I would like to say a few words of thanks to all the people who have supported and helped me during this period.

I would like to thank Prof. Ghiotti and Prof. Bruschi who gave me the chance to enter in the PhD program, believing in my contributions. I thank them for the support to both my researches and my professional growth, and their valuable life lessons, without which this work would most likely not have come to an end.

Federica, you have been close to me in difficult moments, encouraging me to leave no stone unturned and rejoicing with me in the happy moments encountered during this journey. Feel part of this life milestone, hoping that we can share many more together.

I would like to thank my family: your wise advice has made me understand what really matters, you have given me a different perspective, teaching me that even when everything seems to go wrong there is always at least one reason to be happy.

Mattia, we could have made this journey together, but you had the courage to be honest: I can only tell you that you have been an excellent companion on the adventure, from the first day we sat together. Matteo, you know the esteem I have towards you, I thank you for your precious advice and your vision of things. I hope you will both be a reference as you have been up to now. When we grow up we understand who really matters, I believe that there will never be a shortage of things to tell us in front of a mug of beer.

Finally, I thank myself for having just the right amount of insanity to do all of this.

Abstract

Tailored components are increasingly used in modern industry, as they allow the exploitation of key properties, such as strength, thickness, corrosion protection, type of material, in specific areas of interest of the workpiece, removing the weight where not necessary for performance purposes. It is possible to use a class of processes called "Severe Plastic Deformation" to modify some of these properties. Through the considerable refinement of the crystalline grain resulting from the high plastic deformation to which the component is subjected, not only does the resistance of the material increase, but also decreases the presence of internal defects, and consequently increases the fatigue resistance. The smaller dimensions of the crystalline grain are finally linked to a higher resistance to corrosion.

These processes, developed by the most common massive deformation processes such as extrusion, torsion, bending, rolling, are subject to various critical issues, including the laboratory-scale dimensions of the components that can be produced, resulting in poor industrial applicability, the problematic design and implementation of the process, and finally the high costs. From a review of the literature, it was possible to identify some critical points of scientific interest, first of all, the need to develop a process that at the same time guarantees a double objective: to obtain a component with high mechanical characteristics, typical of SPD processes, but with of suitable dimensions for possible use on an industrial scale. To implement a similar approach, attention was focused on the tube flowforming process, also known as tube spinning, which is generally not included among the SPD processes. However, since there are many elements in common (high refinement of the crystalline grain, absence of internal defects, high plastic strain), it was decided to use this technique to obtain two different types of products. The first is a tubular element, very difficult to make at present given the buckling and sticking problems, while the second type of product that can be obtained is a flat element, characterized by the same properties of the tubular component, obtained after cutting and straightening conducted on the tube.

The purpose of this PhD thesis is to evaluate the feasibility of using the backward tube flowforming process to obtain tailored SPD components, thus assessing the influence of various process parameters both numerically and experimentally in some of the properties of the final component. To this end, two different equipment have been developed to perform the experimental tests, a traditional one, designed starting from the peculiar characteristics of the process available in the literature and simulated numerically, and an innovative equipment that uses a constraint placed radially to the tube, helpful in increasing the strain imposed during the process and improving the surface quality of the final component.

The experimental tests, carried out using the AA6082-T4 alloy as reference material, allowed us to evaluate the variations in the mechanical characteristics of the starting material, reporting a high increase in microhardness and mechanical properties intended as yield strength and UTS. At the same time, following the theoretical result that associates an increase in mechanical performance with a decrease in the size of the crystalline grain, there was a high reduction in the size of the crystalline grain, with a portion of the tube characterized by a structure with microstructure highly refined, typical of SPD processes. The high deformation impressed on the tubular elements led to a reduction in ductility, which in any case did not affect the execution of the flattening process performed downstream of the flowforming process, allowing to obtain plates characterized by the same microstructure and mechanical characteristics of the initial flowformed tube.

Sommario

L'utilizzo di componenti progettati "su misura" trova sempre più spazio nell'industria moderna, poiché il loro impiego permette di sfruttare delle proprietà chiave, quali resistenza, spessore, protezione dalla corrosione, tipologia del materiale, in specifiche aree di interesse del pezzo, rimuovendo il peso dove non necessario ai fini prestazionali. Per modificare alcune di queste proprietà è possibile utilizzare una tipologia di processi denominata "Severe Plastic Deformation". Tramite il notevole raffinamento della grana cristallina conseguente all'elevata deformazione plastica a cui il componente è soggetto non si va solo ad aumentare la resistenza del materiale, ma si va anche a diminuire la presenza di difetti interni, e conseguentemente ad aumentare la resistenza a fatica. Le dimensioni inferiori della grana cristallina sono infine collegate ad una più elevata resistenza alla corrosione.

Questi processi, sviluppati partendo dai più comuni processi di deformazione massiva quali estrusione, torsione, piegatura, laminazione, sono soggetti a diverse criticità, tra cui: le dimensioni su scala di laboratorio dei componenti che possono essere prodotti, con conseguente scarsa applicabilità industriale, la difficile progettazione e realizzazione del processo, e infine i costi elevati. Da una revisione della letteratura è stato possibile individuare alcuni punti critici di interesse scientifico, primo tra tutti l'esigenza di sviluppare un processo che allo stesso tempo garantisce un obiettivo duplice: ottenere un componente con caratteristiche meccaniche elevate, tipico dei processi SPD, ma con delle dimensioni idonee ad un eventuale utilizzo su scala industriale. Per attuare un simile approccio l'attenzione è stata focalizzata sul processo di tube flowforming, conosciuto anche con il nome di tube spinning, che generalmente non si annovera tra i processi SPD. Essendo tuttavia molteplici gli elementi in comune (elevato raffinamento della grana cristallina, assenza di difetti interni, elevata deformazione plastica) si è deciso di utilizzare questa tecnica per ottenere due diverse tipologie di prodotto. Il primo è un elemento tubolare, molto difficile da realizzare allo stato attuale visti i problemi di buckling e sticking, mentre il secondo tipo di prodotto ottenibile è un elemento piatto, caratterizzato dalle stesse proprietà dell'elemento tubolare, ricavato dopo le operazioni di taglio e spianatura condotte sul tubo.

Lo scopo di questa tesi di dottorato è quello di valutare la fattibilità nell'utilizzo del processo di backward tube flowforming per ottenere componenti con microstruttura raffinata creati "su misura", valutando quindi sia a livello numerico sia a livello sperimentale l'influenza di vari parametri di processo su alcune delle proprietà del componente finale. A tal fine per eseguire le prove sperimentali sono state sviluppate due diverse attrezzature, una tradizionale, progettata partendo dalle

caratteristiche peculiari del processo reperibili in letteratura e simulate numericamente, ed un'attrezzatura innovativa che utilizza un vincolo posto radialmente rispetto al tubo, utile per aumentare la deformazione impressa durante il processo e per aumentare la qualità superficiale del componente finale.

Le prove sperimentali, condotte utilizzando come materiale di riferimento la lega di alluminio 6082-T4, hanno permesso di valutare le variazioni delle caratteristiche meccaniche del materiale di partenza, riportando un elevato incremento di durezza e delle proprietà meccaniche intese come limite di snervamento e UTS. Allo stesso tempo, in accordo con il risultato teorico che associa un incremento di prestazioni meccaniche con un decremento della dimensione del grano cristallino, si è avuta un'elevata riduzione della dimensione del grano cristallino, con una porzione di tubo caratterizzata da una microstruttura altamente raffinata, tipica dei processi SPD. L'elevata deformazione impressa sugli elementi tubolari ha comportato una riduzione della duttilità, che comunque non ha influito sull'esecuzione del processo di spianatura eseguito a valle del processo di flowforming, permettendo di ottenere piatti caratterizzati dalla stessa microstruttura e caratteristiche meccaniche del tubo flowformato di partenza.

Tables of Contents

Part 1: Introduction

Chapter 1

Introduction

1.1 The industrial problem

A growing concern in the manufacturing industry's automotive, aerospace and biomedical segments is to efficiently build components with custom-designed and optimized properties as their prerogative, with homogeneous distribution in particular component areas. To this end, techniques have been developed over the years to manufacture tailored semi-finished parts, which are typically characterized by the presence of different alloys, thicknesses, coatings, or material properties. On the other hand, through Severe Plastic Deformation techniques, it is possible to increase the mechanical characteristics of the components acting on the material's microstructure. Using particular setups, and based on the presence of high hydrostatic stresses, these techniques reduce the grain size, increasing at the same time, following the Hall-Petch relationship, the mechanical characteristics of the material, and augmenting other properties, such as fatigue life or corrosion resistance.

The combination of these two manufacturing principles could lead to the achievement of benefits in different fields, depending on the functionality needed. Considering automotive or aerospace sectors, components with higher mechanical properties or higher stiffness allow lower cross-sections or to use a different shape, increasing the strength-to-weight ratio. In this way, strength can be concentrated where it is most needed, while more ductile materials can be used in the same part to control deformation, for example, in structural elements stressed during an accident. As a result, overall material thickness is reduced, decreasing weight and emissions. In the biomedical field, prostheses with tailored properties guarantee the use of bioabsorbable and biocompatible materials instead of permanent implants. The traditional currently used solution requires a second surgery, with adverse effects on

the well-being of patients and additional costs for healthcare. In contrast, a tailored solution allows you to define a personalized useful life, with properties that vary over time, such as corrosion resistance. In this way, the component, characterized by a microstructural gradient and consequently a variable corrosion resistance, varies its thickness over time, compensating for the lower load required due to the reconstitution of the bone part.

Although the tube flowforming is usually not part of the so-called SPD processes and the tailored components, it is possible to find some similarities. Considering the characteristics of the SPD techniques, in common, there are a high reduction in grain size, an increase in mechanical characteristics, a reduction in mechanical defects, porosities, and cracks. Considering the tailored components instead, it is possible to obtain tubes with variable thickness and mechanical properties, allowing obtaining tailored panels. However, a further aspect that is often not considered is the size of the component that can be obtained: generally, these refining processes allow obtaining laboratory-scale components, which are rarely used in manufacturing applications. The flowforming process, on the other hand, allows for larger parts to be obtained due to the characteristics of the process, which will be described in detail in the following Chapters.

1.2 Scientific relevance

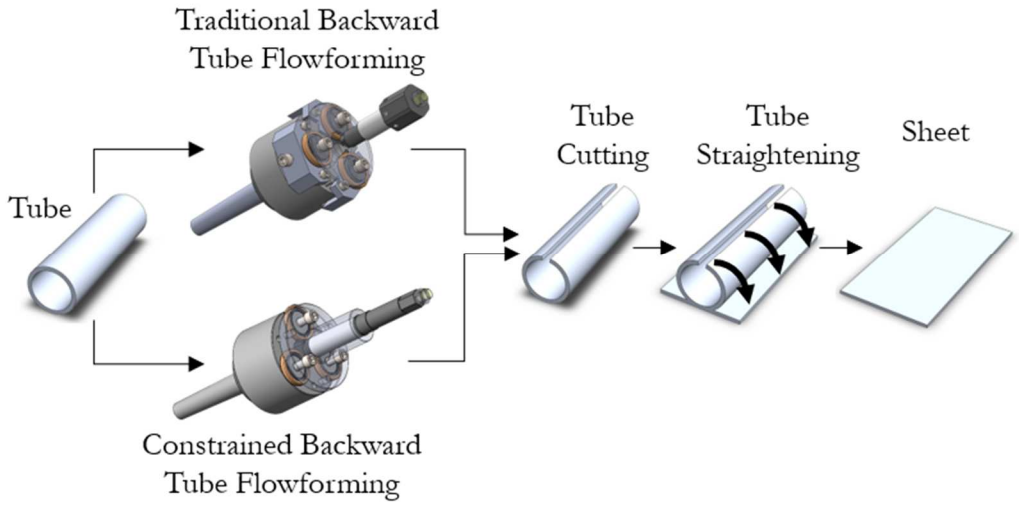

Fig. 1.1 *- Process chain.*

The aim of this research project, therefore, does not focus on the single flowforming process, being the state of the art known and developed over the years, but focuses on innovative use of the product that can be obtained through this process, developing a new process chain for the economical and reliable production of large size metal sheet parts with accurate control of their properties during the product

service-life.

The idea is to use a traditional and innovative version of the backward tube flowforming process to tune the material microstructure of thin-walled tubes and obtain sheet panels by longitudinal cutting of the obtained tubes and subsequent incremental flattening operations, as reported in Fig. 1.1. A further advantage of this conceptual process chain would be represented by the possibility to control the anisotropy and the grain size across the tube wall thickness to vary the required properties, such as the surface microhardness, the chemical resistance, etc.

In this work, aluminium AA6082-T4 alloy was used to exploit its formability and have not too high loads in executing the flowforming process. However, this process chain can be applied to different materials (Al, Zn, and Mg alloys) to obtain different properties on the final components, both as regards tubular components (Fig. 1.2a) and as regards sheet metal workpieces (Fig. 1.2b).

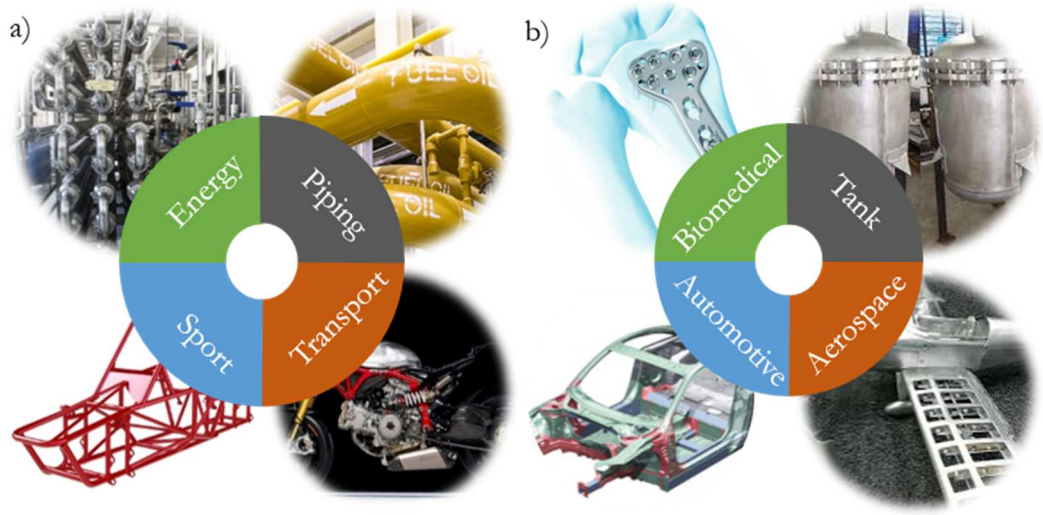

Fig. 1.2 *- Possible use of a) a tailored tube and b) a tailored sheet.*

As for the use of the flowformed tube, it can be adopted in different sectors, which can be, for example, the energy sector in parts of heat exchangers, that of piping, to increase the mechanical characteristics of the tubes and ensure greater sealing, in sport and transport sectors, to improve the stiffness or the fatigue resistance of trellis frames, also having the possibility to vary the cross-section of the component. As regards the use of sheets deriving from flowformed tubes, also in this case, there can be several applications. In the automotive and aerospace sectors, for high-strength panelling, to create lighter structures and at the same time more rigid and more resistant, but also in the biomedical industry, for biodegradable prostheses obtained with materials that otherwise would have unsatisfactory mechanical characteristics, like zinc. By taking advantage of the lower presence of cracks, porosity, and microstructural defects, further use can be in pressurized tanks.

1.3 Research objectives

As previously described, innovative use and a modified version of a traditional process like the tube flowforming may be modifying the characteristics of the products to a different extent. However, a link between process parameters and mechanical properties is greatly needed. This research is an attempt to address these concerns, and its principal objectives are:

- Apply innovative manufacturing techniques such as the constrained flowforming or traditional ones like the flowforming to manufacture tailored components with improved characteristics;
- Investigate the effect of different process parameters on microstructure, microhardness, elongation, etc., induced by these manufacturing operations.

As the flowforming is a non-linear plastic deformation process, a finite element method is required to predict the stress state and the strain distributions during the process for efficient and successful product manufacturing. The FE model allows for the investigation of the influence of different process parameters on the material properties, optimizing the setup in terms of geometry and kinematic to obtain the desired characteristics.

Considering the process chain shown in Fig. 1.1, it was decided to focus the activities on the traditional and constrained backward tube flowforming for two reasons: the first one is related to the larger economic value these processes give to the workpiece, while the second reason is related to a technical aspect. Although geometrically there are considerable differences between the flowformed tube and the sheet obtained by straightening, it was demonstrated that the mechanical behaviour of the flowformed tube is very similar to the sheet obtained in the last step.

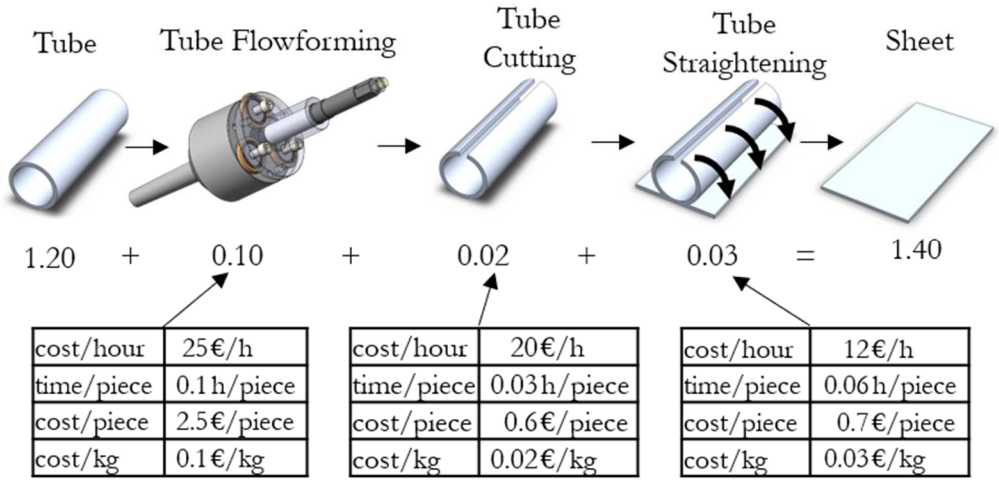

Fig. 1.3 *- Changes in the economic value along the process chain.*

From an economic point of view, the process chain could be reasonable only if the mechanical and chemical properties of the final component are better than the properties of a sheet with the same geometrical characteristics. Comparing the value of an extruded tube and a plate, it is possible to notice how the average value of the first is about 1.10-1.20 times the value of the sheet. This calculation considers different materials, like aluminium, steel, Inconel, and nickel, comparing the cost per kilogram. In addition, several manufacturing operations need to be carried out on the sheet produced with the process chain, increasing the component's value. It is possible to estimate an increase of the sheet value obtained through this process chain of +20%, and consequently at least 1.4 times if compared with a commercial sheet, as reported in Fig. 1.3, considering the AA6082 alloy as the reference case.

1.4 Overview of the dissertation

Fig. 1.4 shows how this work is organized in five parts, which in turn are subdivided into eight Chapters.

The first part is the current Chapter entitled *"Introduction"*. Therefore it is not included in the flow chart.

Chapter 2 composes the second part, *"State of the art"*, in which a literature review is presented. The major experimental studies that deal with the Severe Plastic Deformation processes are described. In addition, the few available studies on the effect of the material grain refinement induced by the flowforming process on the material properties are reported.

The third part, *"Material and methods",* comprises four Chapters, namely 3, 4, 5, and 6. In Chapter 3, the characteristics of the material under investigation in this research work, namely aluminium AA6082-T4, are described. Besides general information, attention was paid to highlight concerns related to their functional performances. Chapter 4 summarizes the influence of the process parameters on the strain distributions, the axial loads, and the geometrical variations of the tube, in particular the effects of the geometrical and kinematics process parameters, using numerical simulations. In Chapter 5, an overview of two different experimental equipment used to carry out flowforming experiments is presented. In particular, the backward tube flowforming setup and the constrained backward tube flowforming setup are described in detail, starting from the results achieved in Chapter 4. Chapter 6 deals with the description of the measurements carried out to assess the properties of the flowformed workpiece. These mechanical properties measurements include analysis of microstructures, microhardness evaluation strategies, tensile tests, and geometrical properties examination.

The fourth part, *"Results and discussion",* is composed of one Chapter, namely 7. The experimental results obtained using the traditional and the constrained backward tube flowforming are described and compared, associating the numerical results with

the experimental results.

Solely Chapter 8 composes the fifth part, *"Conclusions"*. In this Chapter, the findings and results of the current work are summarized with final remarks and conclusions. The directions of the future work are discussed briefly based on the results and observations presented in this dissertation.

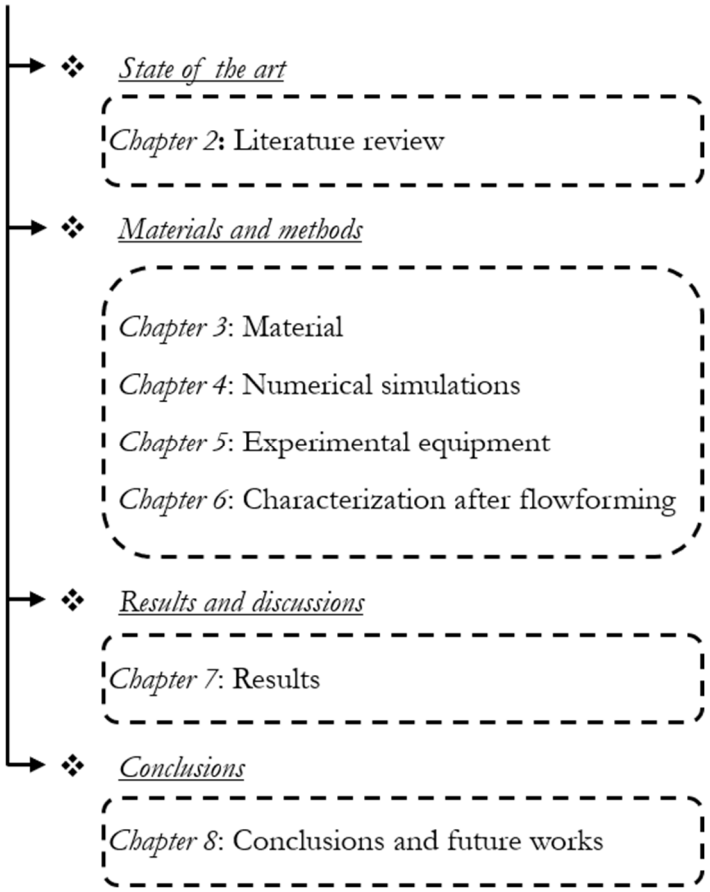

Fig. 1.4 *- Flow chart of this PhD essay.*

Part 2: State of the art

Chapter 2

Literature review

The first part of this Chapter reports the peculiar characteristics of the most important SPD techniques, describing different processes and analysing the main limitations of these methodologies. This state-of-the-art analysis is not intended to be exhaustive but aims to describe the critical points of the various methodologies and the benefits that SPD processes can bring. The parameters that are generally analysed to determine if the SPD methods have been effective are described below. The second part of this Chapter refers to the description of the state of art related to the flowforming process, also comprehending an overview of the few studies related to the influence of the flowforming process on the functional performances of the workpiece. The literature analysis concerning the numerical simulations of the flowforming process instead has been reported in Chapter 4.

2.1 Fundamentals of Severe Plastic Deformation

The well-known Hall-Petch [1] relationship, developed in the 1950s, establishes that the inverse square root of the grain size *d* in the polycrystalline materials is related to the yield stress of the metals σ_Y at room temperature, according to the Eq. 1:

$$\sigma_Y = \sigma_0 + \frac{K}{\sqrt{d}} \qquad \textit{Eq. 1}$$

where σ_0, the friction stress, represents the resistance to dislocation motion in the grain interior and *K* measures the local stress needed to initiate plastic flow [2]. Due to the inverse relationship between the grain size and the yield stress, and consequently the smaller the grain size, the higher the yield stress, it could be thought that infinitely reducing the grain size would significantly influence the mechanical properties, with

positive effects. However, in literature, several researches reveal the impossibility of extrapolating the Hall-Petch relationship for grain sizes smaller than 1 μm [3] - [4]. There is an ambiguity in the trend line of the plot as the grain size is around a nanometric scale: while some results predict a plateau, others show an unexpected decrease [5]. The slope of the Hall-Petch line, which influences the relationship between the grain size and the mechanical characteristics, is different varying the metal structure. *K* value of hcp metals is higher than that of bcc, while the *K* value of bcc is higher than that of fcc. The smallest *K* value for fcc metals is related to weakly locked dislocations and a multiplicity of slip systems, and a small grain size dependence of the flow stress, the largest *K* value for hcp metals is linked to the limited slip systems, and relatively large *K* value for bcc metals is related to the strong locking. This means that with the same decrease in the size of the crystalline grain, there will not be the same variation in terms of mechanical characteristics for materials belonging to different families. The following paragraphs describe the fundamental characteristics to perform an SPD process and the main differences between SPD and conventional metal-forming processes.

2.1.1 Basic principles of SPD Methods

Generally, a Severe Plastic Deformation process, hereafter an SPD process, is defined [6] as a metal forming process that may be used to impose very high strains on materials leading to exceptional grain refinement, obtaining higher mechanical characteristics. Although there is a complex and very high stress-strain state, the dimensions of the component do not vary much, channelling all the energy of the process into the decrease of the grain size. It is possible to explain an SPD process with simplicity by analogy with a hammer that impacts a window glass: the glass can be associated with the material microstructure while the window frame is the hydrostatic pressure generated during the SPD process. The hammer that impacts the glass represents the strain imposed by the tools, which, like the hammer that destroys glass, reduces the grain size, refining the microstructure.

To perform an SPD process, special tools are used, preventing the free flow of the material. Soft materials are easily processed but hard to deform materials put some challenge to die design because the mechanics of this method has revealed that contact stresses in the die are of paramount importance [7]. In general, applying one or more SPD processes generates higher mechanical properties of the components on which they are applied, as reported by Rosochowski [8]. Among them, a greater microhardness value of the material [9] is associated with higher yield stress; however, both are characterized by a tendency to saturate with increasing applied strain [10]. Regarding other mechanical properties, the authors revealed different behaviour of ductility and toughness and magnetic properties. Weertman [11] reports an increase in yield stress, however at the expense of ductility, for samples of nanocrystalline (5 nm

grain size) and annealed coarse-grained Pd, while Valiev [12] establishes, considering copper and titanium, how, as the deformation impressed on the component increases, the ductility is not reduced, but instead increased, however reducing it compared to the as-delivered conditions.

2.1.2 Difference between SPD and conventional metal-forming processes

One of the main differences between the conventional metal forming processes and the SPD ones is the grain size: with the SPD processes, it is possible to refine the grains to sizes that cannot be attained with conventional thermomechanical treatments. The difference is about one order of magnitude: SPD processing is capable of producing grains having sizes comprised between the submicrometric and nanometric ranges, while a traditional process may refine the grains to sizes of several micrometres. Considering the shape of the grain, the microstructures obtained with conventional processes are characterized by substructures with low angle misorientation boundaries. On the other hand, the structures formed by SPD processes are ultrafine-grained or nanograined structures with predominantly HAGBs [13]. This explains the interest of large scientific and industrial sectors, which consider these materials an excellent opportunity to improve the design and performances and increase their stability during the service life. Sabirov *et al.* [14] report various industrial applications concerning aluminium, relating to the aerospace and automotive fields, underlining an increasingly marked trend towards this class of material in recent years.

For this reason, numerous processes have been developed and presented in the literature to improve the characteristics of the material by acting not with heat treatments or by various alloying but with grain refinement. Another peculiarity of the samples obtained through an SPD process is that they should be free of mechanical cracks, or damage, after plastic deformation, due to the deformation schemes that are imposed [15]. It is impossible to meet the requirements mentioned above in conventional plastic deformation methods such as drawing, rolling, torsion, or extrusion. In these manufacturing processes, the imposed plastic strain is generally less than about 2.0. This is a limit to the use as a structural part for the material: having plastic strain higher than 2.0 means that the thicknesses or diameters are very thin and unusable [16]. About the final sample, with a conventional manufacturing process, it is possible to obtain larger components, through continuous manufacture, without significant waste of material considering a hypothetical incremental process. Considering a sample obtained through an SPD process, the dimensions are smaller: after each pass, usually, part of the workpiece needs to be removed due to the presence of cracks or other defects, as reported by Faraji *et al.* [17]. The authors review different SPD methods, focusing on the sample size and the cross-sectional area, concluding that the largest sample size could be achieved from semi-continuous or continuous SPD processes, while with a discontinuous process, it is possible to obtain the smallest

samples. However, the discontinuous processes allow refining the microstructure more and homogeneously due to the higher hydrostatic pressure generated by this type of setup. A well-known way to reduce a material grain size is to apply a large deformation to activate different sliding planes, as reported by Furukawa *et al.* [18]. However, this method requires strict control of the applied stress and strain state to avoid component failure under such elevated applied strains. Several authors combined traditional extrusion or rolling processes superposed with hydrostatic pressure to prevent the growth of cracks and porosity. Faraji *et al.* [19] proposed the use of special tools to limit the material flow in these processes. Microstructural homogeneity is very difficult to obtain, and this can lead to differences in the mechanical characteristics in the final component: for this reason, it is preferred to perform several steps on the same component, varying the direction of deformation, as in the repetitive ECAP process performed by Zhilyaev *et al.* [20]. This process activates different sliding planes of the material, however reducing the size of the billet. Not being able to incorporate slightly deformed portions or defects must be removed before each deformation step to not damage the dies.

2.2 SPD process for bulk products

Two of the most used methods developed using bulk samples are proposed below, in particular the ECAP and the HPT processes, referring to the researchers who have carried out the most important studies on their applications.

2.2.1 Equal Channel Angular Pressing (ECAP)

Fig. 2.1 shows the schematic representation of the ECAP process, in which a pure shear deformation is imposed on the material without any change in the cross-sectional dimensions of the workpiece. This process was proposed [21] and developed [22] by Segal and allows to produce submicron-grained structures in various materials. The piece is extruded around a corner, which can have different angles between 80 and 130 degrees, depending on the different sliding systems to be activated.

According to the rotation angle and direction between the next passes, it is possible to obtain four different process routes:

- A: the sample is not rotated;
- B_A: the sample is rotated by 90° clockwise and counter-clockwise around its longitudinal axis alternatively;
- B_C: the sample is rotated by 90° clockwise around its longitudinal axis;
- C: the sample is rotated by 180° around its longitudinal axis.

Among the first attempts in this field are those of Azushima *et al.* [23] and Valiev *et al.* [24], which developed an innovative lateral extrusion process by using customized

dies. However, this solution is limited to the production of small dimensions bulk components, as reported by Azushima *et al.* [16], due to the high forming forces required. Furthermore, as the process is cyclically repeated to increase the amount of applied deformation, the initial and final portions of the component must be cut, reducing cycle after cycle the component volume and increasing the cost/weight ratio of the process [25].

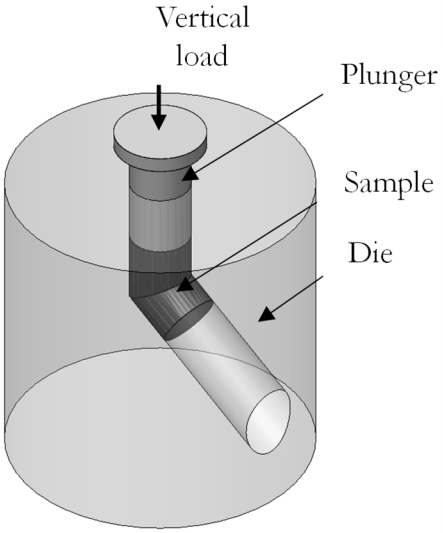

Fig. 2.1 *- Schematic representation of the ECAP process.*

2.2.2 High Pressure Torsion (HPT)

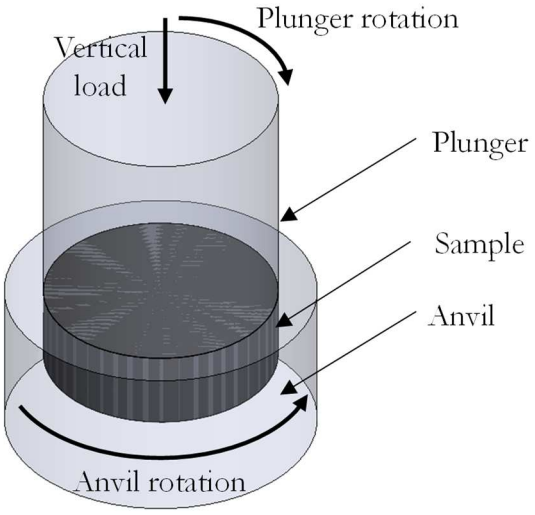

Fig. 2.2 *- Schematic representation of the HPT process.*

Although Bridgman [26] investigated in 1935 the effect of the hydrostatic pressure combined with shearing stresses, not paying attention to the microstructure change

taking place during the material deformation, only within the last 30 years several authors like Valiev [27], Xu *et al.* [28] and Zhao *et al.* [29] carried out experiments to enhance the materials mechanical properties using this process. The high pressure torsion process is schematically reported in Fig. 2.2: the sample is subjected to a high compressive load generated by the action of a plunger against an anvil. The rotation of the anvil causes frictional forces that deform the disk by torsional straining, creating a shear deformation that occurs under high hydrostatic pressure. This technique has several advantages. It allows a continuous variation of strain without losing part of the material; on the other hand, the applied strain is radius-dependant, creating inhomogeneity in the mechanical properties, as reported by Kapoor *et al.* [30].

2.3 SPD process for sheet products

In the field of sheet metal components, Tsuji *et al.* [31] varied the applied deformation impressed by the rolling process, changing the rollers distances or the lubrication conditions. Although several changes of the original process make it possible to obtain a considerable deformation [32], the appearance of defects on the rolled product is very frequent, making these processes of poor industrial applicability [25]. Below are the details of two processes developed from the sheet rolling and pressing, the Equal Channel Angular Rolling (ECAR) and the Constrained Groove Pressing (CGP).

2.3.1 Equal Channel Angular Rolling (ECAR)

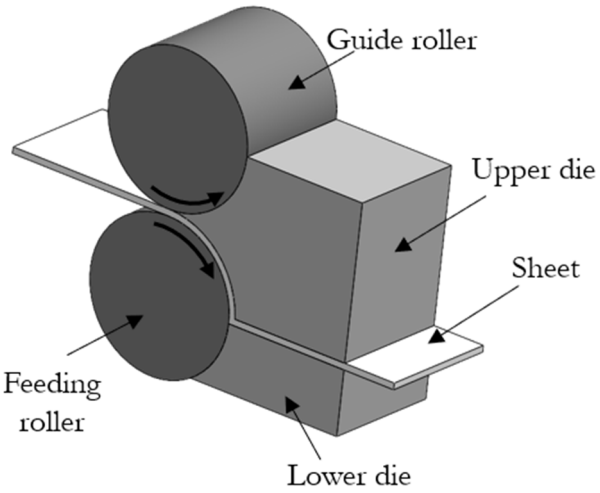

Fig. 2.3 *- Schematic representation of the ECAR process.*

The schematic representation of the ECAR process is reported in Fig. 2.3: it consists of two dies at the outlet, called upper and lower, and two rollers, called guide and feeding. The initial and final thicknesses are the same, while after the rollers, there

is a decrease in the sheet thickness in the deformation zone.

This process is the counterpart of the ECAP process for bulk samples, reported in Section 2.2.1, being a process that maintains the cross-section of the sample, activating, through the use of shear stresses, different slip systems. Due to the continuous nature of this manufacturing process, larger samples can be obtained, however, with the limitation of surface defects that could be generated by the friction of the sheet with the rollers and the dies. Analysing the mechanical characteristics of the final component, Azimi *et al.* [33] found that microhardness values at the surfaces were higher compared to the middle of thickness due to the higher strain hardening effect between the sheet and dies, which causes a non-uniform deformation [34].

2.3.2 Constrained Groove Pressing (CGP)

The Constrained Groove Pressing technique was developed by Shin *et al.* [35] for the fabrication of plate-shaped ultrafine-grained metallic materials. Fig. 2.4 represents part of the CGP process: in fact, the material is subjected to a repetitive shear deformation condition, alternating the action of corrugating and straightening the sheet using different dies. Using the groove dies, part of the sheet remains undeformed, while the inclined region of the sample is deformed by pure shear stress. After the flattening operation is carried out using flat dies, the sheet is shifted or rotated to perform the grooving operation in other sheet parts. Alternating these operations, it is possible to refine the grain structure to a sub-micrometric level and, at times, even to a nanometric level, as reported by Gupta *et al.* [36].

Though CGP is an efficient technique, it has some limitations. The sheet metals can be subjected to only a few passes because the sharp profile of the dies causes after a certain number of passes microcracks on the surface of the specimen. These surface defects lead to the decrease of the material's mechanical properties. In addition, Kumar *et al.* [37] reported that the lower grain refinement rates that are observed for the CGP technique when compared to other SPD techniques could be attributed to the non-existence of multiple shear stress planes during the deformation.

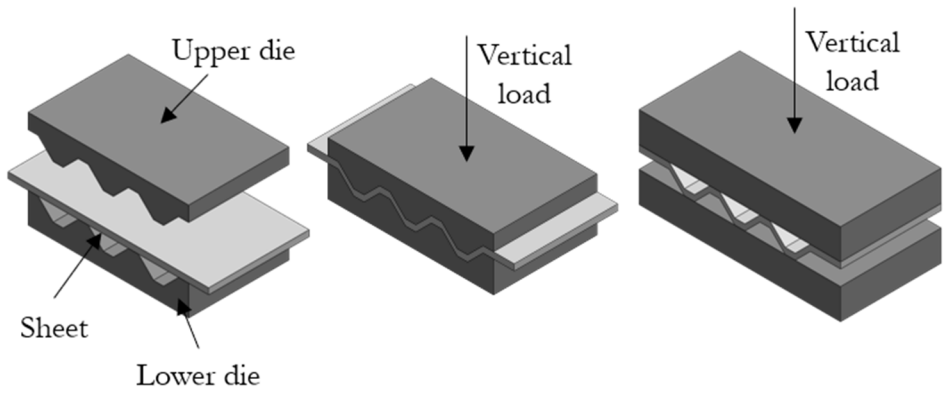

Fig. 2.4 *- Schematic representation of the CGP process.*

2.4 SPD process for tubular samples

The applications presented in the literature are not only limited to bulk and flat sheet components but also consider hollow section profiles. Several authors carried out attempts using process setups similar to those previously applied to produce bulk samples starting from traditional processes like extrusion [38] and compression [39], as reported by Faraji *et al.* [40]. However, as underlined by Baghenpour *et al.* [41], the great gap between the state of the art of these processes and a possible industrial use does not allow using these technologies to manufacture long or large diameter ultrafine-grained tubes in large quantities, thus requiring innovative methods. Below are the details of two of the most studied and interesting processes at the application level, Tubular Channel Angular Pressing (TCAP) and Spin Extrusion (SE).

2.4.1 Tubular Channel Angular Pressing (TCAP)

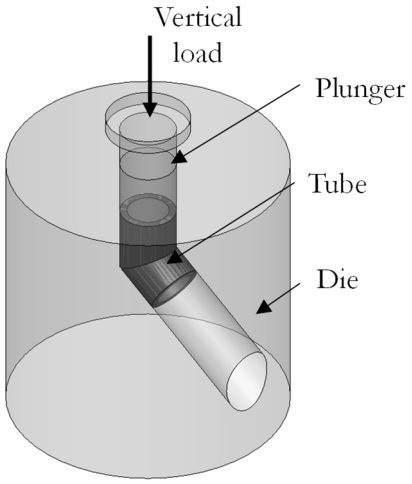

Fig. 2.5 *- Schematic representation of the TCAP process.*

Nagasekhar *et al.* [42] firstly applied the ECAP process to obtain tubes from powder, observing an interesting shear-sliding phenomenon that accompanied the powder compaction and the particle refinement. Starting from this observation, Faraji developed and patented an innovative solution [43], proposing a new process to obtain a grain refinement in tubular components, taking a cue from the ECAP process performed on bulk components. In this method, schematically represented in Fig. 2.5, the tube is pressed into the channel using a punch from the top of the die, using a flexible mandrel placed inside it to avoid its buckling or sand, rubber, and grease to prevent the tube from crushing, as reported by Djavanroodi *et al.* [44]. The extrusion channel can be lateral with different extrusion angles, as used by Jafarlou *et al.* [45] or by Djavanroodi *et al.* [46], or it can be straight with a variation in the section of the channel, as reported by Faraji *et al.* [47].

Although several authors observe that this process is effective in improving the

mechanical properties of the material, as reported by Ebrahimi *et al.* [48], using AA6083 tubes, Srivastava *et al.* [49], using Mg-3Al-1Zn, and Zhang *et al.* [50], using 316L austenitic stainless steel tubes, the greatest limitation is linked to the appearance of defects such as cracks or the sticking of the tube on the die, which makes the design difficult and the process expensive. Furthermore, as for the ECAP process for bulk components, also in this case, the number of cycles that can be performed is limited: after each cycle, the initial and final portion of the tube must be removed, considerably reducing the size of the final component.

2.4.2 Spin Extrusion (SE)

The Spin Extrusion, represented in Fig. 2.6, is an incremental rotational forming process under compressive conditions developed at the Fraunhofer University by Neugebauer *et al.* [51]. The hollow shape is formed by the pressure generated by rollers and a mandrel moving in the axial direction. The mandrel and the massive bar rotate at the same angular velocity to achieve adequate tribological conditions and generate profiled internal shapes, as Neugebauer *et al.* [52] reported. The deformation is realized in increments, locally and temporally limited, which reduces the forming forces and the required drive powers. As reported by Winter *et al.* [53] and Neugebauer *et al.* [54], after the Spin Extrusion process, considerable variations in terms of mechanical properties and grain sizes can be observed in the shaft's cross-section, with a gradient in the grain size from the inner to the outer surface. In particular [54], analysing the microstructure along the shaft radius, it is possible to observe a fine-grain in the inner side, a coarse grain in the central region, and a fine-grain and homogeneous structure in the outer portion, while in [53] the grain size varies from 1-5 μm in the surface regions to about 100-300 μm in the central regions. The biggest and most evident disadvantage of this process is the waste of material in transforming a massive component into a hollow element, reducing the economic efficiency of the process.

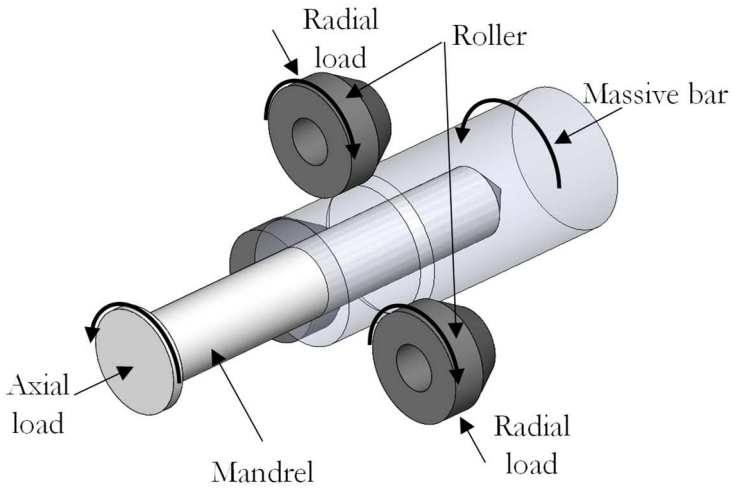

***Fig. 2.6** - Schematic representation of the SE process.*

2.5 General limitations of tube manufacturing methods

Although in the last decades' several researches concerning the production of ultrafine grain tubes have been carried out, it should be emphasized that the industrial applicability is still limited, mainly due to the size of the component that can be produced, as reported by Azushima *et al.* [16]. The methods described above and many others in the literature are generally successful in small-lengths laboratory samples. As for the bulk components, the most important limitation concerns both the component and the dies: increasing the length of the tube increases the possibility of instability and subsequent binding, with the risk of breaking the components of the dies. In addition to this phenomenon, many other tube manufacturing limitations can be found in the literature, some of which are summarized here:

- The difficulties associated with the production of large-scale industrial UFG and nanostructured tubes [55];
- Machining errors in dies manufacturing, excessive friction between the tube and dies, and structural inhomogeneity of materials could lead to the initiation and the propagation of cracks, with the eventual failure of the workpiece, with consequently not uniform mechanical properties [45];
- Very low surface quality like wavy or roughened [17], [56];
- High loads required to carry out the process, limiting the deformation-per-pass and the workpiece size [57], [58];
- Complicated and expensive equipment, with a difficult extraction of the workpiece from the dies [59]; [60];
- Time-consuming processes [61].

2.6 Effective parameters for the success of SPD Methods

Grain and sub-grain structures produced by SPD processes result from the dynamical evolution of ensembles of dislocations, sub boundaries, and the high angle boundaries, mostly frozen at the moment deformation is stopped [62]. As mentioned in Section 2.1, there is an important advantage in refining the material microstructure, according to the Hall-Petch relationship. It is important to note that the testing material influences the equilibrium grain size, defined as the smallest size of grain achievable for a particular metal or alloy after processing by a particular SPD method and process parameters. This minimum value is influenced by several parameters that can be grouped into three categories:

- SPD setup parameters: hydrostatic pressure, applied strain;
- SPD process parameters: process temperature, strain rate;
- Material parameters: composition, stacking fault energy, texture.

The influence of the setup and process parameters is described in Section 2.6.1, while the influence of the material parameters is reported in Section 2.6.2.

2.6.1 Process and setup parameters

The hydrostatic stress and the shear strain values play the main role in producing high-strength, ductile ultrafine-grained metals. Having a compressive hydrostatic pressure, it is possible to avoid crack formation and propagation [63], augmenting the workability of metals and the possibility of reaching higher equivalent plastic strain values [64]. Accordingly to Renk *et al.* [65], the heavy plastic strain of coarse-grained results in the formation of dislocation cells, which are transformed into an ultrafine-grained structure. This grain refinement saturates when the strains reach a value between 10 and 30; thus, a dynamic equilibrium occurs between deformation-induced defects (vacancies, dislocations, and boundaries) and recovery mechanisms. Pippan *et al.* [66] instead establish a limit with a deformation between 5 and 50, underlining a different behaviour regarding pure or alloyed materials, as shown in Fig. 2.7.

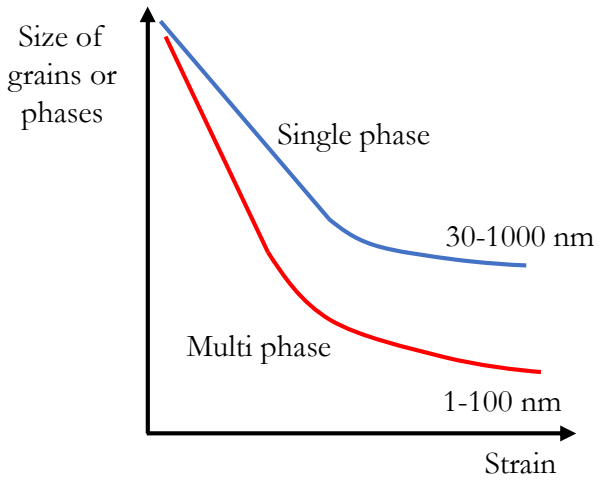

***Fig. 2.7** - Schematic sketch of the structural refinement in single- and multi-phase materials [66].*

The strain rate is another factor that affects the microstructure obtained through an SPD process. Figueiredo *et al.* [67] established that an enhanced strain rate sensitivity is advantageous for materials processed by Severe Plastic Deformation, however decreasing the material workability. The process temperature is another key factor in grain refinement during an SPD process. Increasing this parameter increases the minimum saturated grain size [68] due to the intensification of recovery processes in the grain boundaries [69]. Some researchers demonstrated that the optimum microstructure is obtained when the lowest temperature is possible [70]. However, a low temperature is a limitation for the component size due to the high load needed to perform the process. Summarizing the various process parameters described above, it is possible to obtain Fig. 2.8: the slope of the various trend lines indicates the different

role of influencing factors in the outcome of an SPD process. However, the material parameters (alloying elements, SFE) also influence the minimum grain size, and a detailed discussion is reported in Section 2.6.2.

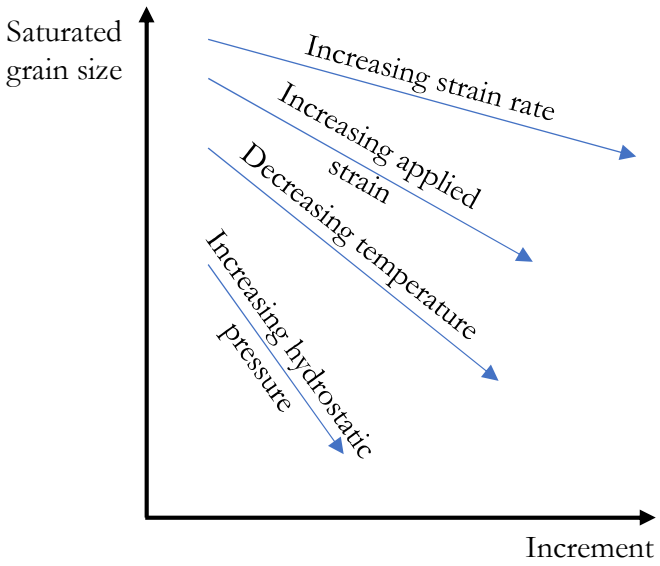

Fig. 2.8 *- Schematic representation of the influence of the process parameters on the minimum saturated grain size in SPD processing.*

2.6.2 Material parameters

The dependence of the minimum saturated grain size on stacking fault energy (SFE) is one of the most debated topics. While some authors have developed models that relate the minimum saturated grain size to SFE, other authors argue for total non-correlation. Decreasing the SFE makes it possible to decrease the minimum value of the crystalline grain, as Mohamed [71] reported. Eq. 2 represents a relationship developed by Zhu *et al.* [72], which allows to calculate the minimum value d_{min} of the crystalline grain as a function of the stacking fault energy (SFE) γ, the lattice parameter a, the Poisson's ratio ν, and the shear modulus G.

$$\frac{d_{min}}{\ln\left(\frac{\sqrt{2}d_{min}}{a}\right)} = \frac{9.69-\nu}{253.66(1-\nu)}\frac{Ga^2}{\gamma} \qquad \textit{Eq. 2}$$

On the other hand, Renk *et al.* [65] and Bruder *et al.* [73] argue that no correlation exists between saturation grain size and SFE. The stacking fault energy of materials can be modified by changing the composition of the materials. This leads to the difficulty of differentiation of the contribution of SFE and alloy elements to SPD-induced structural evolution and the mechanical properties of UFG materials, as reported by Cao *et al.* [74] and An *et al.* [75]. However, in a single alloy system, reduction

of SFE seems to be more effective to refine coarse grains to nanograins than alloying [76]. Some researchers carried out several experiments to investigate if it is possible to attain much smaller grain sizes by alloying, as reported by Iwahashi *et al.* [77]. The authors increasing the percentage of Mg in an Al-alloy showed that the equilibrium grain size is reduced increasing the Mg. The effects of Mg additions are attributed to the reduction in dislocation mobility and the consequent lower recovery rates in the solid solution alloys. Roven *et al.* [78] demonstrated a positive influence of the alloying element on the mechanical behaviour obtained through an SPD process, with higher yield stress values.

The crystallographic texture of a material, also known as preferred orientation, is defined as a microstructural property that describes the orientation of a certain proportion of grains in the material than the neighbouring grains. The post-processed deformation texture can affect many aspects of material behaviour, such as formability, grain refinement, work hardening, plastic anisotropy, and fracture, as reported by Beyerlein *et al.* [79]. These researchers analysed the texture evolution in the ECAP process, considering multiple factors like the applied strain path, die geometry, processing conditions, initial texture, material plastic behaviour, concluding that an SPD process due to the amount of strain, the deformation path, the strain rate, the hydrostatic pressure, the lubrication condition, and the temperature, influence the final texture which in turn depends on the initial texture. Small differences in pre-processing that change the initial texture and microstructure can produce large differences in the final texture under the same deformation process. Tavakkoli *et al.* [80], in the parallel tubular channel angular pressing studies, observed that the mechanical anisotropy and different mechanical properties along the axial and peripheral directions could be related to a crystallographic texture that is changed during the processing. In contrast, Yapici *et al.* [81] observed that texture evolution during straining contributes significantly to the tension-compression asymmetry.

The mechanism for establishing the steady-state condition in SPD processing is not clear, and researchers suggested different reasons to explain this phenomenon. Eckert *et al.* [82], in their preliminary studies regarding the ultimate grain sizes achievable by mechanical friction, suggested a general relation between the plastic deformation and the recovery behaviour. This theory was also followed by Pippan *et al.* [66], which established that in the saturation regime, the generation of defects, i.e., the generation of dislocations, vacancies, and new boundaries, has to be in equilibrium with the annihilation of these defects. However, other researchers suggested twinning [83] - [84], grain boundary migration [85], or dynamic recrystallization [86] - [87] as important processes influencing the steady-state. Higuera *et al.* [88] reported that most metallic materials undergoing the SPD process display a steady grain size, in such a way that no matter to introduce extra strain, as the grain size remains constant, even though more strain is added.

A very high density of grain boundaries is present within a UFG material,

influencing the mechanical properties and allowing to development of a new type of engineering design, based precisely on the exploitation of the grain boundary orientation, as reported by Valiev *et al.* [89]. For this purpose, for example, Liu *et al.* [90] developed a finite element computational model of UFG or NG titanium, based on a unit cell model and the dislocation density to evaluate the mechanical behaviour of the material, considering the grain orientation and their deviation from the undeformed condition in the case of SPD process applications. Depending on the typology of the SPD process, different types of grain boundaries are formed, and they can be classified as low-angle or high-angle, which amount and balance characterize the mechanical properties [91]. Low-angle grain boundaries (LAGBs) have fewer than 15 degrees of misorientation, while higher misorientation characterized the high-angle grain boundaries (HAGBs).

2.7 Tube flowforming

To overcome the problem related to the size of the component, having at the same time a refined microstructure, it is possible to use the flowforming process [92], deriving it from tube spinning, exploiting an incremental approach, as reported Wong *et al.* [93]. Tube flowforming is well-known in the industry for producing axisymmetric net-shaped parts, thanks to the simultaneous action of three rollers that reduce the thickness of a tubular billet by combining radial and axial movements of the tools while maintaining the internal wall of the piece unaltered [94].

Regarding the microstructural observations of the components after the flowforming operations, most of the authors' contributions were focused on the link between the wall thickness reduction with the microstructure and mechanical properties evolution, as reported by Wang *et al.* [95] and Molladavoudi *et al.* [96]. The thickness reduction greatly affects the grain size, in particular, the grain refinement level and its orientation, as reported by Zhang *et al.* [97] studying the hot flowforming behaviour of AZ31B alloy tubes, and the grain morphology, as reported by Wang *et al.* [95] studying the microstructure evolution of the Ti-6Al-2Zr-1Mo-1V alloy during the multi-pass flowforming process. The thickness reduction meanwhile increases the effective plastic strain, thus generating higher microhardness values. Therefore, multi-pass flowforming is often applied to increase the wall thickness reduction. However, the grain shape is often uneven in the radial direction due to the deformation mechanism since the plastic strain is thickness-related during the flowforming process. Focusing on the power spinning method, Xiao *et al.* [98] observed a gradual decrease in the equivalent plastic strain from the outer surface to the inner surface with consequent inhomogeneous grain size, with finer grains than those inside layers. Accordingly to the Hall-Petch relationship, the grain texture [99] and its smaller size cause higher mechanical properties.

However, few studies have paid attention to the grain refinement mechanism of

flowformed components, especially for the aluminium alloy formed at room temperature. In the few literature, the contributions of Mohebbi *et al.* [100] and Zhan *et al.* [101] establish that ultrafine grains originated from the sub-grain misorientation that occurred after the accumulative spin-bonding process and that deformation bands caused by the refined microstructure during shear spinning aluminium alloy, demonstrating the feasibility of using this process to increase the mechanical properties of the component. As reported by Ghiotti *et al.* [102], analysing the conical shapes flowforming, the stress and strain that the material undergoes is a function of the position of the rollers with respect to it. Under the rollers, a high compressive hydrostatic pressure is formed, while when the rollers move, the hydrostatic pressure reaches a negative value due to the decrease of radial compression and the increase of axial tensile load. The following paragraphs describe the fundamental characteristics of the tube flowforming process and the main advantages and disadvantages of using this process as an SPD technique.

2.7.1 Process details

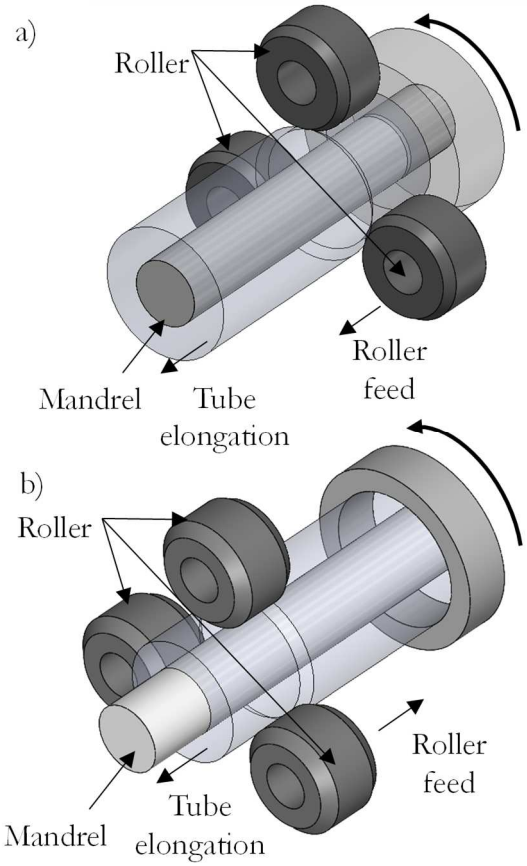

Fig. 2.9 *- Schematic representation of a) the forward and b) the backward tube flowforming.*

The schematic representation of the flowforming process is reported in Fig. 2.9, distinguishing two versions: a) the forward and b) the backward. Most modern

machines employ a three-roller configuration, spaced circumferentially at 120 degrees to achieve a better balance of loads for flowformed components. At the same time, the equipment was designed to allow both the radial and axial offsetting of the rollers. By varying the radial position, it was possible to set the reduction per pass, while the variation of the axial position was used to control surface defects [103] that may appear on the outer surface of the tube and that depends on the imposed reduction per pass. Considering the forward flowforming, represented in Fig. 2.9a, the direction of the material flow is the same as the roller's displacement, with the part that has not been worked which is driven ahead of the rollers. The tube is held between the mandrel and the tailstock, which requires a base or a flange to clamp against the part. In the backward flowforming configuration, represented in Fig. 2.9b, which is suitable to materials with limited ductility, the pressure generated by the rollers pushes the material against the mandrel, and the material flow is opposite to the rollers feed. Due to the deformation mechanism, the material under the rollers is deformed in a compressive stress state, which contributes to increasing the formability with the refinement of the grains, as reported by Xu *et al.* [104].

The main advantage in the forward flowforming as compared to the backward configuration is that it overcomes the problem of distortion at the free end and loss of straightness, as reported by Sivanandini *et al.* [105]. On the other hand, the preform is simpler for the backward configuration and does not require an internal flange for clamping. Xu *et al.* [104] analysed the deformation mechanism and concluded that there is no obvious difference in stress and strain rate on the surface between forward and backward tube spinning for the same process conditions. Bhatt *et al.* [106] compared the loads during the forward and backward flowforming using FE analysis. It has been found that the axial and radial forces are higher in the forward flowforming configuration, while the circumferential load is higher in the backward configuration. Moreover, plastic strain distribution along the thickness is found higher in forward flowforming and along the length, it is found higher in backward flowforming. For these reasons, wanting to minimize the axial load necessary to perform the process, it was decided to use the backward configuration.

2.7.2 Is flowforming an SPD process?

In the literature, there are few references to the use of flowforming as an SPD process. However, comparing the characteristics of the SPD methods with those of the flowforming process, it is possible to find some elements in common and others that instead distinguish them, briefly summarized in Tab. 2.1. Among the elements that can make the flowforming process be described as an SPD technique is the refining of the grain, there are in fact similarities between the microstructural evolution of materials subjected to tube flowforming and other SPD processes. Several authors report a notable refinement of the crystalline grain, with a grain flattening deformation

along the radial direction and a grain elongation in the rolling direction, as reported by Wang *et al.* [95]. Yuebing *et al.* [107] carried out the flowforming operation using 34CrMo4, obtaining a grain refinement approximatively equal to 11 times, starting from 11.22 μm and deforming it until 1.00 μm. The grains' misorientation increases with the strain, forming HAGBs, as reported by Xia *et al.* [108] studying the microstructural evolution of the spun tubes made of ASTM 1020 steel processed stagger spinning. Considering the plastic strain, Bedeker *et al.* [109] reported large plastic strain values during the flowforming of AISI 1050 steel, developing a UFG structure. However, Xiao *et al.* [98] reported a gradient along the tube radius in the effective plastic strain values due to the process characteristics. This strain gradient influences the mechanical characteristics of the workpiece, having a different grain size and different microhardness.

Regarding the uncommon elements with SPD processes, the cross-section variation is one of the most evident. Technically, the flowforming process involves a reduction in the thickness of the tube, with consequent elongation. However, other processes catalogued as SPD also reduce cross-section, as reported by the torsion-extrusion process developed by Mizunuma [110], in which the final cross-section has a diameter of 5 mm obtained from a billet with a diameter equal to 10 mm. A unique direction of deformation is possible due to the setup configuration; however, the rotation of the tube allows to activate different sliding planes as reported by Cao *et al.* [111], which means that the unique direction of deformation is only a theoretical uncommon characteristic. Several authors [98] reported a gradient in the grain size of a flowformed tube about the anisotropy in mechanical characteristics. However, this aspect is also observed in other SPD processes, like the Spinning Extrusion [53] or the High Pressure Torsion [30]. The presence of compressive hydrostatic pressure is guaranteed below the rollers [102], still the material is free to flow due to the absence of dies or other containment elements. To this end, a setup has been developed that allows solving this problem by using a radial constraint that allows both to increase the hydrostatic pressure on the material and avoid surface defects. This setup is described in Section 5.3.

Tab. 2.1 *- Common and uncommon characteristics between flowforming and an SPD process.*

Common characteristics	Uncommon characteristics
Grain refinement	Variations of cross-section
HAGBs	Unique direction of deformation
Plastic strain	Anisotropy in mechanical characteristics
	Hydrostatic pressure

Comparing the flowforming technique with other SPD processes, several pros can be found. First of all, the size of the components could be obtained because this process allows obtaining larger UFG tubes compared with the classic SPD techniques.

An incremental process requires lower loads to deform the tube, obtaining a product with higher quality and without defects (cracks, porosities, etc.) concerning an SPD process. Considering the tube extraction from dies is simpler than an ECAP process, requiring less expensive setups and fewer dimensional and geometric tolerances. About the cons, being an incremental process, it is time-consuming, and this could be a negative aspect for an industrial application. Considering the mechanical anisotropy, a positive aspect of this cons could be presented: innovative use of the component, with tailored properties and with different characteristics, for example from the inner and the outer side would allow a different engineering design, having the possibility of having the best configuration in the desired place.

Tab. 2.2 *- Pros and cons of the tube flowforming.*

Pros	Cons
Low loads	Time-consuming
Surface quality	Anisotropy in mechanical characteristics
No material defects	
Simple extraction	
Size of components	

2.8 Conclusions

It is well known that materials characterized by a very small crystalline grain size show high mechanical characteristics. To obtain this type of microstructure from a material initially characterized by a coarse-grained microstructure, it is essential to impose high strain without significant variations in the overall dimensions of the sample to have the possibility to perform many times the refining process.

The literature review highlighted how the successful production through an SPD process is complex and with many possible criticalities; hence, it has a high added value from a technological point of view. These processes operate under a wide range of uncertainties related to the different behaviour of grain refinement. From an industrial point-of-view, among the several available technologies, the common limit regards the dimension of the workpiece: usually is produced a laboratory-scale component, with low industrial applicability. From an analysis of the costs in terms of time-consuming design and dies production, it is possible to notice how the gap between the theoretical application and the industry remains important.

One way to solve the typical limitations of SPD processes can be to use the flowforming technique. This process allows obtaining various advantages of industrial applicability, first of all, the size of the components and the possibility of varying the characteristics of the process in real-time, allowing to obtain tailored characteristics. This aspect is very important because more and more the industrial need is to reduce waste, optimizing production through a topological optimization approach. It can be

obtained through the removal of excess material or through a net-shape approach, where during the process, we try to minimize the difference between the component being machined and the final component. The flowforming process is based on the latter approach, allowing to obtain the desired component through incremental procedures, reducing waste and loads during the process. In addition, not only tubular components can be obtained. It is possible to provide a chain of processes that allows obtaining UFG sheets, with the peculiar characteristic of having a gradient of mechanical properties between the two faces is not obtainable by any of the currently available processes.

Part 3: Material and Methods

Chapter 3

Material

This Chapter reports the characterization in the as-delivered condition of AA6082-T4 (DIN 3.2315), which is the material object to investigation using the backward tube flowforming and the constrained backward tube flowforming processes. This alloy is used very often in structural profiles and offers good formability and machinability, with alloying elements that guarantee a good propensity to be deformed by SPD processes, as reported in Section 2.6.2. The tubes' nominal chemical composition is reported in Tab. 3.1. The tube has a length of 75.0±0.1 mm, an initial outer diameter of 30.0±0.05 mm, and an inner diameter of 25.0±0.1.

Tab. 3.1 *- Nominal chemical composition of AA6082-T4 tubes.*

El.	Al	Si	Mg	Mn	Fe	Cr	Zn	Ti	Cu
Wt. %	base	0.7-1.3	0.6-1.2	0.4-1.0	0.0-0.5	0.0-0.3	0.0-0.2	0.0-0.1	0.0-0.1

3.1 Tensile test

Three tensile tests were carried out at room temperature, using a strain rate equal to 1 s^{-1}, to characterize the material's mechanical properties in the as-delivered conditions. The tensile tests were carried out using an *MTS™-322* hydraulic dynamometer, with a maximum load of 50 kN and a maximum stroke of 150 mm. From three different tube, a tensile specimen was obtained by water cutting. From the tensile tests, the maximum elongation, yield stress, and ultimate tensile strength were evaluated to calibrate the material model for numerical simulations using the Hollomon equation. These data, reported in Tab. 3.2, were compared with the data obtained from the tensile tests on the flowformed material to investigate changes in the mechanical properties consequent to the processes.

In evaluating the mechanical properties, the average results of the three tests were taken into account, without reporting the variability of the results as it is not significant for the purposes of numerical simulation. The coefficients *n* and *K* minimize the error with the experimental curves through an optimization process, while the elongation, yield stress and UTS values are obtained from the experimental curves.

Tab. 3.2 *- Mechanical properties of AA6082-T4 tubes.*

E (GPa)	Y (MPa)	A (%)	UTS (MPa)	n (-)	K (MPa)
70	175	15	200	0.09	289

3.2 Microstructure analysis

In addition to the tensile tests, the tube's microstructural characteristics in the as-delivered conditions were evaluated to investigate the variation of this material parameter after the flowforming processes. All the samples were prepared for microstructural analysis using SiC papers for grinding and colloidal silica for the final polishing. The grain structure was revealed by chemical etching using the Weck's reagent, a solution of 4 g $KMnO_4$ + 1 g NaOH + 100 ml H_2O for 12 seconds, using images obtained by a Scanning Electron Microscope (SEM) FEI Quanta™ 400 SEM.

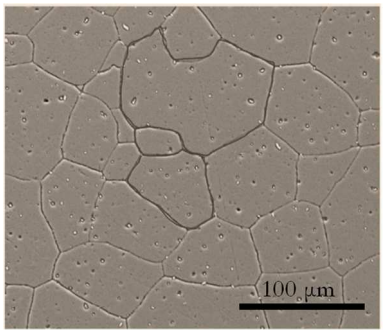

Fig. 3.1 *- Microstructure in the as-delivered condition.*

Fig. 3.1 represents an example of microstructure in the as-delivered condition, with a grain size equal to 70±17 µm, obtained analysing 10 different cross-sections along the tube, repeating the tests considering three different tube, to take into account the material variability. The grain structure is composed of equiaxed grains with no homogeneous dimensions. Due to this, the quantitative microstructural parameters were measured through the intercept lines method (Heyn method), using four directions of analysis (0 deg, ± 45 deg, 90 deg). 4 directions were chosen on which to carry out the grain size measurement. In this way, it was possible to consider the anisotropy in the shape and size of the grain, in particular after the flowforming process. For this reason, an in deep analysis regarding the grain size evaluation method was carry out and reported in Section 6.2.

3.3 Microhardness analysis

To evaluate the Vickers microhardness (HV) of the as-delivered material, a Leitz™ *Durometer* was used to carry out six indentations, repeated three times in each zone, using a 2.942 N load and 15 seconds of dwell time. The 18 indentations were performed in three different tube, to take into account the material variability. Fig. 3.2 represents the Vickers microhardness in the as-delivered condition, with an HV equal to 60.9±1.5, with the dispersion considers the minimum and the maximum value.

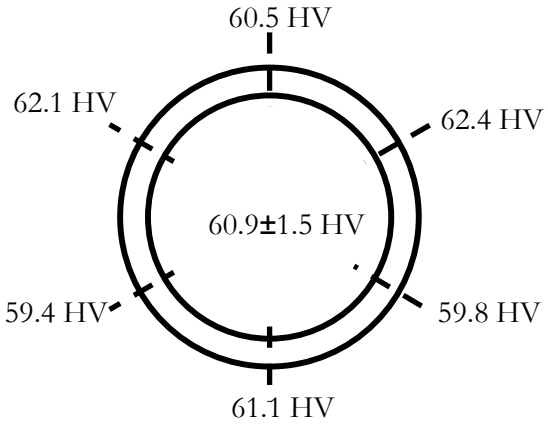

Fig. 3.2 *- Vickers microhardness in the as-delivered condition.*

Chapter 4

Numerical simulations

In this Chapter, the numerical simulations of the flowforming processes are reported, focusing on the influence of the process parameters on the strain values along the tube and the surface defects during the process. The first part reports the state of the art regarding the numerical modelling of the tube flowforming process, investigating the relationship among the process parameters and the strain distribution and the loads during the process. In addition, the state of the art relating to the prediction of surface defects resulting from the flowforming process is reported. The second and third parts refer to the numerical simulation of the backward tube flowforming process, considering the traditional setup and an innovative setup with a radial constraint. These parts focus on the relationship between geometrical and kinematics parameters and the strain along the tube, optimizing the process parameters to obtain uniform strain distributions in the axial and radial direction, minimizing surface defects, and verifying the loads acting on the rollers.

4.1 State of the art

As the flowforming is a non-linear plastic deformation manufacturing process, FE numerical simulations are required to understand the stress state and the strain distributions during the process for efficient and successful product manufacturing. In addition, the use of FE methods allows to predict the stress-strain distributions and the loads acting on the rollers during the process and to avoid surface defects. Several authors already studied how to numerical modelling the flowforming process, analysing the influence of the process parameters on the strain distribution or the process loads. Hua *et al.* [112] established, using a 3D elastic-plastic FE model for the backward tube flowforming, that the material in the contact zones is in a 3D

compressive stress state and that locally there are tensile stresses. In addition, the authors concluded that the surface cracks are caused by the circumferential and axial tensile stresses, and by minimizing these loads, it is possible to avoid the formation of this defect. Wang *et al.* [113] focused their study on the comprehension of the microstructure inhomogeneity development during the backward tube flowforming of TA15 alloys, analysing the strain distribution in the (i) axial, (ii) radial, and (iii) circumferential directions. The different amount of strain in these directions causes an elongation of the grain in the axial and circumferential directions, while the grain shape is compressed along the radial direction. In addition, it is possible to notice how increasing the forming pass can decrease the inhomogeneous microstructure characteristics. Bhatt *et al.* [106] compared two different flowforming strategies, the forward and the backward, using FE analysis. In particular, the authors investigated the differences between the forward and the backward loads during the process, considering the (i) axial, (ii) radial, and (iii) circumferential directions. It has been found that the axial and radial forces are higher in the forward flowforming configuration, while the circumferential load is higher in the backward configuration.

Several authors carried out experiments about the effect of flowforming process variables, such as the rollers feed rate and the thickness reduction, on the stress and strain distributions and rollers forces. In particular, Bhatt *et al.* [114] investigated the influence of different variables during the flowforming process of AA6063 alloy, distinguishing many factors, namely (i) operating variables (rotational and axial feed, depth of forming), (ii) material variables (microhardness, yield stress, UTS, hardening and strength coefficients), and (iii) geometrical variables (roller diameter, roller thickness, roller angles). Based on these process parameters, the authors derived that the axial and circumferential forces are affected by the roller feed in the axial direction and the friction coefficient. In addition, the friction coefficient also affects the value of the radial loads. Parsa *et al.* [115] studied the effects of attack angles of the rollers and feed rates on the flow formability, concluding that the flow formability decreases by increasing the feed rate, while the attack angle has no significant effect on the flow formability. Kim *et al.* [116] described the influence of the attack angle by the upper bound analysis, developing a model that predicts the optimal angle with the minimum axial force. In addition, the FE simulations allow predicting the tube shape, in particular the surface defects like the build-up and the springback. Cao *et al.* [111] had studied the effects of processing parameters including flowforming temperature, mandrel speed, feed rate, and thickness reduction on the microstructure and mechanical properties of AZ80 alloy tubes, showing that the variation of mandrel speed and feed rate had a slight influence on the microstructure, however influencing the elongation. In addition, increasing the thickness reduction, the grain size decreased while the material microhardness increased significantly. Razani et *al.* [117] had done an experimental study on AISI304 using the response surface methodology to develop a mathematical model to predict the optimum microhardness, having as parameters of

influence the rotational speed of the mandrel, the feed rate, and wall thickness reduction. The authors' model revealed that the microhardness increases with increasing of the mandrel speed and the depth of cut, and it decreases with a decrease of the feed rate. In addition to the relationship between the process parameters and the deformation distribution and with the acting loads, several researchers developed FE models to predict, as a function of the process parameters and the material, the formation of surface defects such as (i) build-up, (ii) bulging between the rollers, and (iii) bell-mouth, as reported in Fig. 4.1.

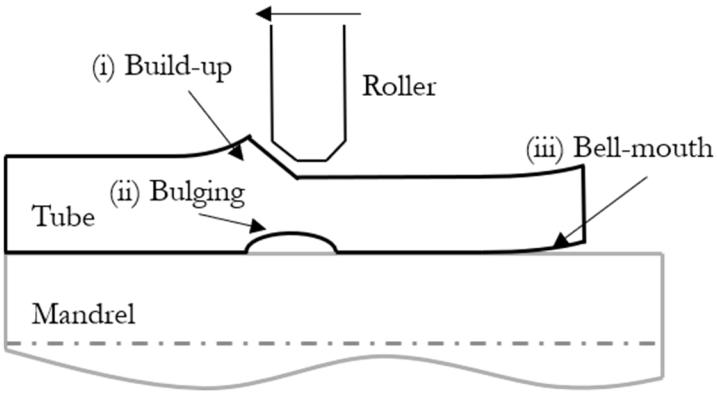

Fig. 4.1 *- Typical defects for the backward tube flowforming.*

Srinivasulu *et al.* [118] focused the research on studying the influence of various process parameters on dimensional and surface characteristics of AA6082-T4 flowformed tubes, concluding that the roller radius, the roller axial feed, the thickness reduction, the initial heat-treatment condition has a significant effect. In particular, lower feed rates improve the surface finish, increasing the ovality and the variation in the mean diameter. Shinde *et al.* [119] have conducted a study to develop a parametric model to predict the ovality, the diametral growth, roll forces, stresses, and strain as a function of process parameters during the three-roller staggered backward flowforming of MDN-250 maraging steel tube. The feed rate, the reduction ratio, and the attack angle of the roller are found to be the most significant parameters to control the circularity of the tube. Among all process variables, the feed rate and the reduction ratio are the most significant parameters for the effective plastic strain and the roller forces, following a proportional trend.

The following paragraphs describe the numerical models used in the case of backward tube flowforming and constrained backward tube flowforming.

4.2 Backward Tube Flowforming

To understand the influence that the geometric and kinematics process parameters have on the strain distribution and, consequently, on the material properties, a FE model of the traditional backward tube flowforming was developed on the Forge™

environment. In addition, the FE models allow investigating the relationship between process parameters and surface defects, like the build-up, bulging between the rollers and the bell-mouth, as reported in Fig. 4.1. Geometrical parameters and kinematics parameters were varied, analysing the strain distribution in the (i) axial, (ii) radial, and (iii) circumferential directions, according to the scheme shown in Fig. 4.2.

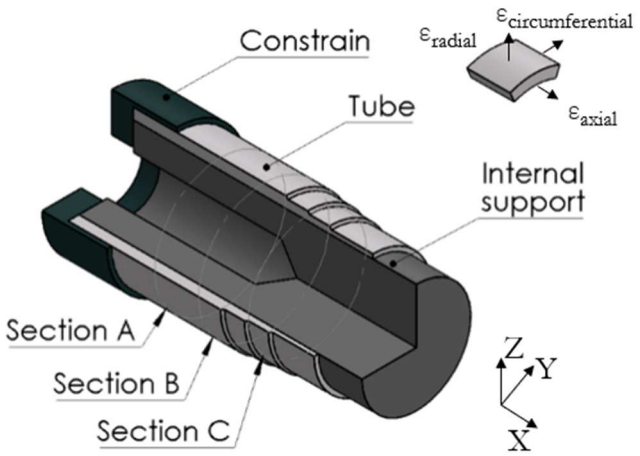

Fig. 4.2 *- Schematic representation of analyses cross-sections.*

In particular different tube cross-sections at three distances from the constraint, namely Section *A*, placed at a distance equal to 10 mm, Section *B*, placed at a distance equal to 20 mm, and Section *C*, placed at a distance equal to 30 mm, were considered. Three different tube portions were considered for each cross-section, subdividing the thickness into three parts and using a strain-sensor placed in the centre of each part. To reduce the number of simulations necessary to have a good knowledge of the process, average values of some parameters were chosen, analysing the influence of parameters kept free. Having optimized the latter, it proceeded by varying those that had previously been kept fixed.

4.2.1 FE Model

Fig. 4.3 shows the numerical model setup, in which the three rollers and mandrel were modelled as rigid bodies while the workpiece was meshed as a deformable body by using elements with different mesh sizes. In particular, for the workpiece, as reported in Fig. 4.4, under the rollers, the elements were sliced by a 3 deg angle, while in the rest of the workpiece, 10 deg angle elements were adopted.

A tube length of 70 mm was used to ensure process stability and investigate differences along the axial direction, while the total stroke of the rollers was fixed at a value equal to 35 mm. The inner and outer diameters were respectively equal to 25 mm and 30 mm. A unique flowforming pass was numerically simulated to investigate the influence of geometrical and kinematics parameters. At the same time, for the strain

analysis as a function of the thickness reduction, an incremental numerical simulation was developed, considering the cumulative deformations and stresses in each pass. To simulate the effect of the tailstock and the tube rotation, the nodes at one end of the workpiece were constrained in the axial and angular directions. The axial constraint, obtained by the plate manipulator function, aims at reproducing the mandrel that keeps the tube fixed. In contrast, the angular constraint, obtained by the rotating manipulator function, was used to simplify the contact condition between the mandrel and the tube by imposing the spindle speed directly on the workpiece nodes.

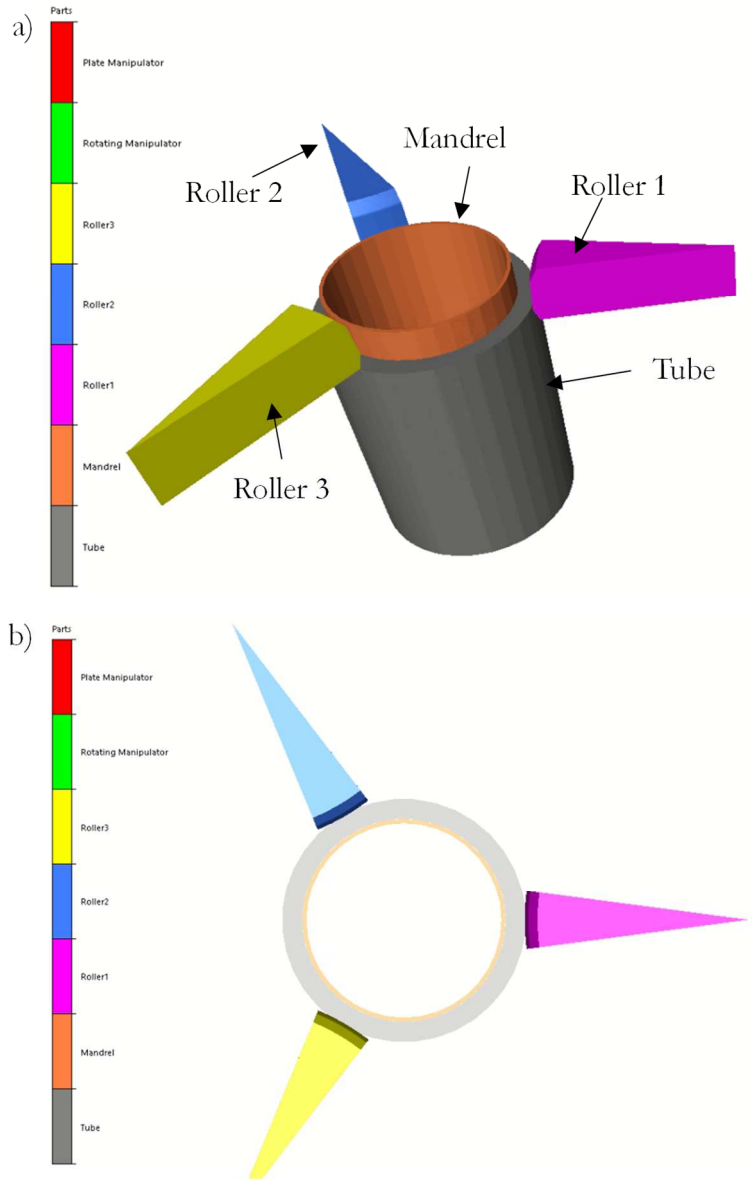

Fig. 4.3 *- Numerical FE model of backward flowforming: (a) perspective view; (b) frontal view.*

The workpiece is considered elastic-plastic, and it was modelled through the Hooke equation for stress lower than σ_Y and with the Hollomon equation for stress

larger than σ_Y, as reported in the following equation:

$$\sigma = \begin{cases} E\varepsilon \text{ for } \sigma < \sigma_Y \\ K\varepsilon^n \text{ for } \sigma \geq \sigma_Y \end{cases} \qquad \textit{Eq. 3}$$

where the values of the coefficient K and n of the AA6082-T4 alloy are reported in Chapter 3. Since the process is carried out at room temperature, the temperature and strain rate effects were assumed negligible.

A surface-to-surface contact was set between the mandrel and the inner tube surface and between the rollers and tube outer surface. The former was modelled according to the Coulomb equation, assuming a friction coefficient μ=0.1; for the latter, a sliding condition without friction was assumed based on the fact that the contribution of the rolling friction was considered negligible in the experiments, as proved by the absence of material flow in the circumferential direction. The three-roller configuration, spaced circumferentially at 120 deg, allowed a better balance of loads. By varying the radial position, it was possible to set the thickness reduction per pass, while the variation of the axial position was used to control the surface defects that may appear on the outer surface of the tube and depend on the imposed reduction per pass. The influences of axial and radial rollers positions and the shape of the rollers on the strain distribution were evaluated. A variable rotational speed and rollers feed rate were selected to investigate the influence of different kinematics parameters.

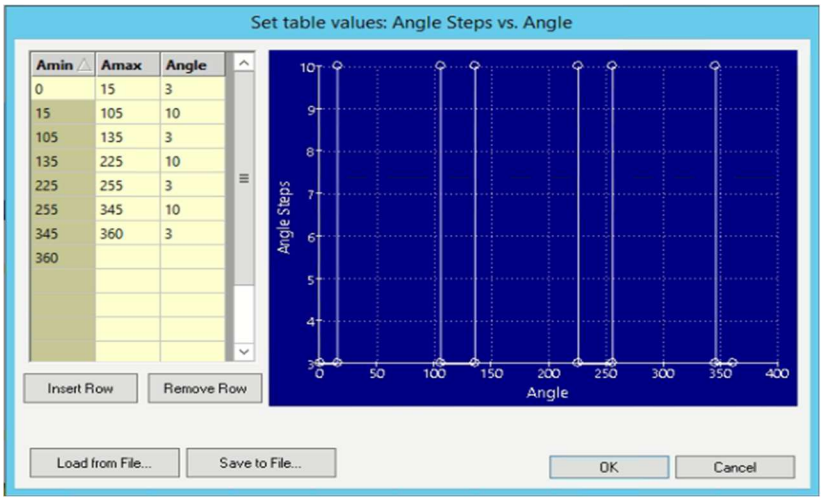

Fig. 4.4 *- Mesh dimension for the workpiece.*

4.2.2 Geometrical parameters

Tab. 4.1 *- Roller geometrical parameters.*

α (deg)	β (deg)	γ (deg)	l (mm)	r (mm)
20	20	3	3	1
25	30	5	5	5
30				

Double-tapered rollers (see Fig. 4.5) were designed to improve the surface smoothness of the flowformed tube. For thin-walled soft materials, such as aluminium alloys, the following values are suggested: (i) the forming angle a in the range 15-30 deg, (ii) the sleeking angle γ is usually 3-5 deg, (iii) the receding angle β is 20-30 deg, (iv) the fillet radius r is 1-10 mm, and (v) the polishing belt length l is 3-6 mm [108]. To reduce the number of simulations necessary to analyse all the possible combinations, the values reported in Tab. 4.1 were chosen, with constant kinematic values equal to 2 mm/s for the roller feed rate f and 420 rpm for the rotation speed of the tube ω. The total simulations are 48 fixing the other geometric variables, as the roller radius R, equal to 27.5 mm, the axial roller offset a, equal to 1.5 mm, and the thickness reduction Δt_i, equal to 0.10 mm for each roller.

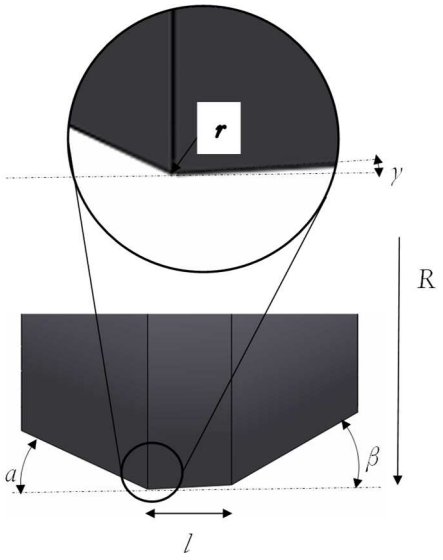

Fig. 4.5 *- Key dimensions of roller.*

Once the geometric parameters of the rollers have been chosen, their axial distance is subject to optimization to avoid surface defects such as build-up or axial force values that are not compatible with the equipment used. The values of axial offset a are reported in Tab. 4.2, also considering in these cases constant kinematic values equal to 2 mm/s for the roller feed rate f and 420 rpm for the rotation speed of the tube ω. For the investigation of the roller axial distance influence, the total amount of simulations needed is 5.

Tab. 4.2 *- Axial offset optimization for the rollers.*

#	a (mm)
1	0.5
2	1
3	1.5
4	2
5	2.5

4.2.3 *Kinematics parameters*

The values of the process parameters being analysed are the roller feed *f* of the rollers and the rotational speed of the tube *ω*, as reported in Fig. 4.6. The rotational speeds have been chosen in such a way as to consider the minimum value of 240 rpm for and a maximum value of 600 rpm, which has been seen, through feasibility experimental tests, to be the limit values for avoiding vibrations (for values higher than 600 rpm) and process time (for values below 240 rpm). On the other hand, the feed rates must consider the process time (values below 0.5 mm/s) or the risk of heating the material (values above 2 mm/s).

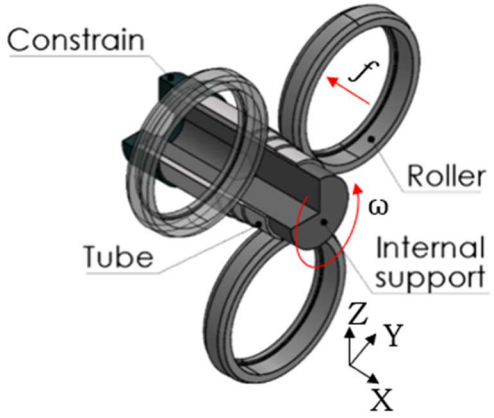

Fig. 4.6 *- Kinematics parameters.*

The optimal geometrical parameters were adopted to reduce the number of simulations, while the kinematics values are the combination of the values reported in Tab. 4.3, needing 12 simulations for the kinematics parameters investigation.

Tab. 4.3 *- Kinematics parameters optimization.*

f (mm/s)	ω (rpm)
0.5	240
1	420
1.5	600
2	

4.2.4 *Thickness reduction*

Tab. 4.4 *- Thickness reduction optimization for each roller.*

Δt_1 (mm)	Δt_2 (mm)	Δt_3 (mm)
0.05	0.05	0.05
0.15	0.15	0.15
0.30	0.30	0.30

Fixed the geometrical rollers parameters and the axial offset among them, and

calculated the optimal kinematics parameters, the thickness reductions for each roller Δt_i are optimized to avoid also in this case surface defects or higher axial loads. The Δt_i values, reported in Tab. 4.4, take into account the position of each roller. In particular, the relative interpenetrations for each roller are reported, which combined give a total simulations number equal to 27.

4.2.5 Incremental process

Once the radial position of the rollers has been chosen to reduce surface defects and minimize the axial force required to complete the process, several passes on the same tube can be performed. The incremental action of the process guarantees two objectives, low forces and high deformations. By doing this, it is possible to reach the same deformation state that would have been obtained with a much greater interpenetration but with considerably fewer necessary forces. In addition, it is possible to minimize the possibility of the appearance of surface defects. The initial and final thicknesses of the tube after each pass of the incremental process and the percentage reduction in thickness for each roller are shown in Tab. 4.5. Following what is described in Section 4.4.1.4 regarding the interpenetration of the rollers, a solution was chosen which guaranteed the absence of surface defects, moderate axial loads, and balanced deformation on each roll. The results of these simulations are reported in Chapter 7, comparing these with the experimental results in terms of microhardness, microstructure, mechanical properties, and tube elongation.

Tab. 4.5 *- Incremental process simulation details.*

#	$t_{initial}$ (mm)	t_{final} (mm)	Δt_1 (mm)	Δt_2 (mm)	Δt_3 (mm)
1	2.50	2.35	-2%	-2%	-2%
2	2.35	2.20	-2%	-2%	-2%
3	2.20	2.05	-2%	-2%	-2%
4	2.05	1.90	-2%	-2%	-2%
5	1.90	1.75	-2%	-2%	-2%
6	1.75	1.60	-2%	-2%	-2%
7	1.60	1.45	-2%	-2%	-2%

4.3 Constrained Backward Tube Flowforming

As for the traditional backward tube flowforming, a FE model of the constrained backward tube flowforming was developed on the Forge™ environment. In this case, in addition to the aim of investigating the relationship between process parameters and surface defects, the role of the radial constraint, reported in Fig. 4.7, was investigated, firstly to understand if it influences the distribution of the strain along the workpiece and secondly if its length influences the deformation of the workpiece. As in this model were considered different tube cross-sections at three distances from the constraint,

namely Section *A*, placed at a distance equal to 10 mm, Section *B*, placed at a distance equal to 20 mm, and Section *C*, placed at a distance equal to 30 mm. Three different tube portions were considered for each cross-section, subdividing the thickness into three parts and using a strain-sensor placed in the centre of each part. This allows comparing the traditional process with the constrained solution.

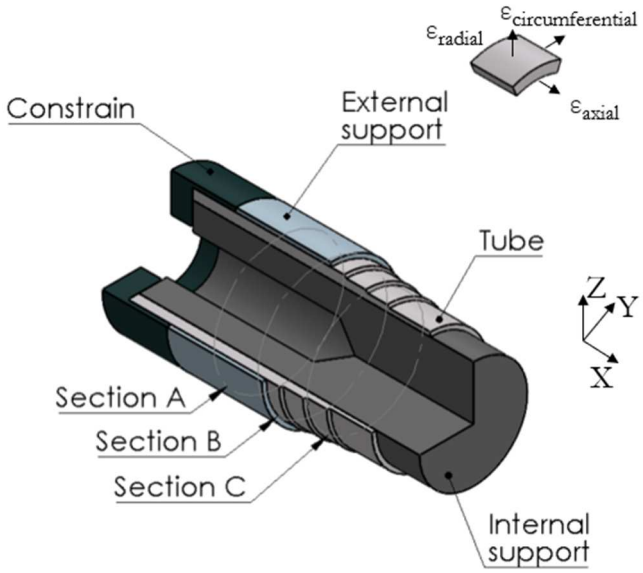

Fig. 4.7 *- Schematic representation of analyses cross-sections.*

To reduce the number of simulations necessary to have a good knowledge of the process, average values of some parameters were chosen, analysing the influence of parameters kept free. Having optimized the latter, it proceeded by varying those that had previously been kept fixed. In particular, the rollers parameters are the same as the traditional backward tube flowforming, to have the possibility to use part of the same setup for the two processes.

4.3.1 FE Model

Fig. 4.8 shows the numerical model setup, in which the three rollers, the mandrel, and the radial constraint were modelled as rigid bodies while the workpiece was meshed as a deformable body by using elements with different mesh sizes.

In particular for the workpiece, as reported in Fig. 4.4 for the traditional backward tube flowforming, under the rollers, the elements were sliced by a 3 deg angle, while in the rest of the workpiece, a 10 deg angle elements were used. A tube length of 70 mm was used to ensure process stability and investigate differences along the axial direction, while the total stroke of the rollers was fixed at a value equal to 35 mm. The inner and outer diameters were respectively equal to 25 mm and 30 mm. Two backward flowforming passes were numerically simulated, taking as target values the results in terms of strain and forces obtained with the traditional incremental backward

tube flowforming, considering different thickness reduction. As the previous model, to simulate the effect of the tailstock and the tube rotation, the nodes at one end of the workpiece were constrained in the axial and angular directions.

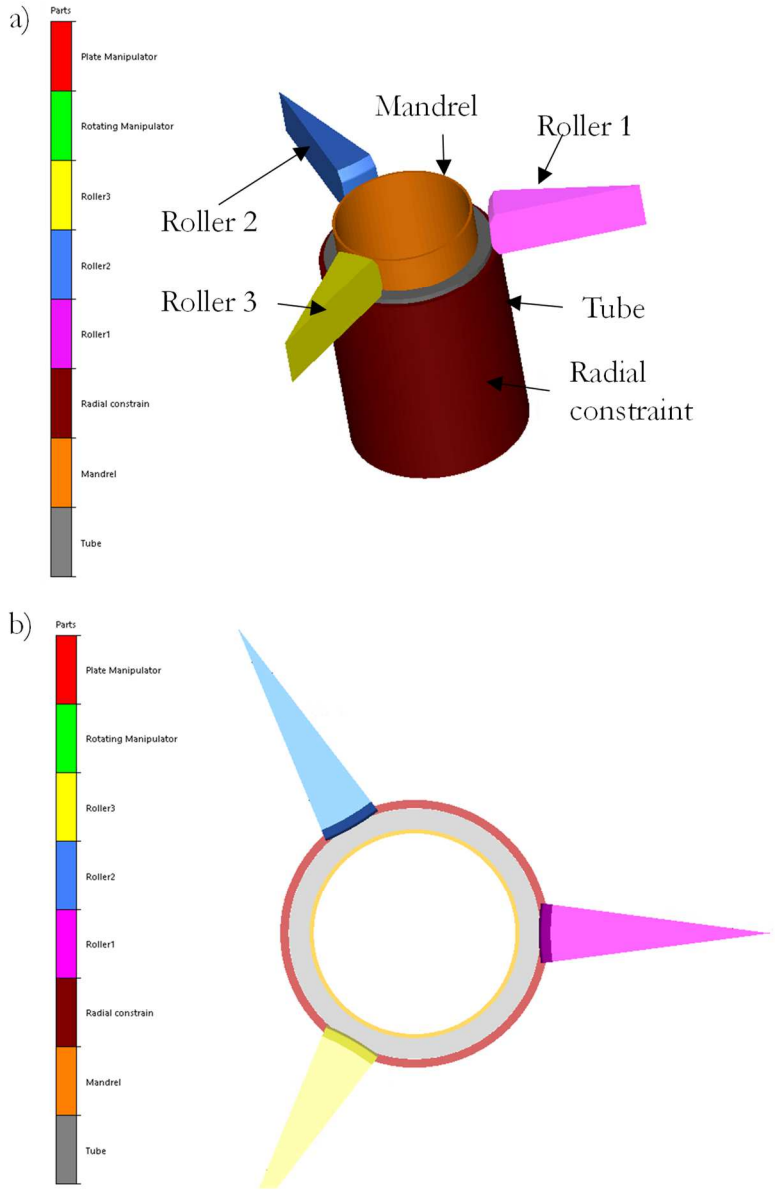

Fig. 4.8 *- Numerical FE model of constrained backward flowforming: (a) perspective view; (b) lateral view.*

The workpiece is considered elastic-plastic, and it was modelled through the Hooke equation for stress lower than σ_Y and with the Hollomon equation for stress larger than σ_Y, as reported in the following equation:

$$\sigma = \begin{cases} E\varepsilon \text{ for } \sigma < \sigma_Y \\ K\varepsilon^n \text{ for } \sigma \geq \sigma_Y \end{cases} \qquad \textit{Eq. 4}$$

where the values of the coefficient K and n of the AA6082-T4 alloy are reported in

Chapter 3.

Since the process is carried out at room temperature, the temperature and strain rate effects were assumed negligible. A surface-to-surface contact was set between (i) the mandrel and the tube inner surface, (ii) the constrain and the tube outer surface, and (iii) the rollers and tube outer surface. The conditions (i) and (ii) were modelled according to the Coulomb equation, assuming a friction coefficient μ=0.1; for the condition (iii) a sliding without friction was assumed based on the fact that the contribution of the rolling friction was considered negligible in the experiments as proved by the absence of material flow in the circumferential direction. In this case, the surface defects are controlled by the presence of the radial constraint. Ideally, it is possible to increase the strain with this innovative process due to a radial strain component. This means that with the same thickness reduction imposed by the rollers, the strain in the constrained solution is higher compared with the traditional backward tube flowforming process. The influence of axial and radial rollers' positions on the strain distribution was evaluated. Variable rotational speeds and rollers feed rates were selected to investigate the influence of different kinematics parameters.

4.3.2 Geometrical parameters

Using the results reported in Section 4.4.1.1, the geometry of the roller was not investigated again. Focusing on the (i) axial and (ii) radial position of the rollers, fewer simulations were necessary to optimize the process. The axial offset configurations that were numerically simulated are reported in Tab. 4.6, while the thickness reduction configurations are reported in Tab. 4.9. Due to the amount of total deformation reached with multiple passes, since there is the possibility to act incrementally with the traditional backward tube flowforming process, the thickness reduction studied for the version with radial constraint provides a greater deformation per pass. The same strain is reached as in the traditional process after more passes, reducing the expenditure of time and comparing the results in strain distribution and axial forces. For the axial offset optimization, 5 simulations were necessary, imposing, in this case, a thickness reduction equal to 0.10 mm for each roller, while the kinematics parameters consist of a 2 mm/s feed rate and 420 rpm mandrel angular speed.

***Tab. 4.6** - Axial offset optimization for the rollers.*

#	a (mm)
1	0.5
2	1
3	1.5
4	2
5	2.5

Another geometrical parameter that needs to be investigated is the axial length *l'*

of the radial constraint, as reported in Fig. 4.7, to understand the stability of the simulation and issues related to the build-up or bulge defects. The values are reported in Tab 4.7. Ideally, this solution avoids the formation of the build-up defect, constraining the material in the radial direction. However, at the end of the constrain in the axial direction, part of the material, pushed by the action of the rollers, could expand, increasing the tube diameter and the force necessary for the advancement of the rollers. Also in this case, a thickness reduction equal to 0.10 mm for each roller was imposed, while the kinematics parameters consist of a 2 mm/s feed rate and 420 rpm mandrel angular speed.

Tab. 4.7 *- Radial constraint length.*

#	l' (mm)
1	20
2	25
3	30
4	35

4.3.3 Kinematics parameters

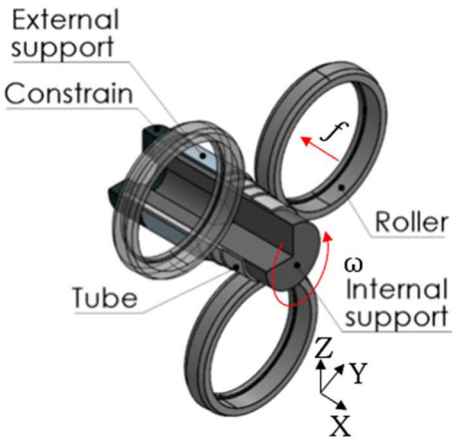

Fig. 4.9 *- Kinematics parameters.*

Tab. 4.8 *- Kinematics parameters optimization.*

f (mm/s)	ω (rpm)
0.5	240
1	420
1.5	600
2	

As for the backward tube flowforming, also in the constrained solution, the values of the kinematics parameters being analysed are the roller feed *f* and the rotational speed of the tube *ω*, as reported in Fig. 4.9, because the radial constraint is integral

with the rollers. To reduce the number of simulations, the optimal geometrical parameters of axial offset and radial constraint length were adopted, while the kinematics values are the combination of the values reported in Tab. 4.8. The total simulations are 12, considering a thickness reduction imposed by each roller equal to 0.15 mm.

4.3.4 Thickness reduction

Tab. 4.9 *- Thickness reduction optimization for each roller.*

Δt_1 (mm)	Δt_2 (mm)	Δt_3 (mm)
0.10	0.10	0.10
0.20	0.20	0.20
0.30	0.30	0.30

Optimized the previous parameters, for the thickness reduction optimization, 27 simulations were necessary. In this case, the thickness reduction per pass is higher than the traditional backward tube flowforming due to the presence of the radial constraint, which ideally avoids the build-up defect. The outputs of these simulations are the presence or absence of surface defects and the total amount of axial loads. Ideally, the higher the thickness reduction per pass, the higher the axial load.

4.3.5 Incremental process

Once the radial position of the rollers has been chosen to reduce surface defects and minimize the axial force required to complete the process, several passes on the same tube can be performed. The initial and final thicknesses of the tube after each pass of the incremental process and the percentage reduction in thickness for each roller are shown in Tab. 4.10. In this case, only two passes were performed, equivalent to a thickness reduction of 48%. Following what is described in Section 4.4.2.4 regarding the interpenetration of the rollers, a solution was chosen which guaranteed the absence of surface defects, moderate axial loads, and balanced deformation on each roll. The results of these simulations are reported in Chapter 8, comparing these with the experimental results in terms of microhardness, microstructure, mechanical properties, and tube elongation.

Tab. 4.10 *- Incremental process simulation details.*

#	$t_{initial}$ (mm)	t_{final} (mm)	Δt_1 (mm)	Δt_2 (mm)	Δt_3 (mm)
1	2.50	1.90	-8%	-8%	-8%
2	1.90	1.30	-8%	-8%	-8%

4.4 Process parameters results

4.4.1 Backward Tube Flowforming

This section reports the results of numerical simulations in backward tube flowforming, distinguishing the results in elongation, strain distribution, and axial forces as the process parameters vary. In analysing the results, the areas of interest were chosen as those shown in Fig. 4.2, using sensors corresponding to an internal, middle, and external portion of the tube.

4.4.1.1 Roller parameters

Using the geometric parameters reported in Tab. 4.11 for the roller geometry, 48 simulations were performed, using a constant feed rate equal to 2 mm/s, a rotation speed of 420 rpm and a thickness reduction of 0.1 mm for each roller. Fig. 4.10 reports the tube elongation as the geometrical parameters of the roller vary. It is possible to notice how increasing the forming angle α dispersion of the results is higher, depending on the fillet radius.

Tab. 4.11 *- Rollers geometry optimization simulations details.*

#	α (deg)	β (deg)	γ (deg)	l (mm)	r (mm)
1	20	20	3	3	1
2	20	20	3	3	5
3	20	20	3	5	1
4	20	20	3	5	5
5	20	20	5	3	1
6	20	20	5	3	5
7	20	20	5	5	1
8	20	20	5	5	5
9	20	30	3	3	1
10	20	30	3	3	5
11	20	30	3	5	1
12	20	30	3	5	5
13	20	30	5	3	1
14	20	30	5	3	5
15	20	30	5	5	1
16	20	30	5	5	5
17	25	20	3	3	1
18	25	20	3	3	5
19	25	20	3	5	1
20	25	20	3	5	5
21	25	20	5	3	1
22	25	20	5	3	5

23	25	20	5	5	1
24	25	20	5	5	5
25	25	30	3	3	1
26	25	30	3	3	5
27	25	30	3	5	1
28	25	30	3	5	5
29	25	30	5	3	1
30	25	30	5	3	5
31	25	30	5	5	1
32	25	30	5	5	5
33	30	20	3	3	1
34	30	20	3	3	5
35	30	20	3	5	1
36	30	20	3	5	5
37	30	20	5	3	1
38	30	20	5	3	5
39	30	20	5	5	1
40	30	20	5	5	5
41	30	30	3	3	1
42	30	30	3	3	5
43	30	30	3	5	1
44	30	30	3	5	5
45	30	30	5	3	1
46	30	30	5	3	5
47	30	30	5	5	1
48	30	30	5	5	5

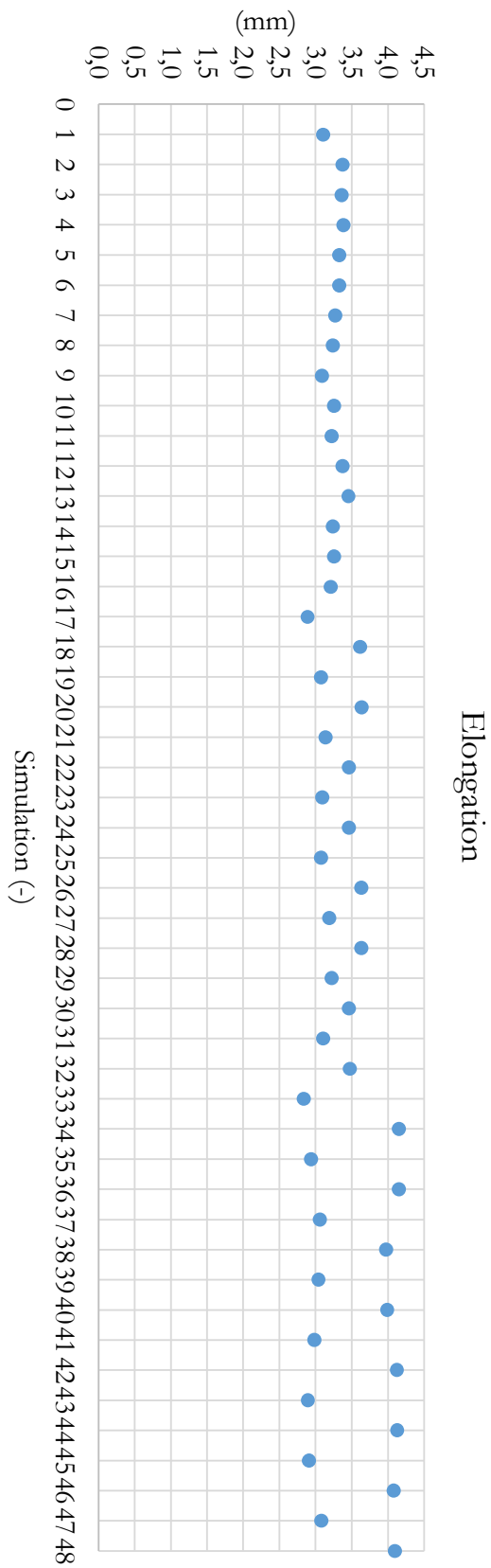

Fig. 4.10 *- Tube elongation for different roller configurations.*

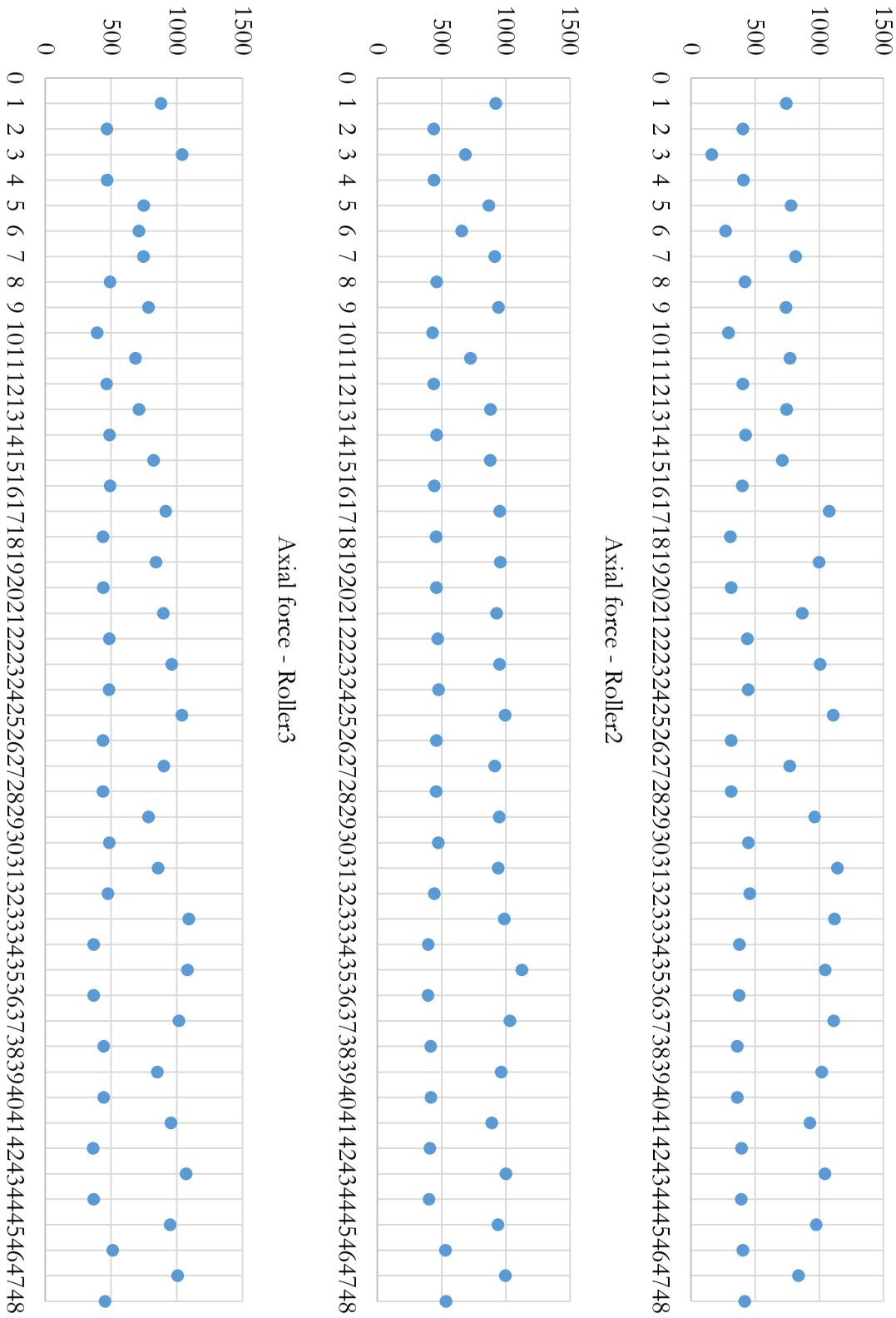

Fig. 4.11 *- Axial force for different roller configurations.*

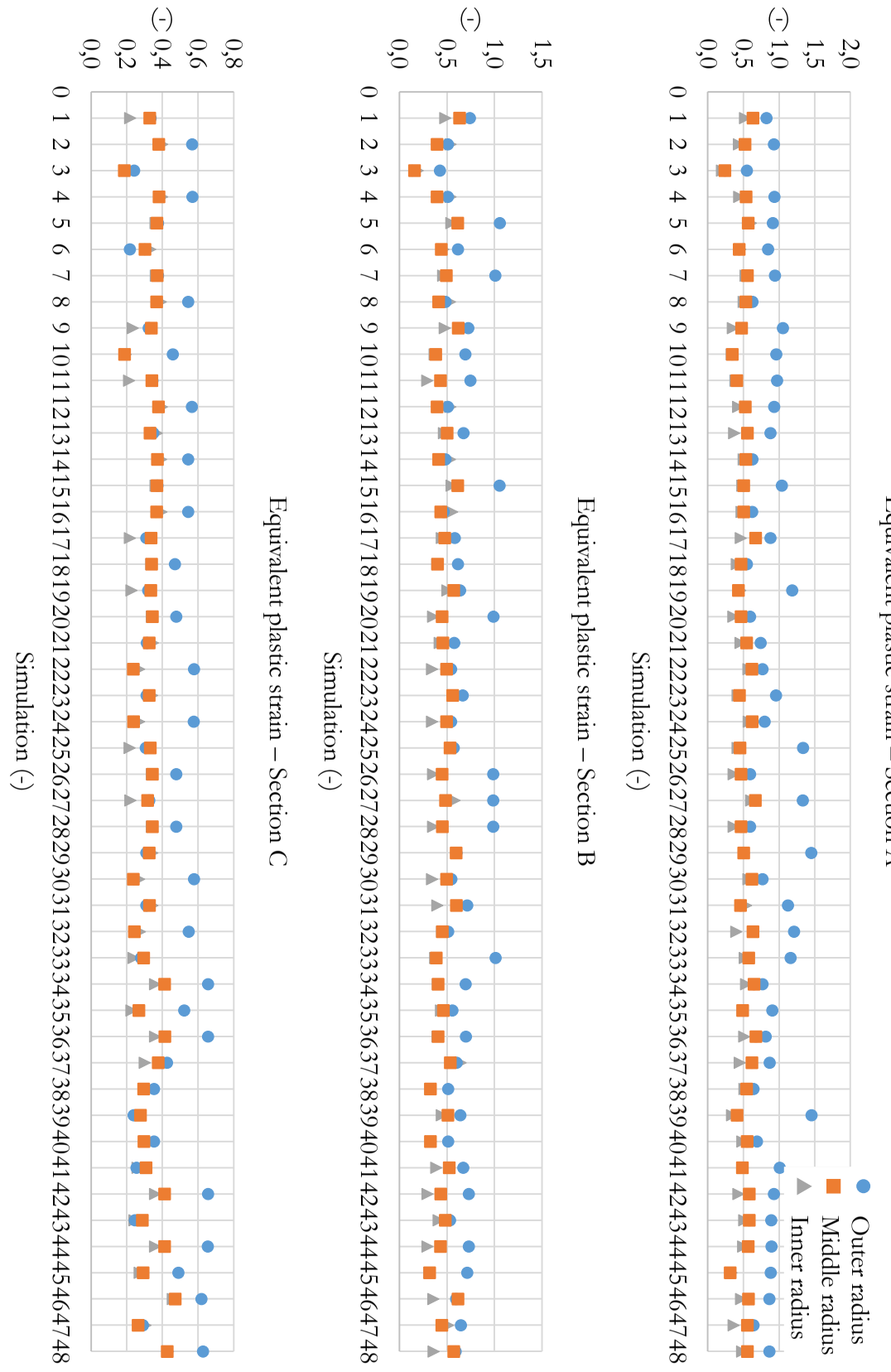

Fig. 4.12 *- Eq. plastic strain for different roller configurations.*

Tab. 4.12 *- Roller optimal geometrical parameters.*

α (deg)	β (deg)	γ (deg)	l (mm)	r (mm)
25	30	3	5	1

Analysing the results in terms of axial force, shown in Fig. 4.11 for each roller, and the distribution of deformation for each section, shown in Fig. 4.12, it is possible to note that axial loads are very often associated with higher elongation values. However, it can be observed that the average strain is maximum for the geometric values shown in Tab. 4.12. In particular, it is possible to notice how with different geometrical parameters, it is possible to obtain similar strain values. For this reason, the optimal geometric parameters were compared with those found in the literature, and a configuration as intermediate as possible was chosen, with similar strain distribution.

4.4.1.2 Axial offset

The values of axial offset *a*, reported in Tab. 4.2, are used with the roller's parameter reported in Tab. 4.12, providing 5 possible configurations. In this case, all the results regarding the external portion of the tube are reported in Tab. 4.13.

Tab. 4.13 *- Roller axial offset optimization results.*

#	a (mm)	$\varepsilon_{A\text{-}ext}$ (-)	$\varepsilon_{B\text{-}ext}$ (-)	$\varepsilon_{C\text{-}ext}$ (-)
1	0.5	0.77	0.58	0.41
2	1	0.55	0.79	0.40
3	1.5	1.01	0.67	0.33
4	2	0.81	0.62	0.33
5	2.5	0.90	0.54	0.33

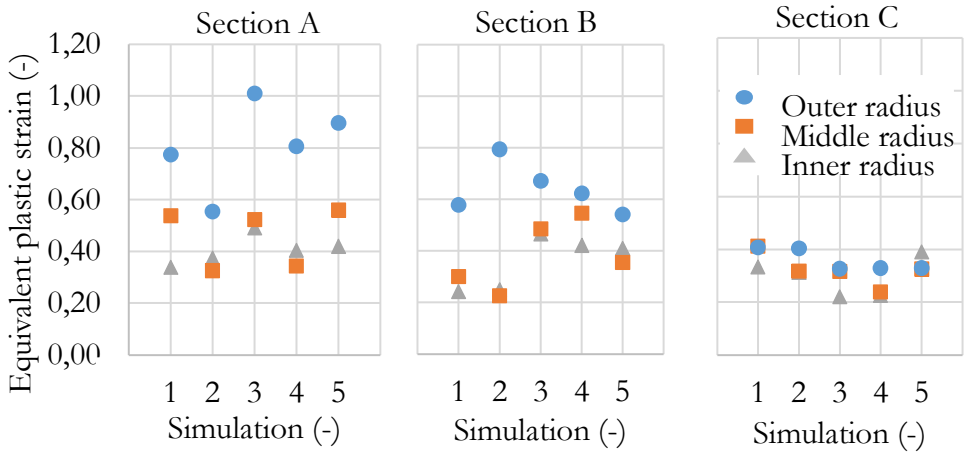

Fig. 4.13 *- Equivalent plastic strain for different cross-sections.*

It is possible to observe how the average higher equivalent plastic strain value is obtained with an axial roller offset equal to 1.5 mm, as shown in Fig. 4.13. The picture

compares each radius for different cross-sections, varying the axial offset among the rollers. Considering these five configurations, it is possible to measure the elongation of the tube after the process. The results, reported in Fig. 4.14a, show that the higher the strain, the higher the tube elongation and that an axial offset between 1.5 mm and 2 mm optimizes this value. However, considering the axial force generated during the process, as reported in Fig. 4.14b, the lower value is obtained with an offset of 1.5 mm. This configuration minimizes the axial force and maximizes not only the elongation but also the equivalent plastic strain. For these reasons, an axial offset among the roller of 1.5 mm was chosen.

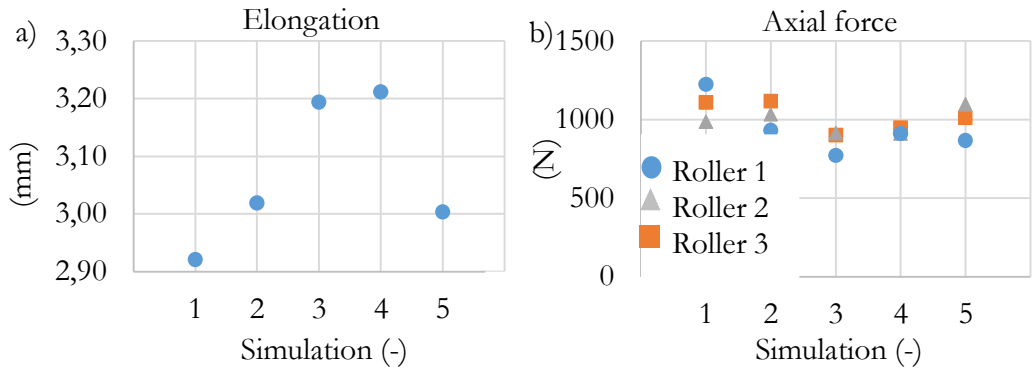

Fig. 4.14 *- a) Tube elongation and b) axial force for each roller considering different axial offset*

4.4.1.3 Kinematics parameters

Tab. 4.14 *- Kinematics parameters optimization details.*

#	*f* (mm/s)	ω (rpm)
1	0.5	240
2	0.5	420
3	0.5	600
4	1.0	240
5	1.0	420
6	1.0	600
7	1.5	240
8	1.5	420
9	1.5	600
10	2.0	240
11	2.0	420
12	2.0	600

Using the feed rate and mandrel speed parameters reported in Tab. 4.14, 12 simulations were performed, using the optimal geometrical parameters for each roller and a thickness reduction for each roller equal to 0.05 mm. The output parameters that must be optimized are the elongation of the tube, the axial load, and the equivalent

plastic strain. Fig. 4.15a reports the tube elongation as the kinematics parameters of the process varies. It is possible to notice how the tube elongation decreases by increasing the feed rate, while a mandrel speed increase affects the tube elongation. Analysing the results of axial forces, as reported in Fig. 4.15b, it is possible to observe that increasing the mandrel speed lower the axial load while increasing the feed rate, the average axial forces of the three rollers remain constant.

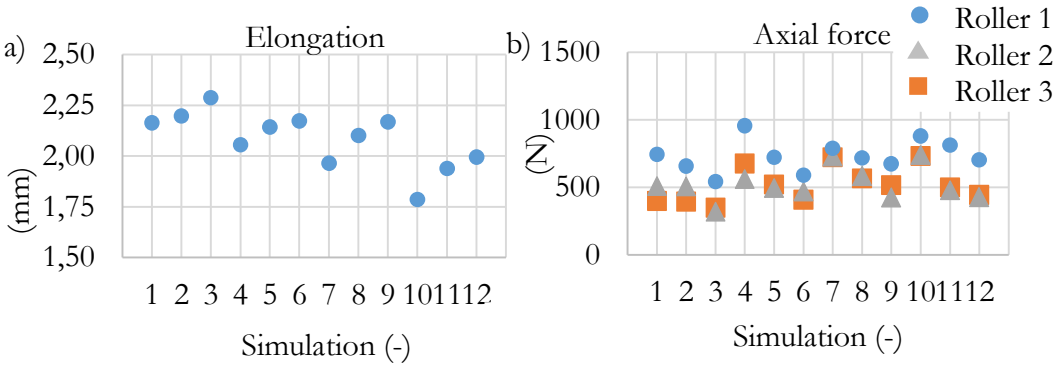

Fig. 4.15 *- a) Tube elongation and b) axial force for different kinematic configurations.*

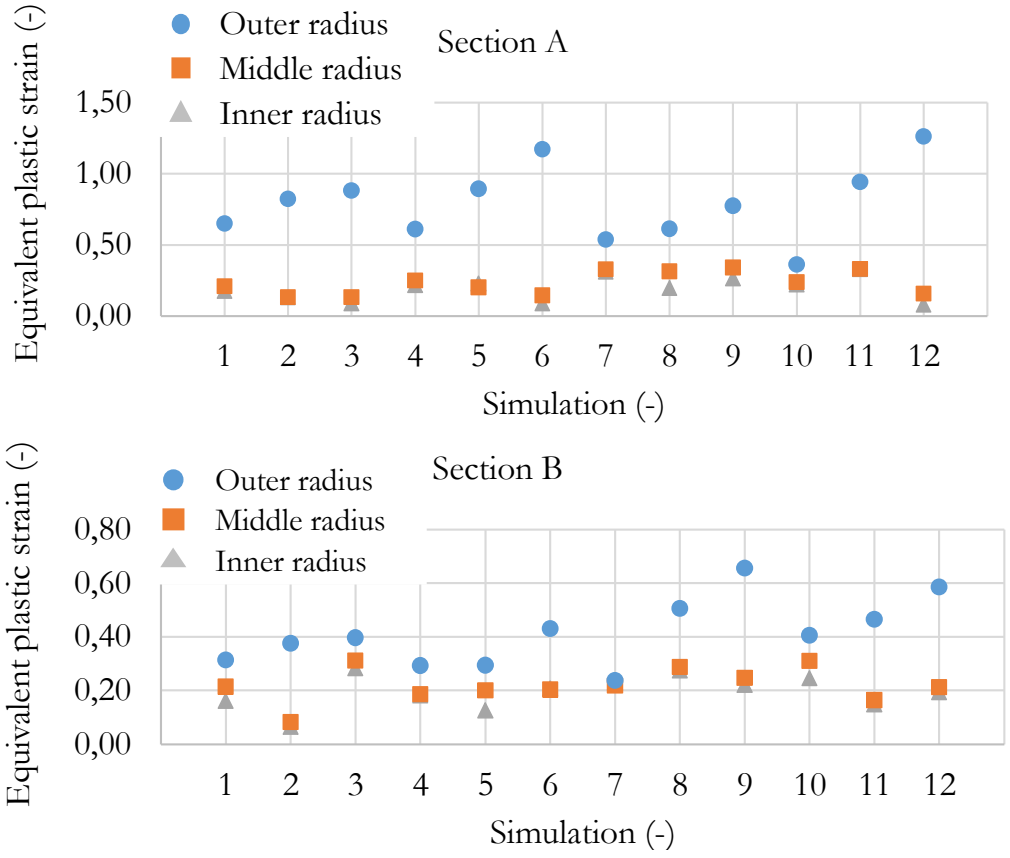

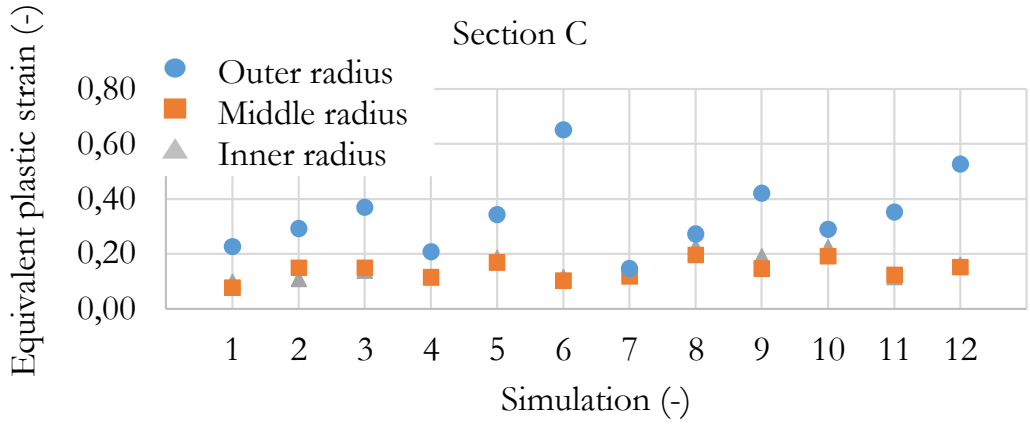

Fig. 4.16 *- Eq. plastic strain distribution considering different kinematic configurations.*

Considering the equivalent plastic strain, as shown in Fig. 4.16, it is possible to observe that the higher the mandrel speed and the feed rate higher the equivalent plastic strain in the outer portion of the tube. However, it is possible to notice how the trend of the equivalent plastic strain of the middle and inner portion is different if compared with the outer. In particular, constant values are obtained varying the kinematics parameters.

Intermediate kinematics parameters were chosen, which considered different influencing trends, as reported in Tab. 4.15, and in particular, a feed rate equal to 2 mm/s and a mandrel angular speed equal to 420 rpm.

Tab. 4.15 *- Eq. plastic strain with different kinematic parameters.*

#	*f* (mm/s)	ω (rpm)	$\varepsilon_{A\text{-}i}$ (-)	$\varepsilon_{A\text{-}m}$ (-)	$\varepsilon_{A\text{-}e}$ (-)	$\varepsilon_{B\text{-}i}$ (-)	$\varepsilon_{B\text{-}m}$ (-)	$\varepsilon_{B\text{-}e}$ (-)	$\varepsilon_{C\text{-}i}$ (-)	$\varepsilon_{C\text{-}m}$ (-)	$\varepsilon_{C\text{-}e}$ (-)	$\varepsilon_{aver.}$ (-)
1	0.5	240	0.18	0.21	0.65	0.16	0.21	0.31	0.10	0.08	0.23	0.24
2	0.5	420	0.13	0.14	0.83	0.07	0.08	0.78	0.11	0.15	0.42	0.30
3	0.5	600	0.09	0.13	0.88	0.28	0.31	0.40	0.14	0.15	0.37	0.31
4	1.0	240	0.22	0.25	0.61	0.18	0.19	0.29	0.12	0.12	0.21	0.24
5	1.0	420	0.23	0.20	0.90	0.13	0.20	0.30	0.19	0.17	0.34	0.29
6	1.0	600	0.09	0.15	1.17	0.21	0.20	0.43	0.12	0.10	0.65	0.35
7	1.5	240	0.31	0.33	0.54	0.23	0.22	0.24	0.15	0.12	0.15	0.25
8	1.5	420	0.20	0.32	0.42	0.27	0.29	1.05	0.23	0.20	0.37	0.37
9	1.5	600	0.27	0.34	0.78	0.22	0.25	0.40	0.19	0.15	0.42	0.33
10	2.0	240	0.22	0.24	0.36	0.25	0.31	0.39	0.22	0.19	0.29	0.28
11	2.0	420	0.33	0.33	0.94	0.15	0.16	0.26	0.12	0.12	0.16	0.29
12	2.0	600	0.08	0.16	1.27	0.19	0.21	0.28	0.16	0.15	0.53	0.34

4.4.1.4 Thickness reduction

For the thickness reduction imposed by each roller, the output parameter of the simulation is not the equivalent strain because obviously higher the thickness reduction, the higher the equivalent plastic strain, but the presence of surface defects

and the axial loads needed to perform the process. Considering different combinations of thickness reduction imposed by the rollers, it is possible to set the optimal one. Fig. 4.17 shows the build-up defect generated by the first roller, as its interpenetration is equal to 0.15 mm (configuration 15).

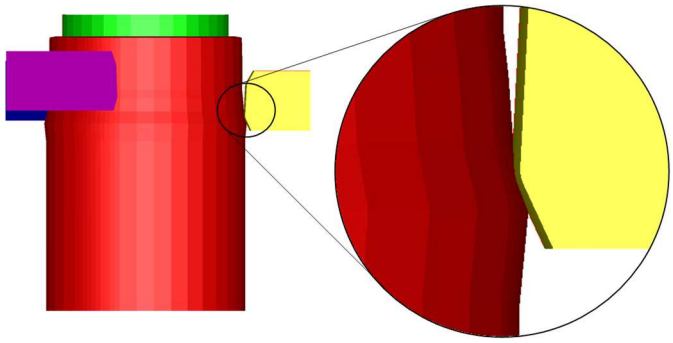

Fig. 4.17 *- Example of build-up defect (configuration 15).*

The results of the other configurations, in terms of maximum axial force among the three rollers and the presence or absence of build-up, are shown in Tab. 4.16. To reduce the total amount of axial loads and avoid the build-up defects, configuration 1 was chosen, with a constant relative interpenetration for each roller equal to 0.05 mm. To increase the total amount of strain, different passes were performed, as reported in Section 4.2.5.

Tab. 4.16 *- Results of the thickness reduction optimization.*

#	Δt_1 (mm)	Δt_2 (mm)	Δt_3 (mm)	F_1 (N)	F_2 (N)	F_3 (N)	F_{TOT} (N)	build-up (-)
1	0.05	0.05	0.05	823	474	500	1797	no
2	0.05	0.05	0.15	1016	709	1326	3051	no
3	0.05	0.05	0.30					yes
4	0.05	0.15	0.05	1023	1105	493	2621	no
5	0.05	0.15	0.15	1257	1130	1230	3617	no
6	0.05	0.15	0.30					yes
7	0.05	0.30	0.05					yes
8	0.05	0.30	0.15					yes
9	0.05	0.30	0.30					yes
10	0.15	0.05	0.05					yes
11	0.15	0.05	0.15	1417	708	1103	3228	no
12	0.15	0.05	0.30					yes
13	0.15	0.15	0.05	1150	833	616	2599	no
14	0.15	0.15	0.15					yes
15	0.15	0.15	0.30					yes
16	0.15	0.30	0.05					yes
17	0.15	0.30	0.15					yes
18	0.15	0.30	0.30					yes

19	0.30	0.05	0.05					yes
20	0.30	0.05	0.15					yes
21	0.30	0.05	0.30					yes
22	0.30	0.15	0.05					yes
23	0.30	0.15	0.15					yes
24	0.30	0.15	0.30					yes
25	0.30	0.30	0.05					yes
26	0.30	0.30	0.15					yes
27	0.30	0.30	0.30					yes

4.4.2 Constrained Backward Tube Flowforming

This section reports the results of numerical simulations in the constrained backward tube flowforming, distinguishing the results in elongation, strain distribution, and axial forces as the process parameters vary. In analysing the results, the areas of interest were chosen as those shown in Fig. 4.7, using sensors corresponding to an internal, middle, and external portion of the tube.

4.4.2.1 Axial offset

The values of axial offset *a*, reported in Tab. 4.6, are used with the rollers parameters reported in Tab. 4.12, considering a thickness reduction for each roller equal to 0.15 mm, providing 5 possible configurations object to analysis. In this case, all the results regarding the external portion of the tube are reported in Tab. 4.17.

Tab. 4.17 *- Roller axial offset optimization results.*

#	a (mm)	$\varepsilon_{A\text{-}ext}$ (-)	$\varepsilon_{B\text{-}ext}$ (-)	$\varepsilon_{C\text{-}ext}$ (-)
1	0.5	0.79	0.94	0.81
2	1	1.30	1.03	0.51
3	1.5	1.63	1.23	1.39
4	2	1.57	1.17	1.30
5	2.5	1.45	1.15	0.86

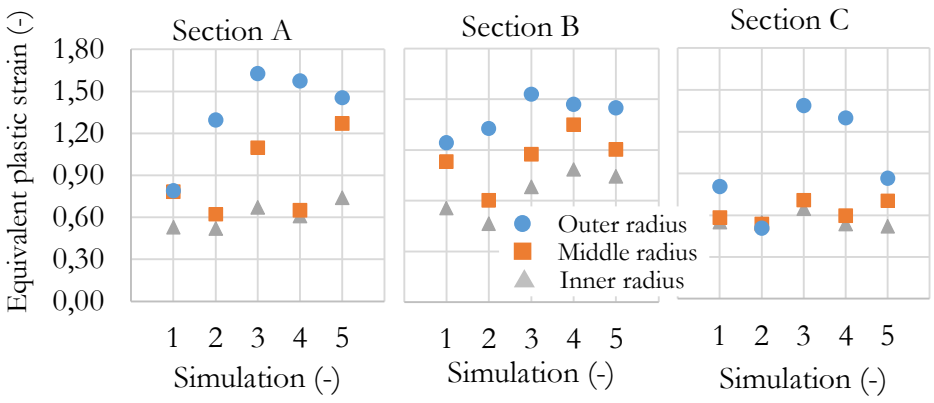

Fig. 4.18 *- Equivalent plastic strain for different cross-sections.*

It is possible to notice how the average strain values are maximum for an axial roller offset equal to 1.5 mm, as shown in Fig. 4.18. The picture compares each radius for different cross-sections, varying the axial offset among the rollers. It is possible to observe how the average higher equivalent plastic strain value is obtained with an axial offset equal to 1.5 mm. Considering these 5 configurations, it is possible to measure the elongation of the tube after the process.

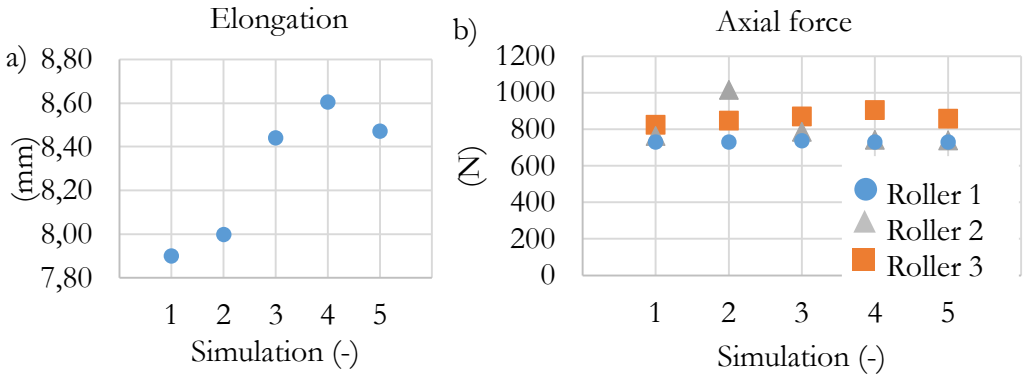

Fig. 4.19 *- a) Tube elongation and b) axial force for each roller considering different axial offset.*

The results, reported in Fig. 4.19a, show that the higher strain values are correlated with higher tube elongation and that an axial offset between 1.5 mm and 2.5 mm optimizes this value. However, considering the axial force generated during the process, as reported in Fig. 4.19b, similar values are obtained, with different axial offset configurations. An axial offset equal to 1.5 mm compromises low axial force, high tube elongation and equivalent plastic strain. For these reasons, an axial offset among the rollers equal to 1.5 mm was chosen.

4.4.2.2 Radial constraint length

Once the optimal value of the axial offset among the rollers has been set, it is possible to optimize the length of the radial constraint. It is important to understand the influence of this parameter because it could generate or avoid surface defects by sliding on the tube. Considering the parameters reported in Tab 4.7, 4 simulations were done, using fixed kinematics parameters. In particular, a feed rate equal to 2 mm/s and a mandrel angular velocity equal to 420 rpm were used. The output parameters that need to be minimized are the build-up defect and the axial force. On the other hand, the equivalent plastic strain is a parameter that needs to be maximized. This solution allows constraining the material that the roller tends to carry forward, allowing to increase the thickness reduction that in these cases is set equal to 0.15 mm for each roller. Fig. 4.20 represents the reduction of the build-up of material with a reduction in thickness that would have led to the formation of this defect in the traditional case. This means that the assumption of the possibility of increase the strain without defects is verified numerically, and it is possible to reduce the number of passes needed with

the same strain distribution.

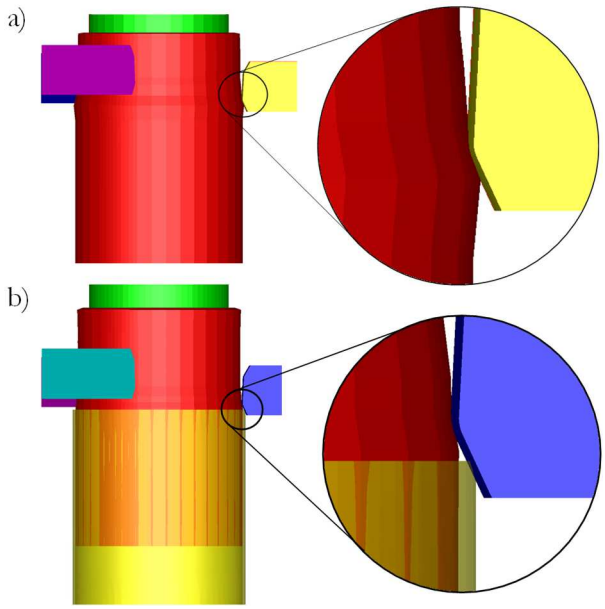

Fig. 4.20 *- Comparison between a) traditional and b) constrained backward tube flowforming.*

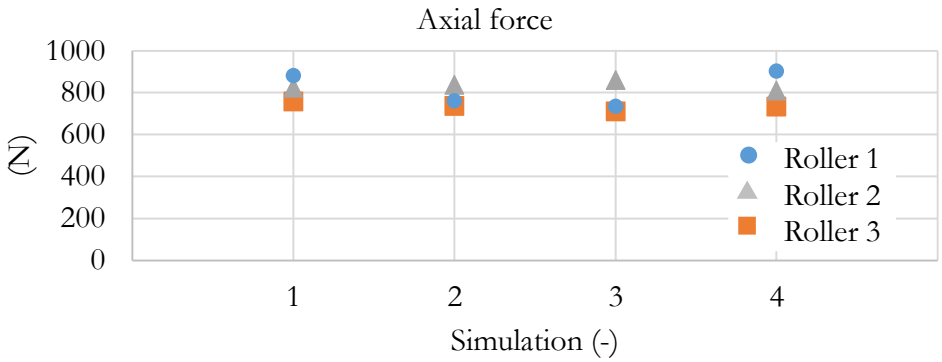

Fig. 4.21 *- Axial force for each roller considering different lengths for the radial constraint.*

Analysing the results obtained, as the length of the radial constraint increases, no differences are noted in the formation of the build-up defect near the rollers. However, as the length decreases, a circular band of work-hardened material forms, which opposes the sliding of the radial constraint. It is possible to observe how increasing the length of radial constraint, the axial force remains constant, as reported in Fig. 4.21, while this geometrical parameter also affects the strain distribution, reported in Fig. 4.22. Comparing the results of the constrained solution with the traditional backward flowforming, equalling the reduction in thickness, it is possible to note how the constrained solution allows obtaining higher strain values. This means that it is necessary to perform fewer passes to obtain the same deformation. A constrain that compresses the material radially along its entire length makes it possible to reach on average higher deformation values, as shown in Fig. 4.22.

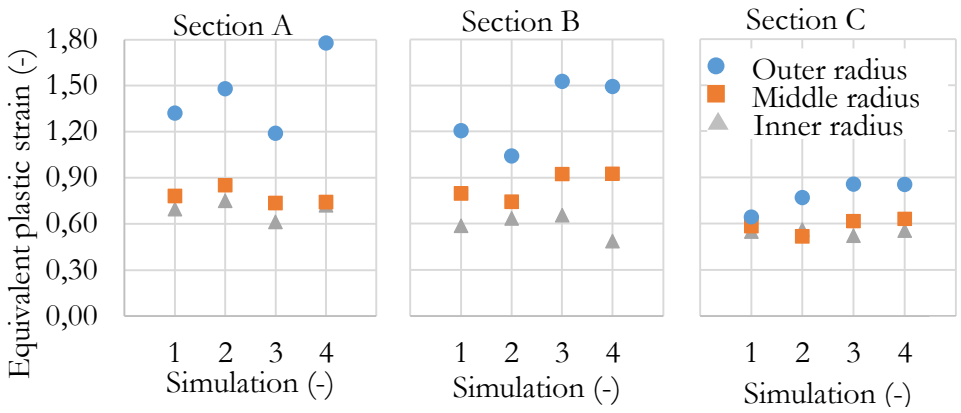

Fig. 4.22 *- Equivalent plastic strain for different cross-sections.*

4.4.2.3 Kinematics parameters

Using the feed rate and mandrel speed parameters reported in Tab. 4.18, 12 simulations were performed, using the optimal geometrical parameters for each roller and a thickness reduction for each roller equal to 0.15 mm. The output parameters that must be optimized are the elongation of the tube, the axial load, and the equivalent plastic strain.

Tab. 4.18 *- Kinematics parameters optimization details.*

#	f(mm/s)	ω (rpm)
1	0.5	240
2	0.5	420
3	0.5	600
4	1.0	240
5	1.0	420
6	1.0	600
7	1.5	240
8	1.5	420
9	1.5	600
10	2.0	240
11	2.0	420
12	2.0	600

Fig. 4.23a reports the tube elongation as the kinematics parameters of the process vary. It is possible to notice how increasing the feed rate the tube elongation decreases while increasing the mandrel speed there is a positive effect on the tube elongation. Analysing the results of axial forces, as reported in Fig. 4.23b, it is possible to observe that the higher the mandrel speed the lower the axial loads and that the feed rate does not affect this parameter. Comparing these distributions with the traditional solution, it is possible to notice a lower difference among the rollers.

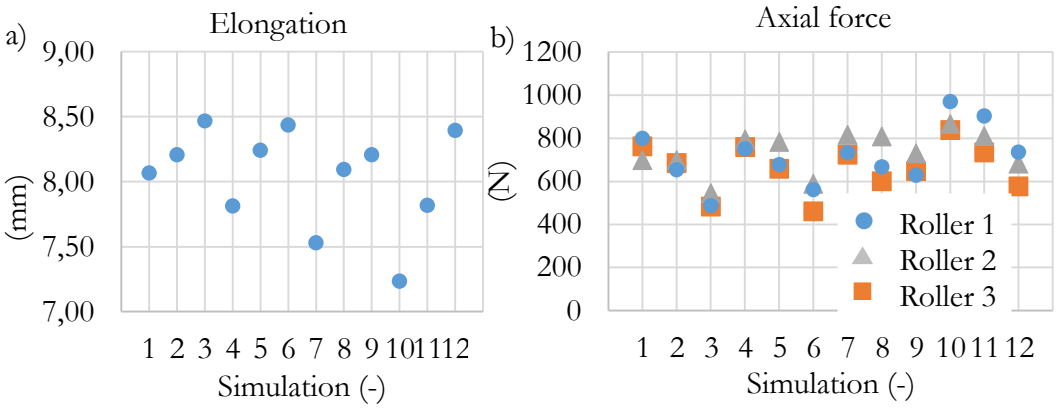

Fig. 4.23 *- a) Tube elongation and b) axial force for different kinematic configurations.*

Considering the equivalent plastic strain, as shown in Fig. 4.24, it is possible to observe that the higher the mandrel speed higher the equivalent plastic strain considering Section *A* and *B*. At the same time, the feed rate affects with a positive trend the equivalent plastic strain considering Section *A* and *B*. Section *C* follows an inverse trend: increasing the mandrel speed or the feed rate, the equivalent plastic strain decreases. However, as reported in Tab. 4.19, it is possible to notice how with different combinations of the kinematics parameters, it is possible to obtain similar strain values. For this reason, intermediate parameters were chosen, which took into account different influencing trends, with a feed rate equal to 1.5 mm/s and a variable mandrel speed, considering this parameter equal to 240 rpm, 420 rpm and 600 rpm.

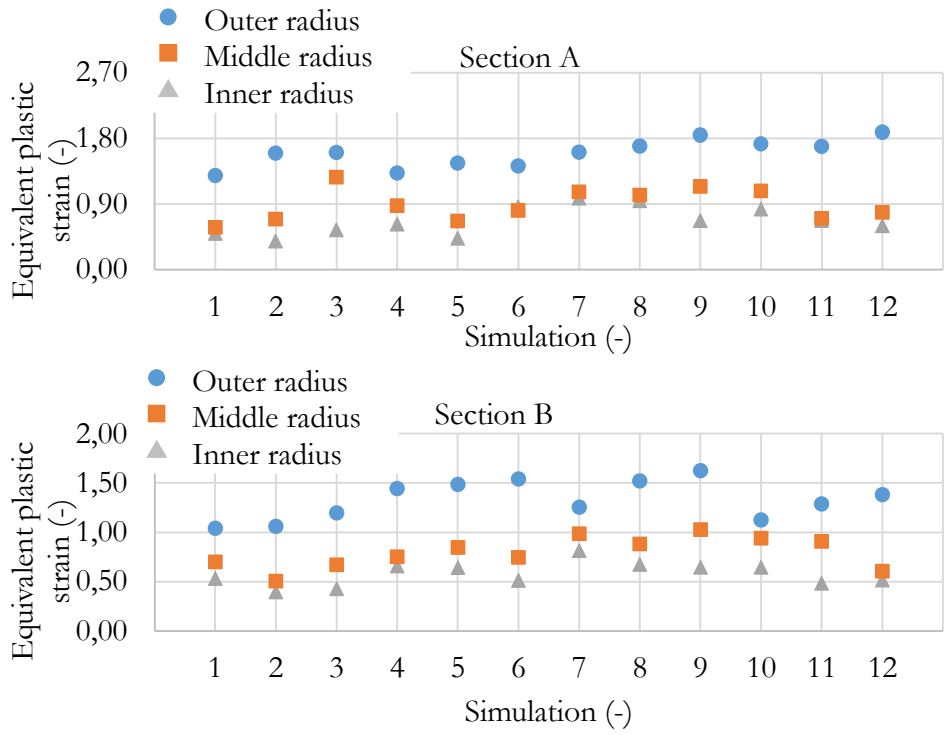

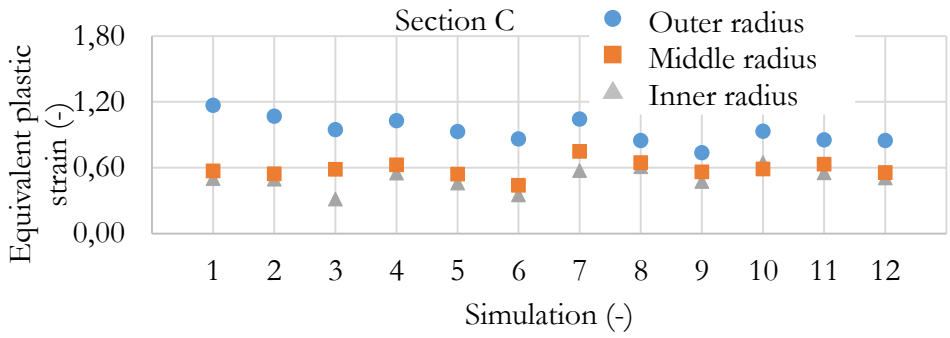

Fig. 4.24 *- Equivalent plastic strain distribution considering different kinematic configurations*

Tab. 4.19 *- Eq. plastic strain with different kinematic parameters.*

#	*f* (mm/s)	ω (rpm)	$\varepsilon_{A\text{-}i}$ (-)	$\varepsilon_{A\text{-}m}$ (-)	$\varepsilon_{A\text{-}e}$ (-)	$\varepsilon_{B\text{-}i}$ (-)	$\varepsilon_{B\text{-}m}$ (-)	$\varepsilon_{B\text{-}e}$ (-)	$\varepsilon_{C\text{-}i}$ (-)	$\varepsilon_{C\text{-}m}$ (-)	$\varepsilon_{C\text{-}e}$ (-)	$\varepsilon_{aver.}$ (-)
1	0.5	240	0.50	0.58	1.29	0.53	0.70	1.04	0.50	0.57	1.17	0.77
2	0.5	420	0.39	0.70	1.60	0.40	0.51	1.06	0.49	0.55	1.07	0.75
3	0.5	600	0.55	1.27	1.61	0.43	0.67	1.20	0.32	0.59	0.95	0.84
4	1.0	240	0.63	0.88	1.33	0.66	0.75	1.44	0.55	0.63	1.03	0.88
5	1.0	420	0.43	0.67	1.46	0.64	0.85	1.49	0.46	0.54	0.93	0.83
6	1.0	600	0.86	0.82	1.43	0.51	0.75	1.54	0.35	0.44	0.86	0.84
7	1.5	240	0.98	1.07	1.62	0.82	0.99	1.26	0.57	0.75	1.04	1.01
8	1.5	420	0.95	1.03	1.70	0.68	0.88	1.52	0.61	0.65	0.85	0.98
9	1.5	600	0.67	1.14	1.85	0.64	1.03	1.63	0.48	0.56	0.74	0.97
10	2.0	240	0.83	1.08	1.73	0.65	0.94	1.13	0.65	0.59	0.93	0.95
11	2.0	420	0.67	0.71	1.69	0.48	0.91	1.29	0.55	0.63	0.85	0.87
12	2.0	600	0.61	0.79	1.89	0.52	0.61	1.38	0.51	0.56	0.85	0.86

4.4.2.4 Thickness reduction

For the thickness reduction imposed by each roller, the output parameter of the simulations is the axial loads needed to perform the process. Considering different combinations of thickness reduction imposed by the rollers, it is possible to set the optimal one. The optimal configuration allows maximizing the strain having an axial load compatible with the maximum axial load available. In this case, the trade-off parameter is the axial force due to the radial constraint that allows minimizing the presence of the build-up defect. The result of the configurations, in terms of the maximum axial force of the three rollers, is shown in Tab. 4.20.

Tab. 4.20 *- Results of the thickness reduction optimization.*

#	Δt_1 (mm)	Δt_2 (mm)	Δt_3 (mm)	F_1 (N)	F_2 (N)	F_3 (N)	F_{TOT} (N)
1	0.10	0.10	0.10	1127	1156	944	3227
2	0.10	0.10	0.20	1229	1187	1337	3753

3	0.10	0.10	0.30	1336	1240	1817	4393
4	0.10	0.20	0.10	1173	1597	1226	3996
5	0.10	0.20	0.20	1296	1802	1242	4340
6	0.10	0.20	0.30	1381	1758	1880	5019
7	0.10	0.30	0.10	1210	1934	1246	4390
8	0.10	0.30	0.20	1263	2105	1625	4993
9	0.10	0.30	0.30	1377	2072	1658	5107
10	0.20	0.10	0.10	1461	1039	987	3486
11	0.20	0.10	0.20	1691	1415	1549	4655
12	0.20	0.10	0.30	1797	1142	1866	4804
13	0.20	0.20	0.10	1370	1395	978	3742
14	0.20	0.20	0.20	1516	1437	1371	4324
15	0.20	0.20	0.30	1588	1679	1807	5074
16	0.20	0.30	0.10	1586	2124	1405	5116
17	0.20	0.30	0.20	1691	2158	1890	5739
18	0.20	0.30	0.30	1898	2402	2245	6545
19	0.30	0.10	0.10	1931	1305	1344	4579
20	0.30	0.10	0.20	1962	1326	1747	5035
21	0.30	0.10	0.30	2008	1362	1825	5194
22	0.30	0.20	0.10	1836	1956	1125	4916
23	0.30	0.20	0.20	1894	1802	1781	5477
24	0.30	0.20	0.30	1851	1956	1911	5717
25	0.30	0.30	0.10	2107	2423	1335	5865
26	0.30	0.30	0.20	2065	2414	1744	6223
27	0.30	0.30	0.30	1976	2164	2373	6513

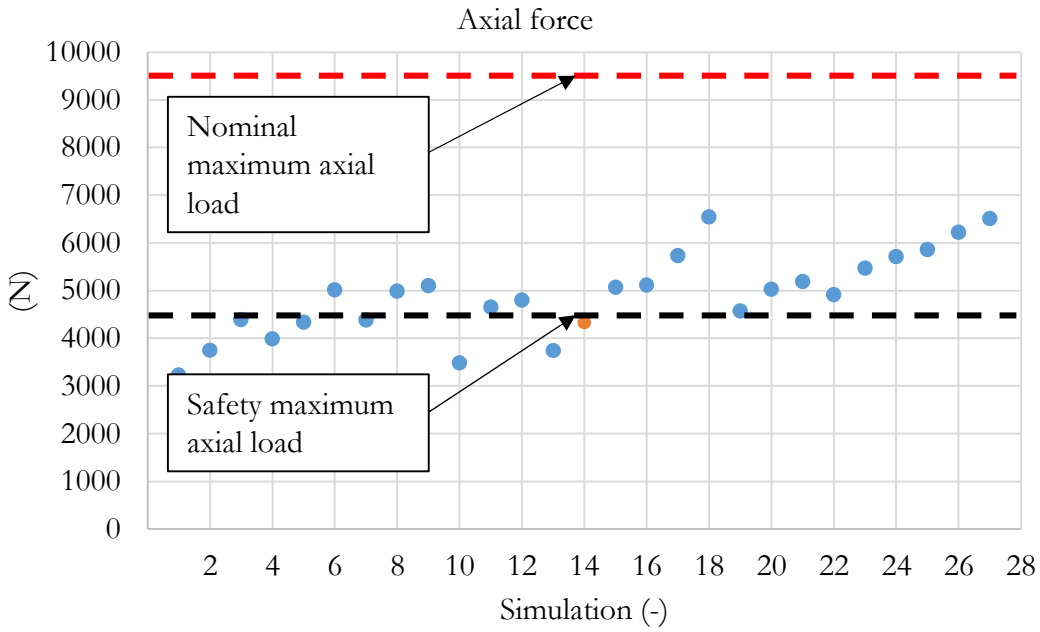

Fig. 4.25 *- Total axial force considering different thickness reductions.*

Fig. 4.25 reports the sum of the total axial load that the rollers need to perform the process. It is possible to notice that by increasing the total interpenetration of the rollers, the sum of the axial forces increases, accordingly with the theoretical result. To balance the axial loads among the rollers, an equal interpenetration is chosen, and to maximize the strain, the configuration with a reduction for each roller equal to 0.20 mm was chosen. The details regarding the nominal maximum axial force and the safety maximum axial force are given in Section 5.1 of Chapter 5.

Chapter 5

Experimental equipment

In this Chapter, the design of the experimental apparatus used to carry out the backward tube flowforming and the constrained backward tube flowforming are described, reporting the main reasons for the design operations and the CAD models. In addition, the experimental procedure used in the experiments is reported, while the exploded-view drawings are reported in the Appendix.

5.1 Mori Seiki™ *NL1500* CNC Lathe

A Mori Seiki™ *NL1500* CNC lathe shown in Fig. 5.1 was used to mount the experimental equipment developed using the FE models described in Chapter 4.

Fig. 5.1 *- Mori Seiki™ NL1500 CNC lathe.*

The datasheet of the machine is reported in Tab. 5.1. It is emphasized that the nominal maximum axial force is equal to 1000 kg. By measuring with a load cell the axial force generated by the tailstock during the movement against the spindle, a

maximum value of 1750 kg was reached. In agreement with the manufacturer of the machine, to prevent damage to the lathe, it was decided to set the nominal value of 1000 kg as a limit and use process parameters that would allow a degree of safety equal to 2 for this value. For this reason, process parameters that from the numerical simulations were correlated with axial loads exceeding 500 kg, which correspond to around 4900 N, were excluded from the experimental tests.

Tab. 5.1 *- Mori Seiki™ NL1500 CNC lathe datasheet.*

Item	Value
Max. turning diameter	366 mm
Max. turning length	1298 mm
Max. spindle speed	6000 rpm
Max. tailstock translational velocity	30 m/min
Max. tailstock force	1000 kg
Max. longitudinal travel	590 mm

The following paragraphs describe the design of the setups used in the case of backward tube flowforming and constrained backward tube flowforming and the experimental procedure adopted.

5.2 Backward Tube Flowforming

The following section describes the experimental setup for carrying out backward tube flowforming operations in detail, reporting the CAD models and the main reasons for the design operations. The exploded-view is reported in the Appendix with the list of components that compose the setup of the backward tube flowforming.

5.2.1 Design of the equipment

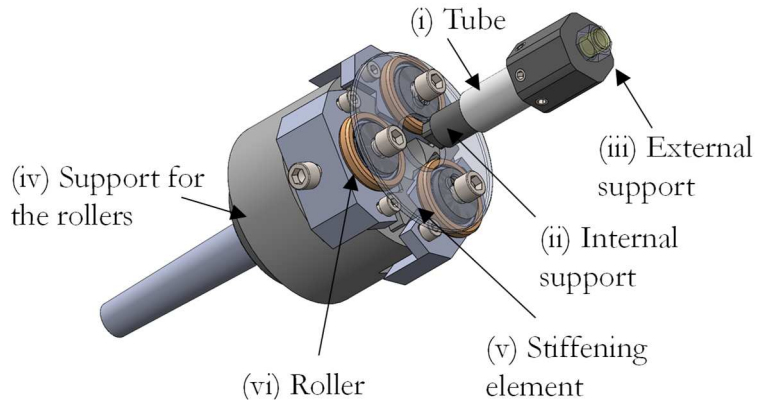

Fig. 5.2 *- Assembly for the traditional backward tube flowforming.*

The assembly of the equipment is shown in Fig. 5.2. It can be seen that the setup is divided into two parts. The first one is a rotating part connected to the spindle of

the lathe, comprising (i) the tube, (ii) the internal support to avoid the collapse of the tube, (iii) the external support for the connection between the workpiece and the machine. The second part is a translating part, connected to the tailstock of the lathe, including (iv) the support for the rollers and (v) stiffening elements to reduce system deflections due to radial forces, (vi) the rollers, and the axial bearings.

The following paragraphs show the details and the design reasons for the main components, in particular as regards the translating part consisting of a support for the rollers, rollers and axial bearings.

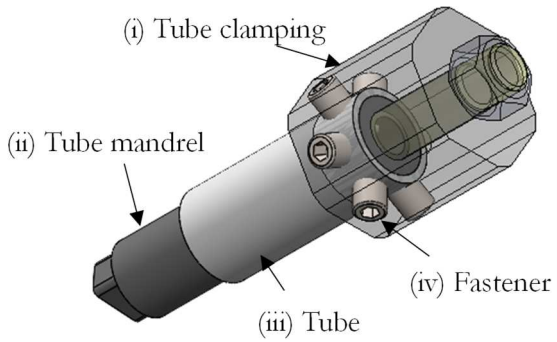

Fig. 5.3 *- Rotational part: (i) tube clamping; (ii) tube mandrel; (iii) tube.*

The rotational part is shown in Fig. 5.3. It is composed of (i) the tube clamping (the external support), which ensures that the nominal rotational speed set is equal to that of the tube, and (ii) the tube mandrel (the internal support), which avoids the collapse of the tube during the process due to the presence of radial forces. The connection of the pieces must guarantee a proper removal of the tube, and to guarantee this for the connection with the tube clamping, two measures have been adopted, in particular a slight interference between the external diameter of the tube and the internal diameter of the tube clamping and six radial fasteners. With the tube mandrel, a connection with interference is not possible. To ensure the integral rotation of the bodies, it was decided to connect the tube clamping and the tube mandrel using a threaded coupling.

The translational part is shown in Fig. 5.4. It is composed of the (i) roller shafts, which constitute the seat of the axial bearings and allow the rotation of the rollers, (ii) three rollers, which have been designed according to the geometric parameters obtained with numerical simulations reported in Chapter 4, and (iii) three axial bearings, which allow absorbing the axial loads generated during the process. The three rollers have a fixed axial offset equal to 1.5 mm, by the optimizations of Chapter 4, while the radial position of the rollers is kept variable, allowing for varying for each pass the tube thickness reduction. To ensure accurate adjustment of the radial distance of the rollers, calibrated steel pieces with a thickness of 0.05 mm were used. In this way, it is possible to perform several passes on the same tube using the same roller shaft elements. A (iv) customized Morse taper shank allows connecting with the lathe's

tailstock, while a (v) circular plate placed at the opposite end allows increasing the structure's stiffness, constraining the rollers' position and reducing the vibrations induced during the process.

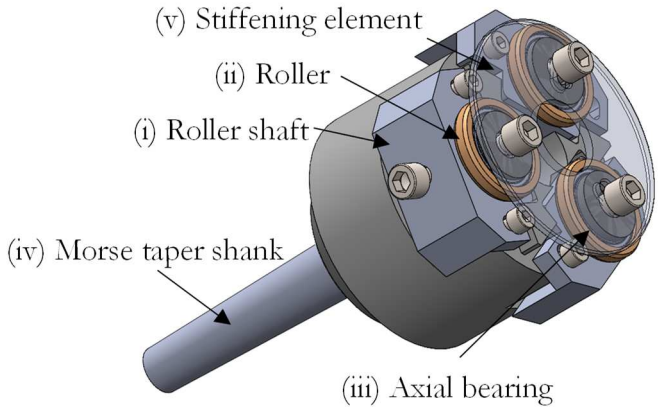

Fig. 5.4 *- Translational part: (i) Roller shafts; (ii) Rollers; (iii) Axial bearings; (iv) Customized Morse taper shank; (v) Stiffening element.*

The technical datasheet of the SKF61807-2RZ axial bearing is reported in Fig. 5.5. In particular, the maximum static load is equal to 3350 N, guaranteeing the rotation of the rollers during the process.

Item	Value
Inner diameter	35 mm
External diameter	47 mm
Thickness	7 mm
Max. velocity	15000 rpm
Max. static load	3350 N
Max. dynamic load	4360 N

Fig. 5.5 *- Axial bearing SKF61807-2RZ.*

5.2.2 Experimental tests

Several experimental tests were carried out using the backward tube flowforming setup, varying the kinematics parameters and the tube thickness reduction. The following tables resume the trials performed, justifying the reasons. To analyse the influence of the kinematic parameters, the tests reported in Tab. 5.2 and Tab. 5.3 were performed. In particular, multiple passes were used for a total tube thickness reduction equal to 42% compared to the initial thickness to investigate the grain refinement

saturation and the increase in mechanical properties. In the first case, a constant feed rate equal to 2 mm/s was used varying the rotational speed with the aim of analyse the mandrel angular velocity influence, while in the second case, a fixed rotational speed equal to 420 rpm was used, to evaluate the roller feed rate influence. Repeatability of three was adopted during the tests, to take into account the variability of the process.

Tab. 5.2 *- Mandrel angular velocity influence.*

#	f (mm/s)	ω (rpm)	$t_{\%}$ (-)
1	2	240	6%
2	2	240	12%
3	2	240	18%
4	2	240	24%
5	2	240	30%
6	2	240	36%
7	2	240	42%
8	2	420	6%
9	2	420	12%
10	2	420	18%
11	2	420	24%
12	2	420	30%
13	2	420	36%
14	2	420	42%
15	2	600	6%
16	2	600	12%
17	2	600	18%
18	2	600	24%
19	2	600	30%
20	2	600	36%
21	2	600	42%

Tab. 5.3 *- Roller feed rate influence.*

#	f (mm/s)	ω (rpm)	$t_{\%}$ (-)
1	1	420	6%
2	1	420	12%
3	1	420	18%
4	1	420	24%
5	1	420	30%
6	1	420	36%
7	1	420	42%
8	1.5	420	6%
9	1.5	420	12%
10	1.5	420	18%
11	1.5	420	24%

12	1.5	420	30%
13	1.5	420	36%
14	1.5	420	42%
15	2	420	6%
16	2	420	12%
17	2	420	18%
18	2	420	24%
19	2	420	30%
20	2	420	36%
21	2	420	42%

5.3 Constrained Backward Tube Flowforming

The following section describes the experimental setup for carrying out the constrained backward tube flowforming operation in detail, reporting the CAD models and the main reasons for the design operations. The exploded-view is reported in the Appendix with the list of components that compose the setup of the constrained backward tube flowforming.

5.3.1 Design of the equipment

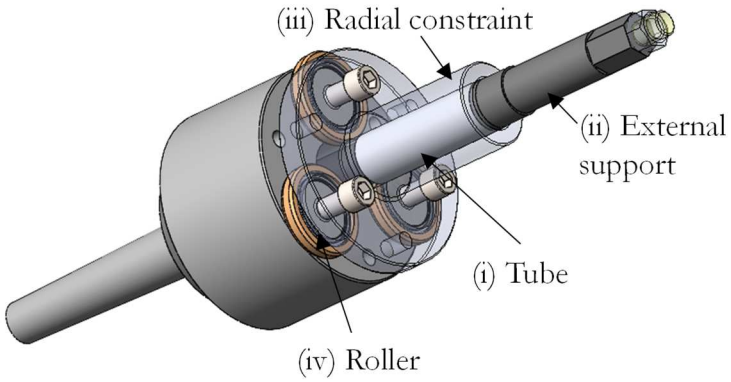

Fig. 5.6 *- Assembly for the constrained backward tube flowforming.*

The assembly of the constrained equipment is shown in Fig. 5.6. As for the traditional backward tube flowforming, also in this solution, the setup is divided into two parts. The first one is a rotating part connected to the spindle of the lathe, comprising (i) the tube, the internal support to avoid the collapse of the tube, and (ii) the external support for the connection between the workpiece and the machine. The second one is a translating part, connected to the lathe's tailstock, in which the (iii) radial constraint for the tube also has a function of improving the setup stiffness, reducing system deflections due to radial forces. In addition to the radial constraint, (iv) the rollers and the axial bearings compose the translating part. The following paragraphs show the details and the design reasons for the main components, in

particular as regards the translating part.

The rotational part is shown in Fig. 5.7. It is composed of (i) the tube clamping, which ensures that the nominal rotational speed set is equal to the one of the tube, and (ii) the tube mandrel, which avoids the collapse of the tube during the process due to the presence of radial forces. The differences between this solution and the solution reported in Fig. 5.3 are that there are no fastener elements, and there is no possibility to vary the thickness reduction due to the internal diameter of the radial constraint. In fact, after each pass, there is a difference between the internal diameter of the radial constraint and the external tube diameter due to the thickness reduction. Two setups are made to solve this technical problem, changing the roller shafts' position and the radial constraint's internal diameter. With this solution, it is possible to perform a unique pass on the tube, however increasing the stiffness of the equipment. A slight interference between the external diameter of the tube mandrel and the internal diameter of the tube was adopted, while it was decided to connect the tube clamping and the tube mandrel through a threaded coupling.

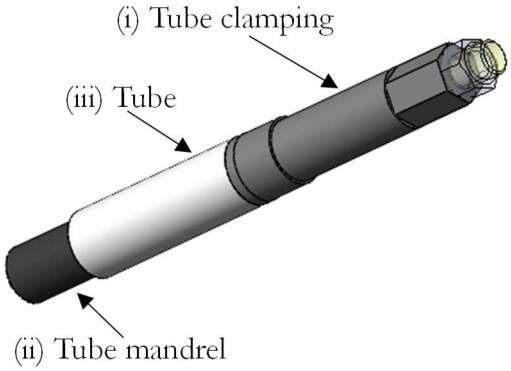

Fig. 5.7 *- Rotational part: (i) tube clamping; (ii) tube mandrel; (iii) tube.*

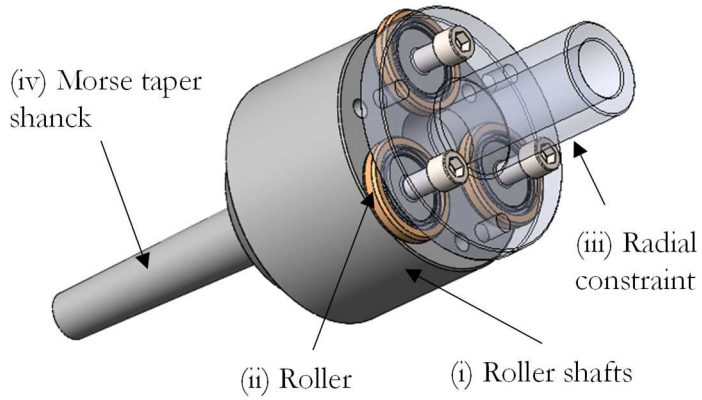

Fig. 5.8 *- Translational part: (i) Roller shafts; (ii) Rollers; (iii) Radial constraint; (iv) Morse taper shank.*

The translational part is shown in Fig. 5.8. It is composed of (i) roller shafts, (ii) three rollers, three axial bearings, and (iii) the radial constraint. The three rollers have a fixed axial offset equal to 1.5 mm and impose a thickness reduction equal to 0.20

mm for the first roller, 0.40 mm for the second roller, and 0.60 mm for the third roller. To carry out experiments with different thickness reductions, two (i) roller shafts configurations were used, having a first pass with a thickness reduction equal to 24% and a second pass with a total reduction of 48%. A (iv) customized Morse taper shank allows connecting with the lathe's tailstock, while the radial constraint, placed at the opposite end, allows increasing the strain imposed by the process, reducing the surface defects, and increasing the hydrostatic pressure imposed on the workpiece. This part must ensure sliding in the tube; therefore, the internal surface of the radial constraint must be free to slide on the external surface of the tube.

5.3.2 Experimental tests

Several experimental tests were carried out using the constrained backward tube flowforming setup, varying the kinematics parameters and the thickness reduction. The following tables resume the trials performed, justifying the reasons. To analyse the influence of the kinematic parameters, the tests reported in Tab. 5.4 and Tab. 5.5 were performed. In particular, due to the equipment characteristics, two passes were performed for a thickness reduction equal to 48% compared to the initial thickness. In the first case, a constant feed rate equal to 1.5 mm/s was used, varying the mandrel rotational speed, to analyse the mandrel angular velocity influence, while in the second case, a rotational speed equal to 420 rpm was used, with different feed rate values, to evaluate the roller feed rate influence. Repeatability of three was adopted during the tests, to take into account the variability of the process.

Tab. 5.4 *- Mandrel angular velocity influence.*

#	f (mm/s)	ω (rpm)	$t_{\%}$ (-)
1	1.5	240	24%
2	1.5	240	48%
3	1.5	420	24%
4	1.5	420	48%
5	1.5	600	24%
6	1.5	600	48%

Tab. 5.5 *- Roller feed rate influence.*

#	f (mm/s)	ω (rpm)	$t_{\%}$ (-)
1	1	420	24%
2	1	420	48%
3	1.5	420	24%
4	1.5	420	48%
5	2	420	24%
6	2	420	48%

Chapter 6

Characterization after flowforming

In this Chapter, the design and the study of the experimental tests for the characterization of the material after the flowforming process are described. In addition, in part related to the characterization through microstructures, a study carried out on the microstructural analysis of grains with high distortion levels is reported.

6.1 Microhardness analysis

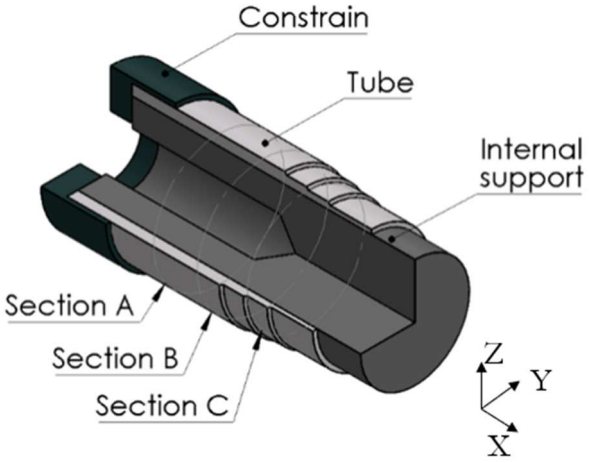

Fig. 6.1 *- Microhardness and microstructure test positions.*

A Leitz™ *Durimet 2* durometer microhardness tester was used to evaluate the

Vickers microhardness (HV) of the material after the flowforming processes, carrying out the indentations using a 2.942 N load and 15 seconds of dwell time. The cold embedded samples were prepared for microhardness analysis using SiC papers for grinding and colloidal silica for the final polishing. The indentations were made in 3 different positions considering the YZ plane, equally spaced by 45 degrees, considering Sections *A*, *B*, and *C* as reported in Fig. 6.2. The indentations were made for each of the three positions as the radius varied, starting from the innermost to the outermost radius. 9 indentations were carried out for each direction, 27 for each section and 81 for each flowformed tube. Considering the XZ plane, in correspondence with Sections *A*, *B*, and *C*, other microhardness tests were carried out, considering indentations as the radius varies, as in the previous case. The microhardness was evaluated in the direction parallel to the advancement of the rollers. In this case, 54 microhardnesses were evaluated for each tube, 18 for each section.

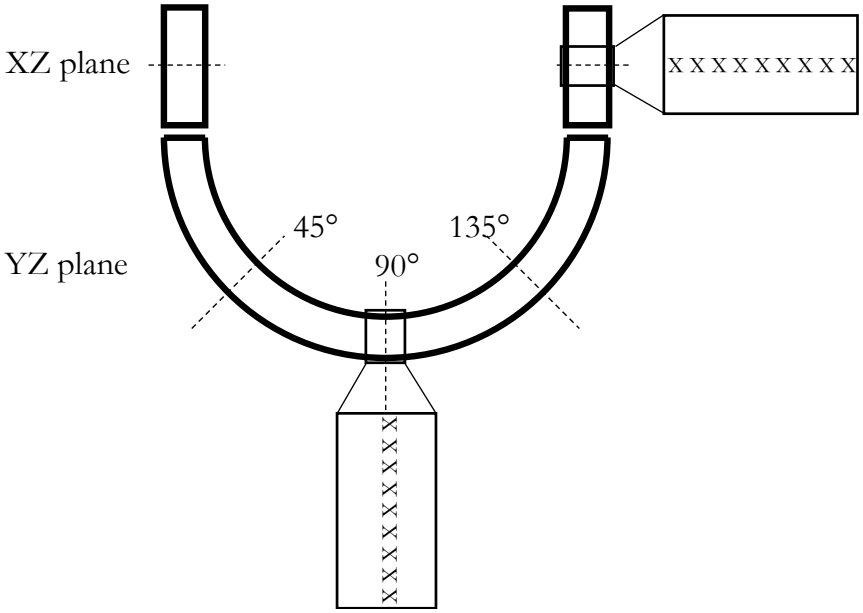

Fig. 6.2 *- Indentation positions for YZ and XZ planes.*

6.2 Microstructure analysis

As regards the analysis of the microstructures, the material, after being cold embedded, was prepared using SiC papers for grinding and colloidal silica for the final polishing. For the chemical etching the Weck's reagent, a solution of 4 g $KMnO_4$ + 1 g NaOH + 100 ml H_2O, for 12 seconds was used, considering the YZ and XZ planes for the grain size evaluation. A FEI Quanta™ *400* Scanning Electron Microscopy (SEM) was used to analyse the grain size evolution after the flowforming processes. As for the microhardness analyses, various areas of interest were considered in the analysis of the microstructure: in the YZ plane, three sections, respectively located at 10 mm, 20 mm, and 30 mm from the undeformed area, while for the XZ plane, in

correspondence of the same three sections, the variation in grain size was evaluated by varying the radius, as reported in Fig. 6.3.

The grain size governs the main physical, chemical, and mechanical properties of the material that it has at room temperature, which depends fundamentally on the process chain used to manufacture the components. The flowforming process permits obtaining a deformation mechanism that allows having a refinement of the material grain, with a considerable elongation in the same direction of the feed of the rollers and a consequent constriction in the direction perpendicular to it. For this reason, the process is considered highly directional, with a significant anisotropy in the shape and size of the grain. There are not only differences in the size of the grain, considering different directions, but there are grains of different shapes depending on whether the external or internal portion of the component is considered, with a grain that moving towards the inside becomes more and more circular.

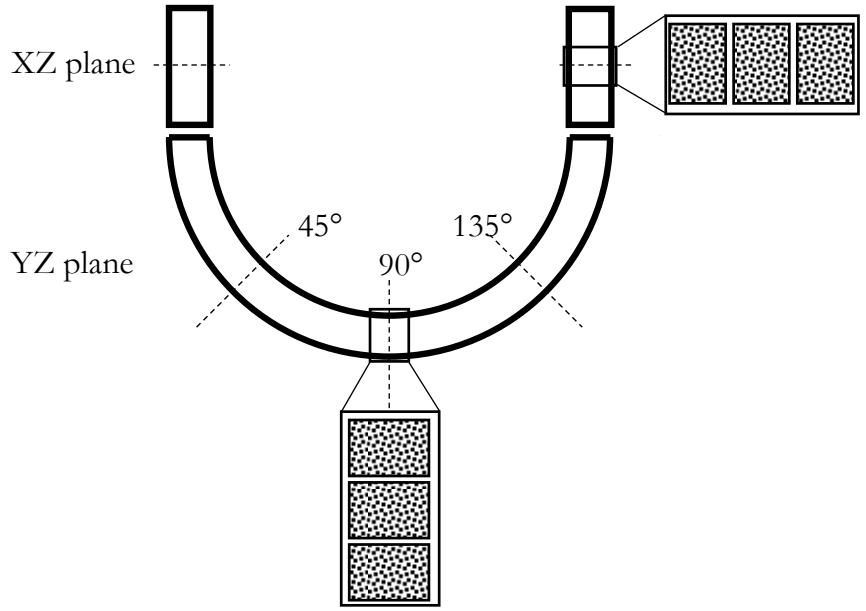

Fig. 6.3 *- Micrograph positions for YZ and XZ planes.*

The high non-uniformity of the microstructure along the radial direction may reach extreme values in the case of high deformation. This aspect may introduce significant uncertainties in evaluating the mechanical properties of the final parts (i.e. microhardness, maximum elongation, yield strength) due to the computational methodologies used to estimate the average grain size. In the literature, there are no contributions regarding the evaluation of the grain size in the case of the flowforming process. The next paragraphs almost verbatim report a study [120] conducted to evaluate these types of microstructures, adapting some parts to the different purposes of the work and not reporting parts that have already been extensively discussed in the previous chapters. This study aimed to choose the appropriate analysis method for very elongated microstructures in one direction.

6.2.1 *State of the art*

Grain size evaluations are probably the most important microstructural measurements performed for either quality control or research purposes. A material grain is a three-dimensional feature, but, in most cases, it is viewed as a two-dimensional feature, measured by different methods after a chemical etching. This is why most measurements are of a planar rather than a spatial nature, and numerous approaches have been developed to reverse planar data into a spatial estimation of grain size [121] - [122]. The study that was carried out focuses on the most frequently used measurement methods to assess the measurement accuracy, having as a reference case for the investigations the flowforming of AA6082-T4 tubes, processed at different process parameters to change the shape of the grain and the gradient along the radius due to different deformation mechanisms. Comparisons were carried out with regards to methods that allow measuring the grain size using 0D features (Triple-Point Count Method), 1D features (Heyn Intercept Method), and 2D features (Jeffries Planimetric Method), describing these operating procedures and analysing the results obtained by considering the direction parallel and orthogonal to the deformation one.

6.2.2 *Grain size measuring methods*

6.2.2.1 *Triple-Point Count Method - 0D features*

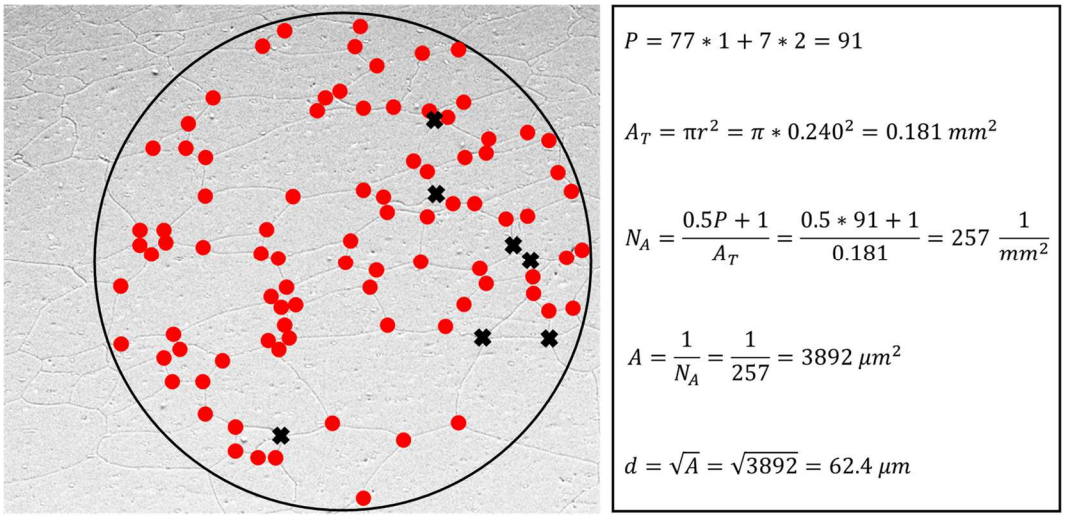

Fig. 6.4 *- Application of the Triple-Point Count Method, using a 500X magnification.*

This method [123] utilizes Euler's law to obtain the number of grains per unit area. The magnification is the only prerequisite because the same micrograph must allow observing at least between 50 and 60 triple points. Having too many triple points leads to a difficult and inaccurate count. To perform this method, a circumference with a known area is superimposed on the micrograph, and the number of triple points, hereafter called *P*, is counted, obtaining the number of grains per unit area, hereafter

N_A, according to the following relationship:

$$N_A = \frac{0{,}5P+1}{A_T} \qquad \textit{Eq. 5}$$

where A_T is the circle test area. A count of two is obtained in the rare case of observation of a four-point grain junction. The reciprocal of N_A allows calculating the average grain area A, while the square root of the area corresponds to the grain diameter d. Fig. 6.4 reports the application of the procedure described above, in which 77 triple-points (dots) and 7 four-junction points (crosses) are counted in a circle having a radius equal to 240 μm, thus resulting in an average grain area of 3892 μm^2 and an average grain diameter d equal to 62.4 μm.

6.2.2.2 Heyn Intercept Method - 1D features

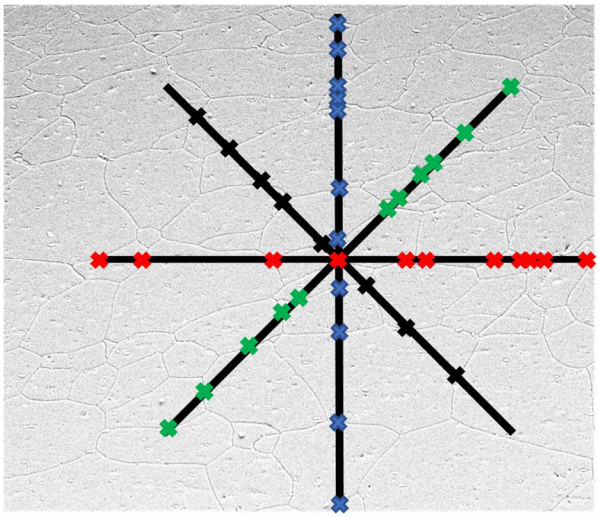

$L_{0°} = 0.480\ mm$ $N_{0°} = 12$

$L_{45°} = 0.480\ mm$ $N_{45°} = 8$

$L_{-45°} = 0.480\ mm$ $N_{-45°} = 11$

$L_{90°} = 0.480\ mm$ $N_{90°} = 11$

$L_{tot} = 1.92\ mm$ $N_{tot} = 42$

$$N_L = \frac{N_{tot}}{L_{tot}} = \frac{42}{1.92} = 21.88\ \frac{1}{mm}$$

$$l = \frac{1}{N_L} = \frac{1}{21.88} = 45.7\ \mu m$$

Fig. 6.5 *- Application of the Heyn Intercept Method, using a 500X magnification.*

The Heyn Intercept Method, developed by Heyn [124] and then modified by Hilliard [125] - [126] and Abrams [127], does not require marking off the intercepts or intersections to obtain an accurate count; hence, this method is faster compared with the zero-dimensional features and the two-dimensional features, and the same degree of precision can be obtained in less time. This method is useful for deformed grain structures because it is possible to place over the micrograph several lines with different orientations in the case of no equiaxed grain structures, as represented in Fig. 6.5. Circumferences substitute lines in the case of equiaxed grain structures. To calculate the grain size, a count can be made of either the number of grains intercepted by the test line, N, or the number of grain boundary intersections with the test lines, P, having equivalent results. It may be easier to make N counts using straight test lines, considering the grains partially intercepted by the ends of the lines as a half grain. Otherwise, using circular test grids, there are no doubts regarding the exact values of N or P, because there are no line ends. The number of N or P counts is divided by the

true test line length (or the circumference in the case of the circular grid) to obtain N_L or P_L, which are the reciprocal of the mean linear intercept length L. As explained above, the procedure in the case of elongated structures can give higher values comparing different directions, for instance, the parallel and the perpendicular direction to the deformation axis. For this reason, it can be defined an anisotropy index, hereafter *AI*, which represents the ratio between the lengths in the parallel and the perpendicular directions:

$$AI = \frac{L_{//}}{L_{\perp}} \qquad \textit{Eq. 6}$$

Fig. 6.5 shows the application of the procedure described above, using four directions for the test lines, in which are counted 12 grains in the vertical direction, 11 grains in the horizontal direction, and respectively 8 and 11 grains in the 45 deg and -45 deg directions. Since each line length equals 480 μm, the average grain length *l* is equal to 45.7 μm.

6.2.2.3 Jeffries Planimetric Method - 2D features

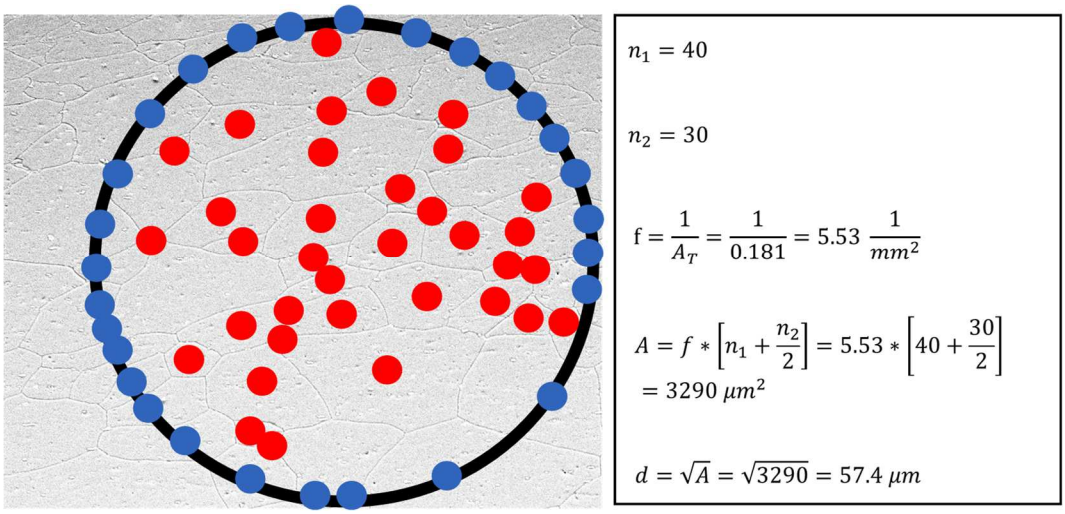

***Fig. 6.6** -Application of the Jeffries Planimetric Method, using a 500X magnification.*

This method, suggested by Sauveur and refined by Jeffries [128], requires counting the number of grains in a known test area, usually circular, superimposed on a micrograph. Also in this case the magnification is a prerequisite to obtaining a correct evaluation of the grain size. Usually, the magnification is chosen so that at least 50 grains are within the test area. Next, the number of grains completely within the test area, hereafter called n_1, and the number of grains intersecting the circle, so-called n_2, are counted. Several fields must be counted to obtain a satisfactory level of precision, depending on the uniformity of the grain structure. The sum of n_1 and $n_2/2$ is multiplied by the Jeffries factor, *f*, which is obtained subdividing the linear magnification squared by the area of the circle, as the following equation:

$$f=\frac{M^2}{A_T} \qquad \textit{Eq. 7}$$

while the number of grains per unit area N_A is obtained according to the following relationship:

$$N_A=f(n_1+\frac{n_2}{2}) \qquad \textit{Eq. 8}$$

moreover, the average grain area A is obtained by the reciprocal of N_A, while the grain diameter d is the square root of the area.

Fig. 6.6 shows the application of the procedure described above, in which are counted 40 grains that are completely inside the circle, while 30 grains intersect the boundary of the circle, in a circle having a radius equal to 240 µm, thus resulting in an average grain area of 3290 µm^2 and an average grain diameter d equal to 57.4 µm.

6.2.3 Application of different methods and conclusions

As explained in the previous section, three different methods were used, comparing the microstructures in two different directions, repeating the test using 5 samples and two different tube thickness reductions. Fig. 6.7 shows the comparison between the various methods reported in Section 6.2.2, with the same micrograph position, material deformation, and analysis direction. The error bar represents the dispersion of the results of the 5 measurements made for each micrograph.

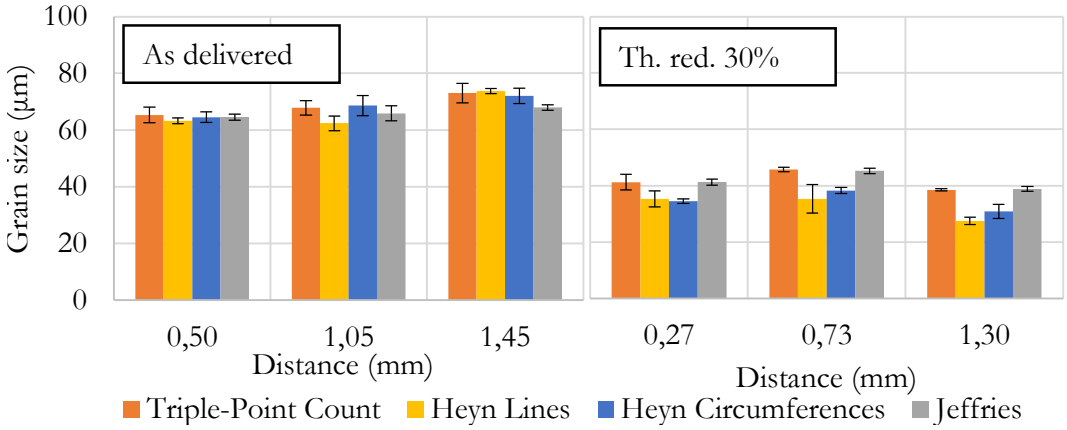

***Fig. 6.7** - Microstructure measurements methods comparison.*

In Fig. 6.7, the various methods are compared by analysing the YZ plane of Section *B*, reported in Fig. 6.1. It is possible to notice how as the grain elongation increases, thus the deformation increases, the differences between the 1D methods (Heyn lines and circumferences) increase compared to the 0D and 2D ones (triple-points count and Jeffries methods), which instead provide compatible results. This difference is related to the nature of the methods: the method developed by Heyn is

particularly suitable in cases where there is a high anisotropy in the grain size, providing the grain size, not deriving it from an area measurement. This means that the fundamental assumption for the 0D and 2D methods is that the grain is equiaxed, deriving its size from mathematical equations. As for the radial direction, also for the axial direction, it is possible to note that as the grain elongation increases, and therefore the deformation, the differences between the 1D methods (lines and Heyn circles) increase compared to the 0D and 2D ones (triple-points count and Jeffries methods), which instead provide compatible results. Furthermore, it can be noted that as the deformation increases, there is less dispersion of the results, which is connected to greater uniformity of the microstructure at the same distance from the centre of the tube. From the analysis of the results, it was possible to observe a notable difference among the various methods: the method developed by Heyn, particularly indicated in cases where there is a high anisotropy of the grains, provided lower measurements values than those obtained with 0D and 2D methods. The reason is due to the mathematical formulation: while in the 0D and 2D cases, the grain measurement is obtained in the hypothesis that it is equiaxed, in the 1D case, it is obtained directly by dividing the number of intersected grains per unit of length. Concluding, 4 directions were chosen on which to carry out the analysis. In this way, it was possible to consider the anisotropy in the shape and size of the grain.

6.3 Tensile test

The tensile tests were carried out using an *MTS™-322* hydraulic dynamometer, with a maximum load of 50 kN and a maximum stroke of 150 mm. From each flowformed tube, 3 tensile specimens were obtained by water cutting. The cutting positions and the dimensions of the specimen are shown in Fig. 6.8. It is possible to notice how the specimens are obtained at 120 degrees from each other and how the gauge length of the specimen is contained in an area having the same thickness. This allows reducing any errors related to section differences.

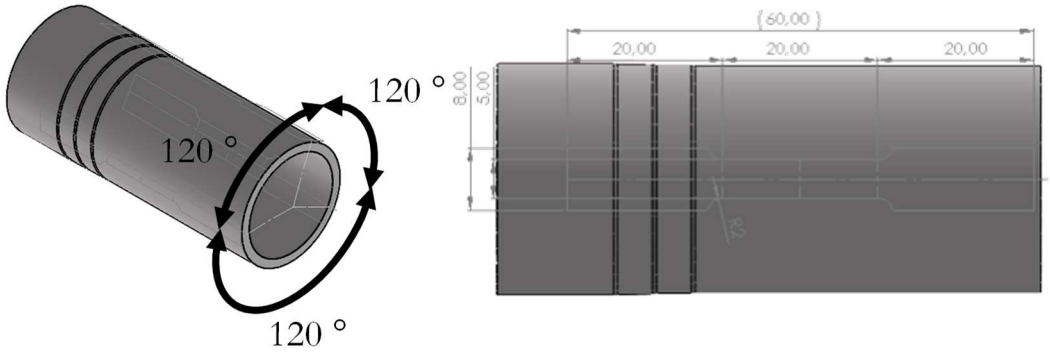

Fig. 6.8 *- Tensile specimen positions and measures.*

6.4 Geometrical analysis

The geometrical tests were carried out using a Coordinate Measuring Machine Zeiss™ *Prismo VAST 7*, equipped with a ball tip probe configuration with a 2.5 mm radius. From each flowformed tube, two geometrical characteristics were evaluated: the thickness and the roundness of the tube considering the Section *A*, *B*, and *C* of the specimen, as reported in Fig. 6.1. For each position, three measures were carried out, varying the position of evaluation of +1 mm and -1 mm, and considering, as a result, the average value obtained from the three measurements. The thickness of the tube was derived from the measure of the inner and the outer diameters. About the roundness, which is the measure of how closely the shape of an object approaches that of a mathematically perfect circle, the outer diameter was considered. A low-pass Gaussian filter was adopted, considering five undulations per revolution.

Part 4: Results and Discussion

Chapter 7
Results

In this Chapter, the numerical and the experimental results of the flowforming tests are reported. In addition, in the part relating to the correlation between numerical and experimental results, the variation of the characteristic parameters of the material (microhardness, grain size, yield stress, tube elongation) was reported as a function of the deformation measured during the numerical simulations. Unless otherwise indicated, the results relating to the configuration at 420 rpm for rotational speed and 2 mm/s for feed rate are reported for the traditional configuration, while the configuration at 420 rpm for rotational speed and 1.5 mm/s for feed rate is reported for the constrained solution. The remaining results are summarized in the Appendix.

7.1 Numerical results

As reported in Sections 4.2.5 and 4.3.5, once the radial position of the rollers was chosen to minimize the axial force necessary to complete the process, the case in which multiple deformation steps are performed on the same tube was numerically analysed, comparing the results obtained with two different setups. This methodology allows to minimize forces and maximize deformations at the same time. In this way, it is possible to reach the same state of deformation that would have been obtained with a much greater interpenetration but with considerably lower forces required. Using a solution with and without a radial constraint allows us to investigate the saturation of mechanical characteristics and grain size reduction.

7.1.1 Strain analysis

Observing the image of the numerical simulation shown in Fig. 7.1, it is possible to notice how the distribution of the strain imposed on the tube is not homogeneous,

both along the radius and along the tube length. As for the traditional setup, also in the constrained process, the strain distribution is radius dependent: after a portion of the initial tube where the parameters are not constant, the deformation reaches approximately constant values. For this reason, it was decided to compare similar positions, to reduce as much as possible an evaluation error linked to the analysis of different deformation states. This radial and longitudinal inhomogeneity can be exploited to have components with different properties, for instance, variable resistance to corrosion, useful in biomedical components.

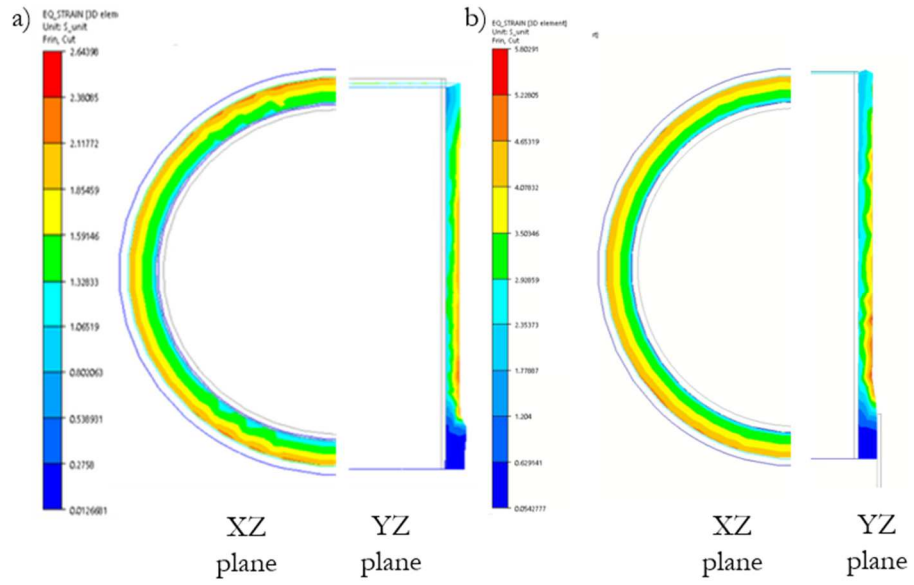

Fig. 7.1 *- Eq. plastic strain distribution in XZ and YZ planes for a) traditional and b) constrained setup.*

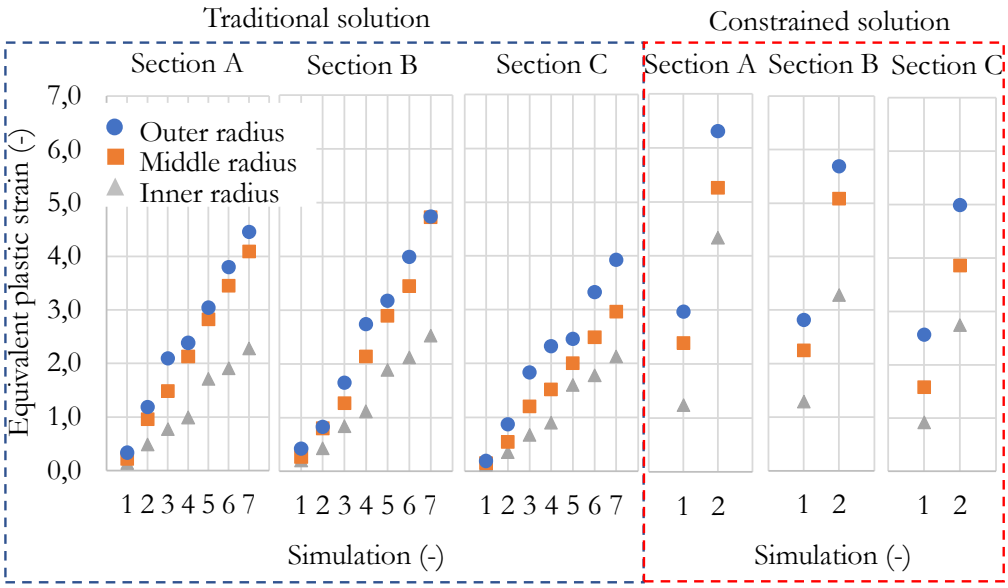

Fig. 7.2 *- Eq. plastic strain for the incremental backward tube flowforming considering the traditional and the constrained setup.*

Fig. 7.2 reports the results of the numerical simulations carried out using the backward tube flowforming process considering the traditional and constrained setup. As explained in the previous Chapters, an incremental process is considered, the details of which and the relative results are reported in Tab. 7.1 and Tab. 7.2. The main remaining results are shown in graphical form in the Appendix.

Tab. 7.1 *- Eq. pl. strain numerical simulation results considering the traditional solution.*

#	$t_{initial}$ (mm)	t_{final} (mm)	Δt (-)	ε_{A-i}	ε_{A-m}	ε_{A-o}	ε_{B-i}	ε_{B-m}	ε_{B-o}	ε_{C-i}	ε_{C-m}	ε_{C-o}
1	2.50	2.35	-6%	0.14	0.21	0.32	0.20	0.27	0.42	0.12	0.15	0.19
2	2.35	2.20	-12%	0.48	0.96	1.18	0.43	0.80	0.83	0.35	0.54	0.87
3	2.20	2.05	-18%	0.77	1.48	2.10	0.84	1.27	1.65	0.67	1.20	1.84
4	2.05	1.90	-24%	0.99	2.13	2.39	1.12	2.14	2.74	0.90	1.52	2.32
5	1.90	1.75	-30%	1.71	2.83	3.04	1.89	2.89	3.18	1.60	2.01	2.46
6	1.75	1.60	-36%	1.91	3.45	3.80	2.12	3.45	3.99	1.78	2.49	3.33
7	1.60	1.45	-42%	2.28	4.09	4.46	2.53	4.73	4.74	2.13	2.96	3.93

Tab. 7.2 *- Eq. pl. strain numerical simulation results considering the constrained solution.*

#	$t_{initial}$ (mm)	t_{final} (mm)	Δt (-)	ε_{A-i}	ε_{A-m}	ε_{A-o}	ε_{B-i}	ε_{B-m}	ε_{B-o}	ε_{C-i}	ε_{C-m}	ε_{C-o}
1	2.50	1.90	-24%	1.24	2.39	2.97	1.29	2.25	2.82	0.92	1.58	2.56
2	1.90	1.30	-48%	4.34	5.26	6.31	3.78	5.08	5.69	2.74	3.86	4.99

The constrained solution allows avoiding the build-up defect (see Fig. 7.3), guaranteeing higher deformation levels compared to the traditional setup both due to the presence of the radial constraint and to the possibility of further reducing the thickness. Comparing the equivalent plastic strain obtained with the traditional setup and with the radial constraint for an equivalent thickness reduction equal to 24%, it is possible to notice how the constrained solution allows reaching higher strain values due to the presence of the radial constraint. The increments, reported in Tab. 7.3, are lower in the initial section due to the lower influence of the radial constraint. The sections further away from the free end of the tube, on the other hand, are subject to a greater increase due to the more effective action of the radial constraint. It is possible to note from the results obtained that as the number of passes increases, and therefore the thickness reduction, the trend of the equivalent plastic strain is approximately linear. However, in the first section that is deformed, called *C*, the deformation values are smaller than those of Section *A* and *B,* considering the outer radius. This means that the process becomes stable after an initial stretch in which the deformation is not yet stable and maximum. The increase in deformation remains almost on a linear trend as the thickness reduction increases.

Fig. 7.3 compares the real shape and the numerical shape of the tube using the constrained solution, demonstrating the consistency of the numerical simulations with

the experimental tests. In addition, it is possible to notice the absence of the build-up defect due to the presence of the radial constraint.

Tab. 7.3 *- Eq. plastic strain numerical simulations comparison.*

setup	$\varepsilon_{A\text{-}i}$	$\varepsilon_{A\text{-}m}$	$\varepsilon_{A\text{-}o}$	$\varepsilon_{B\text{-}i}$	$\varepsilon_{B\text{-}m}$	$\varepsilon_{B\text{-}o}$	$\varepsilon_{C\text{-}i}$	$\varepsilon_{C\text{-}m}$	$\varepsilon_{C\text{-}o}$
trad.	0.99	2.13	2.39	1.12	2.14	2.74	0.90	1.52	2.32
const.	1.24	2.39	2.97	1.29	2.25	2.82	0.92	1.58	2.56
incr.%	+20%	+11%	+20%	+13%	+5%	+3%	+2%	+4%	+9%

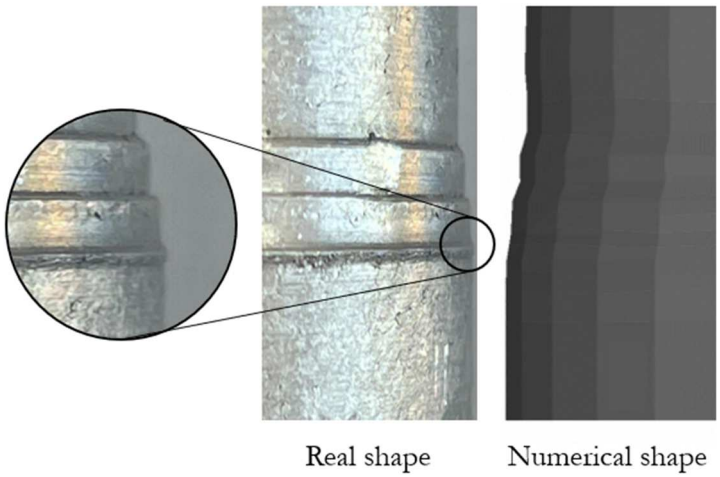

Fig. 7.3 *- Comparison between real and numerical shape.*

By analysing the trend of the equivalent plastic strain during the process, it is possible to notice how the sensor (in the case under examination placed in correspondence with Section *A*, in the outermost radius) is affected by the passage of the three rollers at different instants of time, thus undergoing an incremental deformation. However, after the passage of the last roller, the material, while elongating in the axial direction, undergoes further deformation, reaching the maximum value.

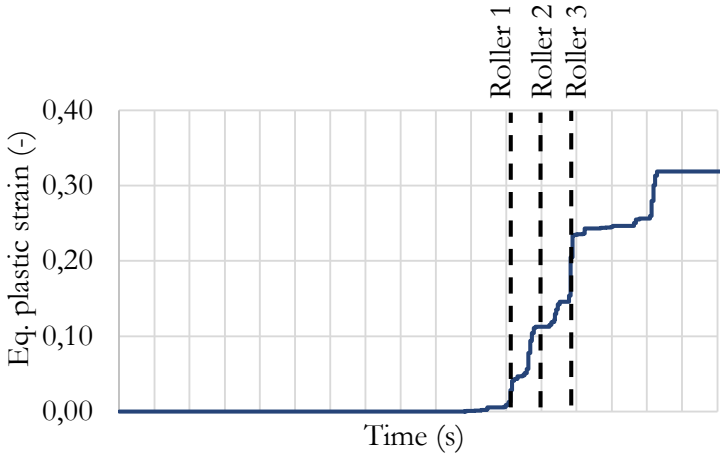

Fig. 7.4 *- Equivalent plastic strain Section A - outer radius for a thickness reduction equal to 6%.*

Fig. 7.5 shows the plot of the strain components vs. the time for an element in the tube cross-section, respectively on the inner, middle, and outer portion of the tube subjected to the traditional backward flowforming process. Section *B* was selected as a reference for the comparison. During the process, the material under the action of the roller encounters a compressive strain condition in the radial direction and a tensile strain condition in the axial and circumferential directions. The results show that the level of the circumferential strain is almost zero in all the layers of the cross-section, and this confirms the assumption of a low value for the friction coefficient between the mandrel and the inner tube surface. On the contrary, the outer layer presents the material build-up in front of the roller, and the outer element experiences first a radial tensile strain and then compressive strain under the roller.

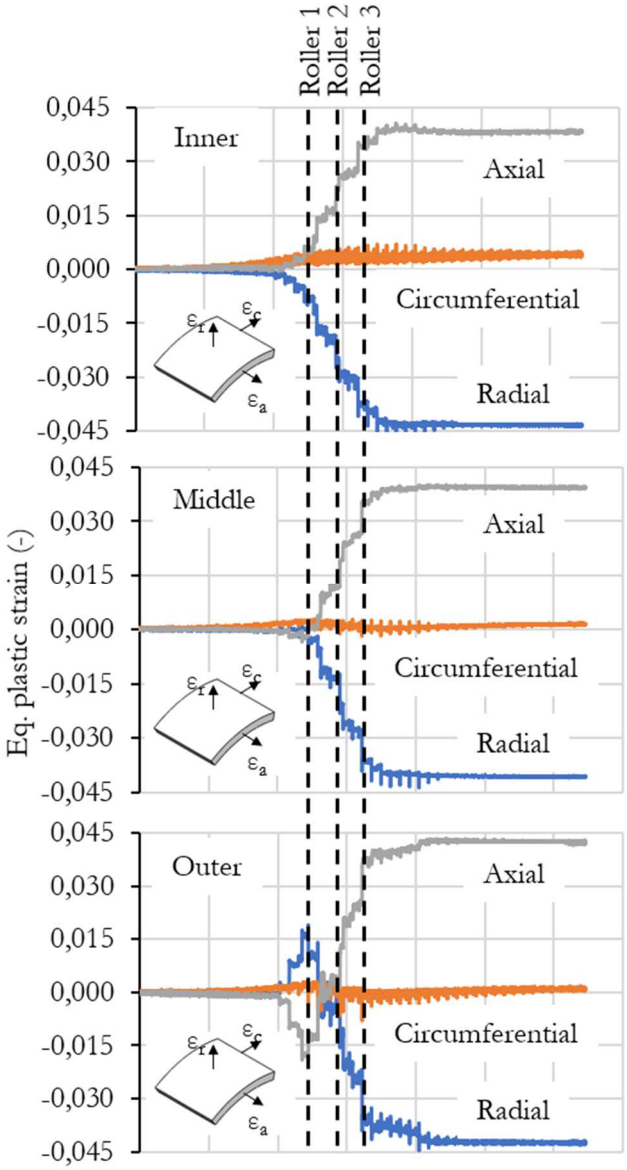

Fig. 7.5 *- Example of strain analysis during the process.*

7.1.2 Tube elongation analysis

The elongation of the tube compared with the initial conditions is another result that has been taken into consideration and can then be related to the experimental results. For this reason, after each pass of the rollers, the length of the tube was evaluated, and the difference compared to the initial value was calculated. Although it can be thought that the tube has a linear elongation as its thickness decreases, being an incremental process with constant thickness variations, it can be seen that the results obtained from the numerical simulations follow a quadratic trend, as shown in Fig. 7.6, with an elongation that tends to decrease as it increases the number of passes and therefore the deformation. Considering the constrained solution and comparing it with the result obtained with the traditional setup, as a function of the reduction in thickness, it is possible to note that there is greater elongation. This difference is the absence of the build-up defect: since the volume of the material is conserved, the tube is not allowed to expand radially, thus constraining it to a greater axial elongation.

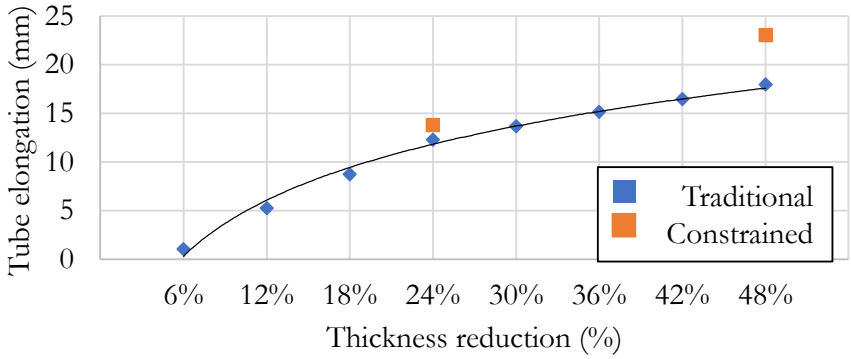

***Fig. 7.6** - Tube elongation vs. thickness reduction.*

7.2 Experimental results

7.2.1 Microhardness analysis

The graphs reported in Fig. 7.7 allow us to compare the microhardness values in the YZ plane and the XZ plane of the samples, after a thickness reduction of 30% using the traditional setup, considering different rotational speeds, equal to a) 240 rpm, b) 420 rpm and c) 600 rpm. The result relating to this reduction in thickness due to the phenomenon of saturation of the mechanical properties explained in the following paragraphs has been reported, while the results regarding the various thickness reductions are reported in the Appendix in terms of percentage increases. In reporting the average values, the tube section was divided into three parts, grouping the results for each part. For example, in Fig. 7.7, the indentations performed on an internal radius (between 12.50 mm and 13.08 mm), average radius (between 13.08 and 13.66 mm), and external radius (between 13.66 and 14.25 mm) have been grouped. The error bars

represent the dispersion of the results for each group, considering the minimum and maximum values as the upper and lower limits.

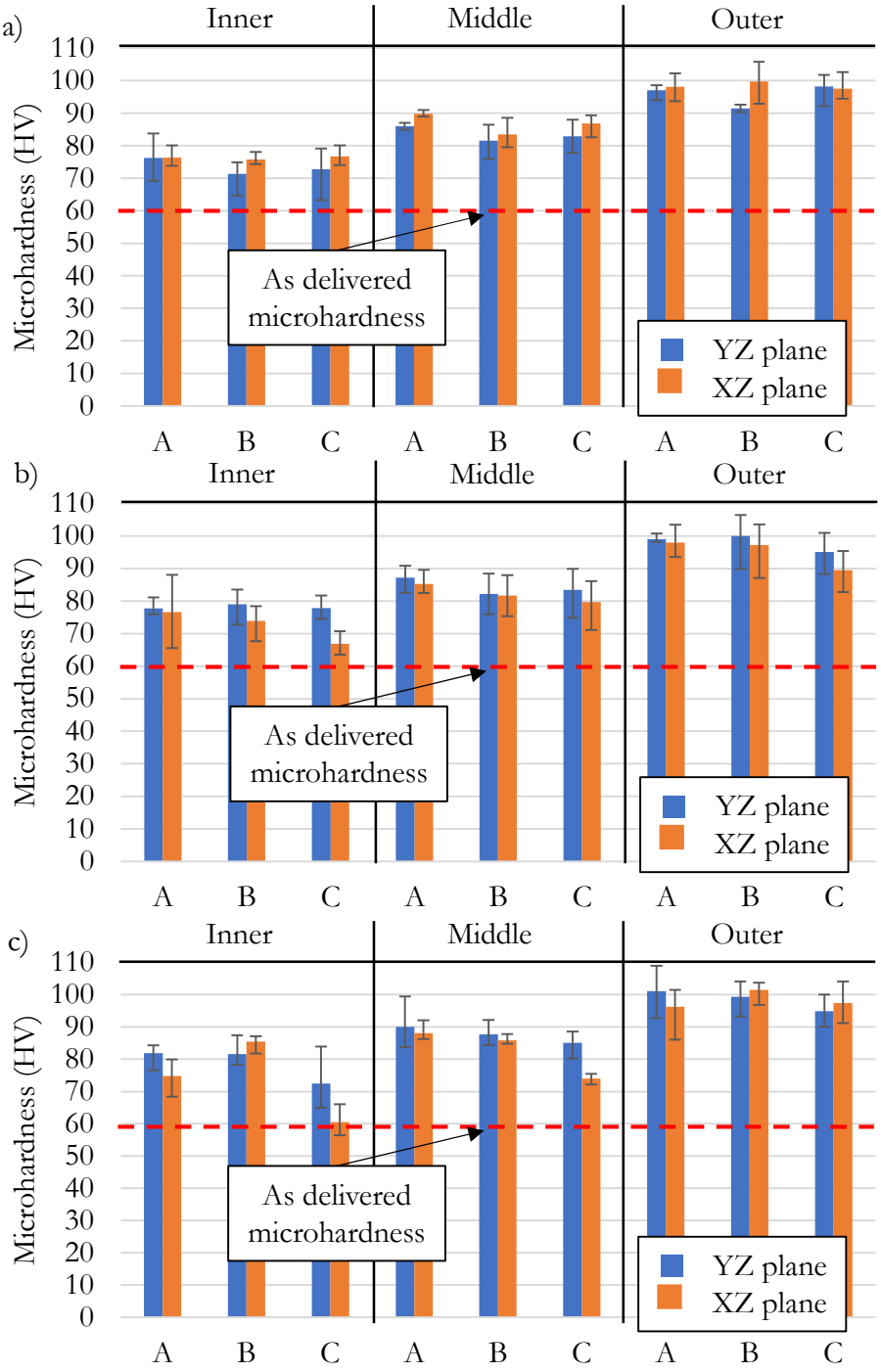

Fig. 7.7 *- Microhardness comparison among different mandrel speeds after a th. reduction equal to 30% for sections: A - 10 mm, B - 20 mm, C - 30 mm, considering a) 240 rpm, b) 420 rpm, c) 600 rpm.*

It is possible to observe an increase in the microhardness values between the internal and external portion of the specimens for each cross-section, but even by

varying the rotation speed, consistent results are obtained. However, in carrying out the tests, it was seen that as the rotation speed increases, the setup becomes more unstable, generating harmful vibrations for the mechanical parts, which in turn caused a lower surface quality. Comparing the results obtained considering the YZ plane and the XZ plane are founded similar microhardness values in all three layers. In particular, it is possible to notice an increase concerning the as-delivered conditions in all three layers considered. Following the results of the numerical simulations, increasing the distance from the centre of the tube, higher microhardness values are in correspondence with the outer layer. Considering different sections of the tube, it is possible to note, following what was found in the numerical simulations, that the process becomes stable after an initial transient, allowing to reach, in addition to higher deformation values, also higher microhardness values. Considering a thickness reduction equal to 30%, the variations of the microhardness values are reported in Tab. 7.4. The average is between +23% and +25% considering the internal radius of the tube, +37% and +40% considering the middle radius, and between +58% and +62% considering the outer portion. Considering the entire tube, the microhardness increases from 60.9±1.5 HV to an average value of 85.7 HV, equivalent to +41%. The error related to the average microhardness comprehends the dispersion of the results, from the minimum to the maximum value. However, in correspondence with a deformation obtained with a thickness reduction of between 30% and 36%, increases in mechanical properties are no longer noted. For this reason, a more advanced analysis was performed to evaluate the microhardness along the radius as the thickness reduction varies.

Tab. 7.4 *- Microhardness considering different rotational speeds.*

ω (rpm)	Inner	Middle	Outer	$Av._{rot\ speed}$
240	+23%	+40%	+59%	+41%
420	+24%	+37%	+58%	+40%
600	+25%	+40%	+62%	+42%
$Av._{layer}$	+24%	+39%	+60%	**+41%**

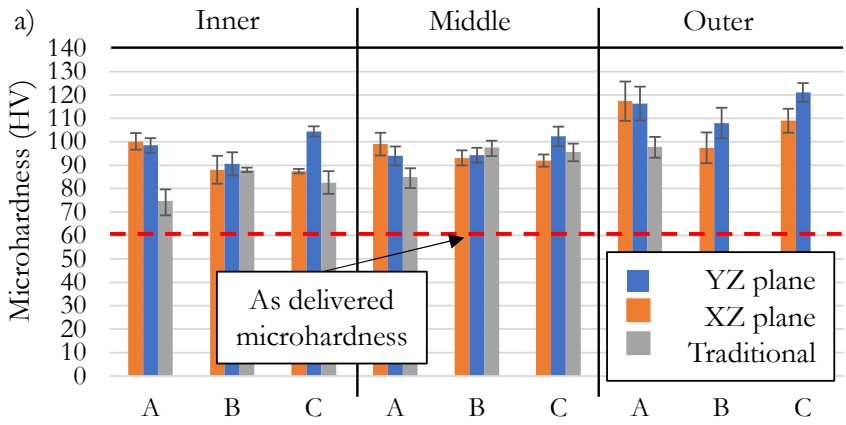

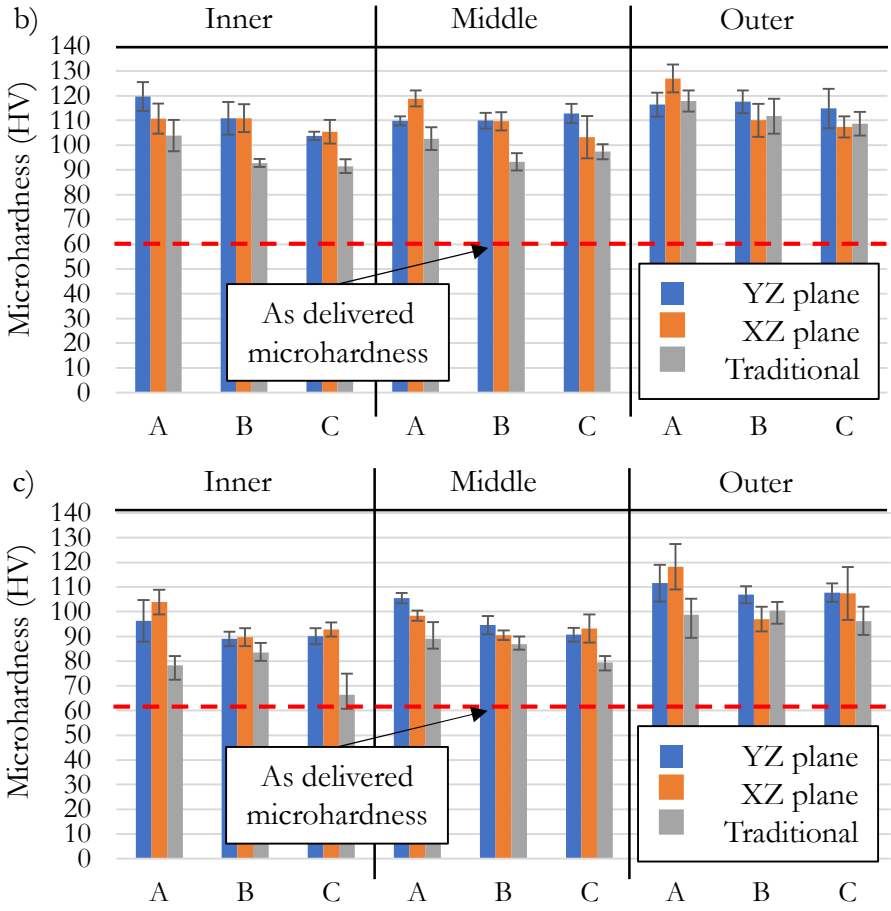

Fig. 7.8 *- Microhardness comparison among different mandrel speeds after a th. reduction equal to 24% for sections: A - 10 mm, B - 20 mm, C - 30 mm, considering a) 240 rpm, b) 420 rpm, c) 600 rpm.*

The graphs reported in Fig. 7.8 allow us to compare the microhardness values in the YZ plane and the XZ plane of the samples, after a thickness reduction of 24% using the constrained setup, considering different rotational speeds, equal to a) 240 rpm, b) 420 rpm and c) 600 rpm. These values have been reported here because they are comparable with those obtained with the traditional setup with the same thickness reduction (grey column). For simplicity, the average value between the value of the XY and YZ plane has been reported. It is possible to observe an increase in the microhardness values between the internal and external portion of the specimens for each cross-section, but even by varying the rotation speed, consistent results are obtained. Unlike the traditional case, in carrying out the tests, it was seen that as the rotation speed increases, the setup remains stable, damping harmful vibrations for the mechanical parts due to the stiffener setup. Furthermore, even at lower speeds, a higher surface quality was noted, with a lower roughness. Comparing the results obtained considering the YZ plane and the XZ plane are founded similar microhardness values in all three layers. In particular, it is possible to notice an increase concerning the as-delivered conditions in all three layers considered. Following the

results of the numerical simulations, increasing the distance from the centre of the tube, higher microhardness values are in correspondence with the outer layer. Considering a thickness reduction equal to 24%, the variations of the microhardness values are reported in Tab. 7.5. The average is between +56% and +60% considering the internal radius of the tube, +59% and +63% considering the middle radius, and between +80% and +89% considering the outer portion. Considering the entire tube, the microhardness increases from 60.9±1.5 HV to an average value of 102.3 HV, equivalent to +68%. The error related to the average microhardness comprehends the dispersion of the results, from the minimum to the maximum value. The greatest increase in microhardness is due to two factors: firstly, the presence of the radial constraint, which increases the deformation impressed on the tube; secondly, the presence of fixed roller shafts. This solution considerably increases the stiffness of the structure, in turn imposing a higher point deformation.

Tab. 7.5 *- Microhardness considering different rotational speeds.*

ω (rpm)	Inner	Middle	Outer	$Av._{rot\ speed}$
240	+58%	+60%	+86%	+68%
420	+60%	+63%	+89%	+71%
600	+56%	+59%	+80%	+65%
$Av._{layer}$	+58%	+61%	+85%	**+68%**

The graphs reported in Fig. 7.9 allow us to compare the microhardness values in the YZ plane and the XZ plane of the samples, after a thickness reduction of 30% using the traditional setup, considering different feed rates, equal to a) 1 mm/s, b) 1,5 mm/s and c) 2 mm/s, and a rotational speed equal to 420 rpm. It is possible to observe that also in this case, for each cross-section, there is an increase in the microhardness values between the internal and external portion of the specimens, and by increasing the feed rate, increased microhardness values are obtained accordingly with the numerical simulation results.

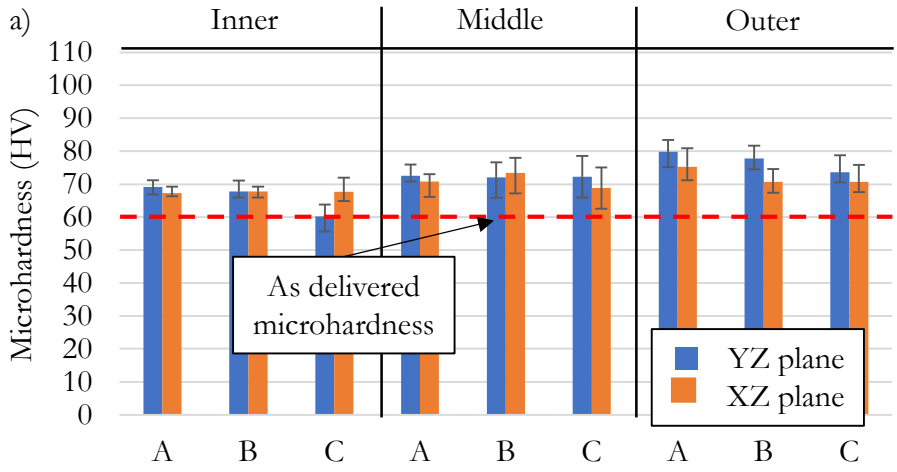

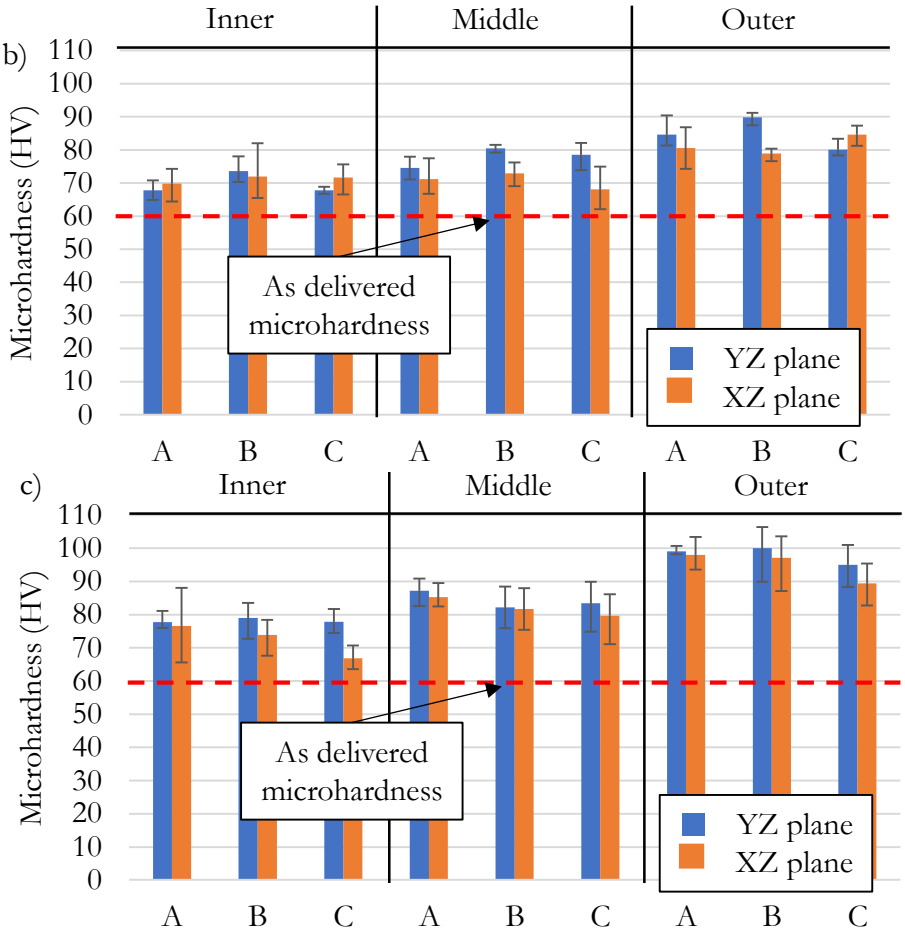

Fig. 7.9 *- Microhardness comparison among different feed rates after a th. reduction equal to 30% for sections: A - 10 mm, B - 20 mm, C - 30 mm, considering a) 1 mm/s, b) 1,5 mm/s, c) 2 mm/s.*

Considering a thickness reduction equal to 30%, the variations of the microhardness values varying the feed rate are reported in Tab. 7.6. The average is between +9% and +24% considering the internal radius of the tube, +18% and +37% considering the middle radius, and between +23% and +58% considering the outer portion. Considering the entire tube, the microhardness increases from 60.9±1.5 HV to an average value of 77.3 HV, equivalent to +27%.

Tab. 7.6 *- Microhardness considering different feed rates.*

***f*(mm/s)**	**Inner**	**Middle**	**Outer**	**Av.$_{\text{feed rate}}$**
1.0	+9%	+18%	+23%	+17%
1.5	+16%	+22%	+36%	+25%
2.0	+24%	+37%	+58%	+40%
Av.$_{\text{layer}}$	+16%	+25%	+39%	**+27%**

The graphs reported in Fig. 7.10 allow us to compare the microhardness values in the YZ plane and the XZ plane of the samples, after a thickness reduction of 24%

using the constrained setup, considering different feed rates, equal to a) 1 mm/s, b) 1,5 mm/s and c) 2 mm/s, and a rotational speed equal to 420 rpm. It is possible to observe that in this case, there is an increase in the microhardness values between the internal and external portions of the specimen for each cross-section.

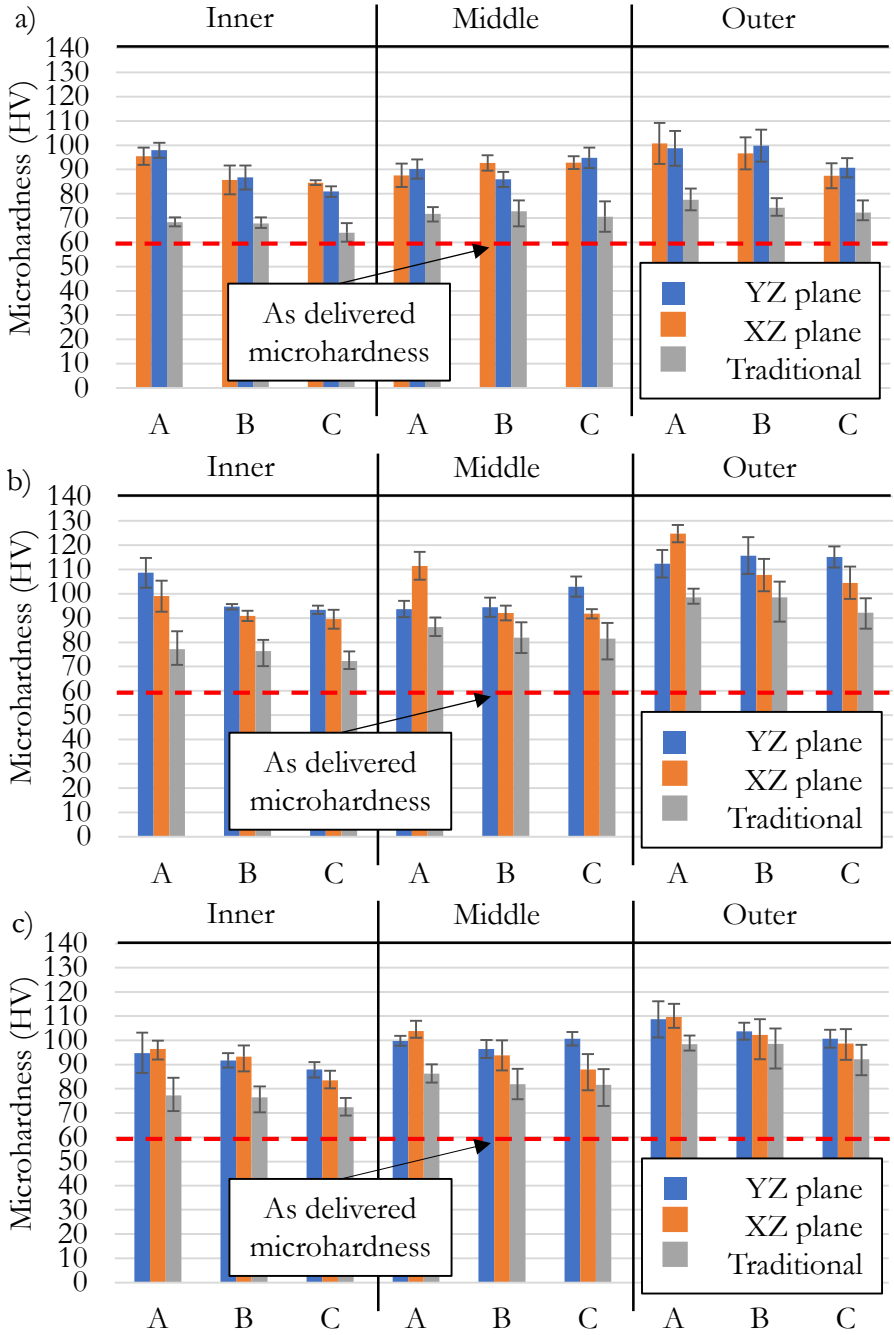

Fig. 7.10 *- Microhardness comparison among different feed rates after a th. reduction equal to 24% for sections: A - 10 mm, B - 20 mm, C - 30 mm, considering a) 1 mm/s, b) 1,5 mm/s, c) 2 mm/s.*

The influence of the feed rate in microhardness variation is not linear: as this kinematic parameter increases, a higher increase is reached for a value of 1.5 mm/s,

but lower results are obtained considering a feed rate of 1 mm/s and 2 mm/s. Considering a thickness reduction equal to 24%, the variations of the microhardness values varying the feed rate are reported in Tab. 7.7. The average is between +48% and +60% considering the internal radius of the tube, +51% and +62% considering the middle radius, and between +59% and +89% considering the outer portion. Considering the entire tube, the microhardness increases from 60.9±1.5 HV to an average value of 98.7 HV, equivalent to +62%.

***Tab. 7.7** - Microhardness considering different feed rates.*

***f*(mm/s)**	**Inner**	**Middle**	**Outer**	**Av.$_{\text{feed rate}}$**
1.0	+48%	+51%	+59%	+53%
1.5	+60%	+63%	+89%	+71%
2.0	+52%	+62%	+73%	+40%
Av.$_{\text{layer}}$	+53%	+59%	+74%	**+62%**

Since the data relating to a 48% reduction in thickness are not available for the traditional setup, the values relating to the increase in microhardness obtained with the constrained process are reported in Tab 7.8 and Tab. 7.9 in terms of average values.

***Tab. 7.8** - Microhardness considering different rotational speeds.*

ω (rpm)	**Inner**	**Middle**	**Outer**	**Av.$_{\text{rot speed}}$**
240	+87%	+79%	+90%	+85%
420	+84%	+84%	+92%	+87%
600	+80%	+78%	+89%	+82%
Av.$_{\text{layer}}$	+84%	+80%	+89%	**+85%**

For each cross-section, there is an increase in the microhardness values between the internal and external portion of the specimens, but even by varying the rotation speed or feed rate, a consistent trend for the 24% thickness reduction is obtained. Unlike the use of the traditional setup, which involved the saturation of the mechanical characteristics already with a thickness reduction of 30%, in this case, there is a further increase considering a thickness reduction of 48%.

***Tab. 7.9** - Microhardness considering different feed rates.*

***f*(mm/s)**	**Inner**	**Middle**	**Outer**	**Av.$_{\text{feed rate}}$**
1.0	+59%	+84%	+90%	+78%
1.5	+84%	+84%	+92%	+87%
2.0	+82%	+84%	+93%	+87%
Av.$_{\text{layer}}$	+75%	+87%	+87%	**+84%**

By comparing two different thickness reductions, it is possible to notice how the microhardness increase in the outer portion of the tube is lower than the inner surface. This shows that the use of this equipment increases the hydrostatic pressure and, by

increasing the deformation imposed in the piece, it increases the mechanical characteristics. Further tests with a greater reduction in thickness are necessary to investigate the limit for which the saturation phenomenon occurs.

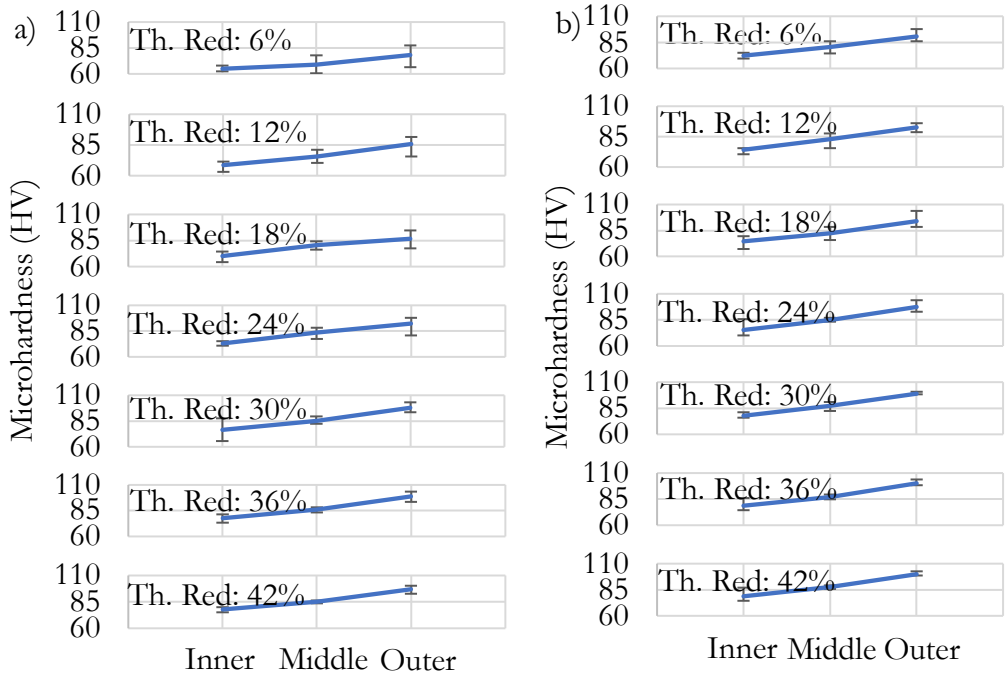

Fig. 7.11 *- Microhardness comparison among different thickness reduction using a mandrel speed equal to 420 rpm in the a) XZ and b) YZ planes considering Section A.*

The graphs of Fig. 7.11 describe the variation in Vickers microhardness as the thickness reduction varies, considering the a) XZ and b) YZ planes and using the traditional setup. This in-deep analysis allows understanding that comparing the microhardness considering different thickness reductions with the as-delivered microhardness (60.9 HV), it is possible to observe an increase in the whole area of the sample. Considering the inner radius, the deformation mechanism causes an increase in the mechanical properties with respect to the delivery condition without any significant changes as the number of passes varies in a zone that is not directly in contact with the rollers. Considering the external part of the tube, it can be seen that there is an increase in the supply conditions both in the YZ and XZ planes, also in this case without significant variations as the number of passes varies. Considering the punctual microhardness values and not the average ones, increasing the thickness reduction makes it possible to gradually obtain higher microhardness values in a larger portion of the tube, as reported in Fig. 7.12 for the Section *A* of the YZ plane. In the graphs, an increase in microhardness of 20% is considered as a marker, and it is possible to notice how the area of the tube in which this increase occurs increases more and more until it involves almost the entire tube with a thickness reduction of 36%. Furthermore, observing the trend line of the values in the graphs, it is possible to observe an initial increase in slope, significant of the fact that there is an increase in

the microhardness of the entire flowformed sample, while, after a certain amount of strain, the slope of the trend line returns to be less pending. This means that even if the deformation increases, there is no longer a variation of the mechanical characteristics intended as maximum values, but the overall properties gradually improve.

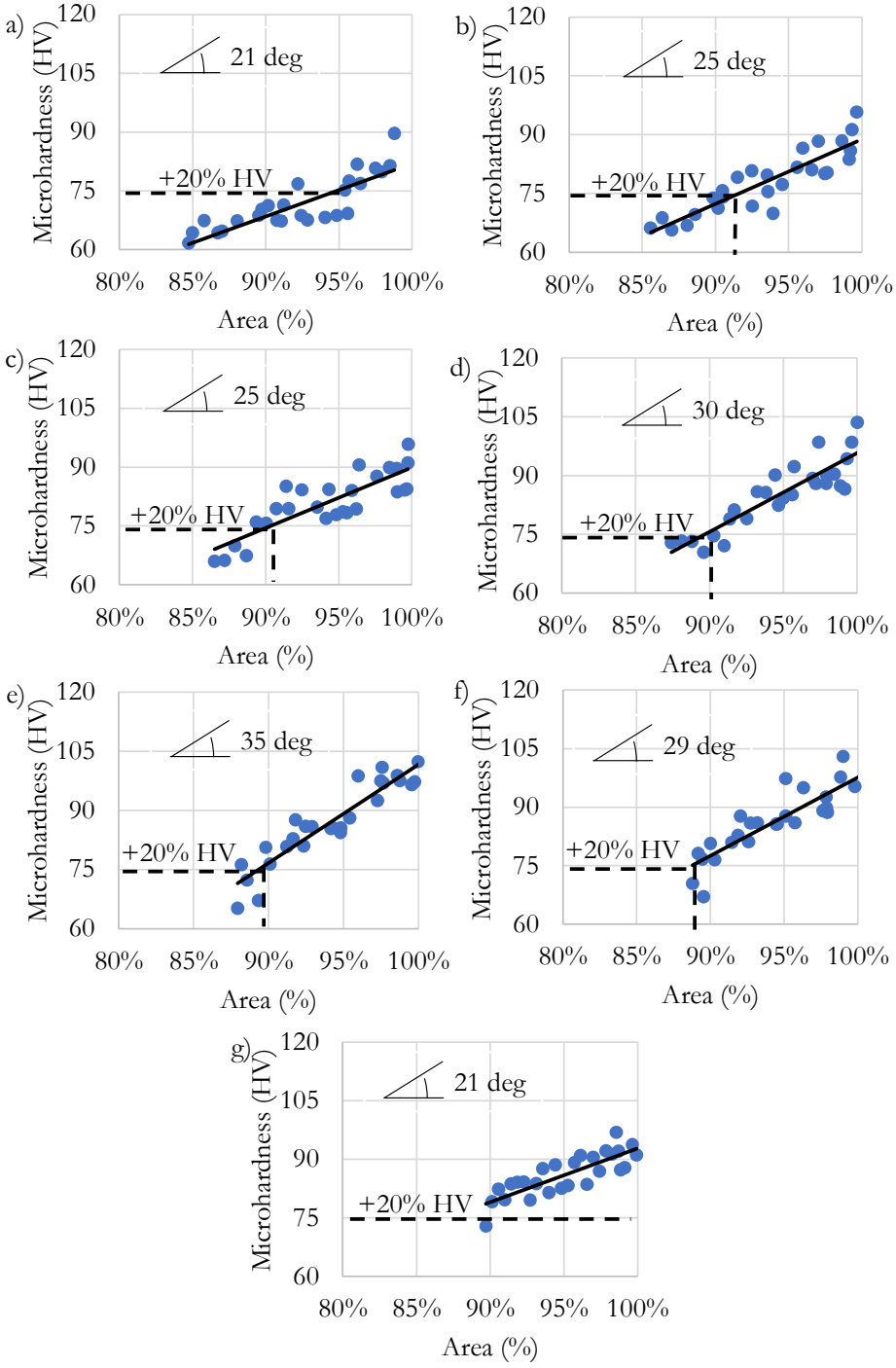

Fig. 7.12 *- Microhardness vs. tube area considering different thickness reduction: a) 6%, b) 12%, c) 18%, d) 24%, e) 30%, f) 36% and g) 42%.*

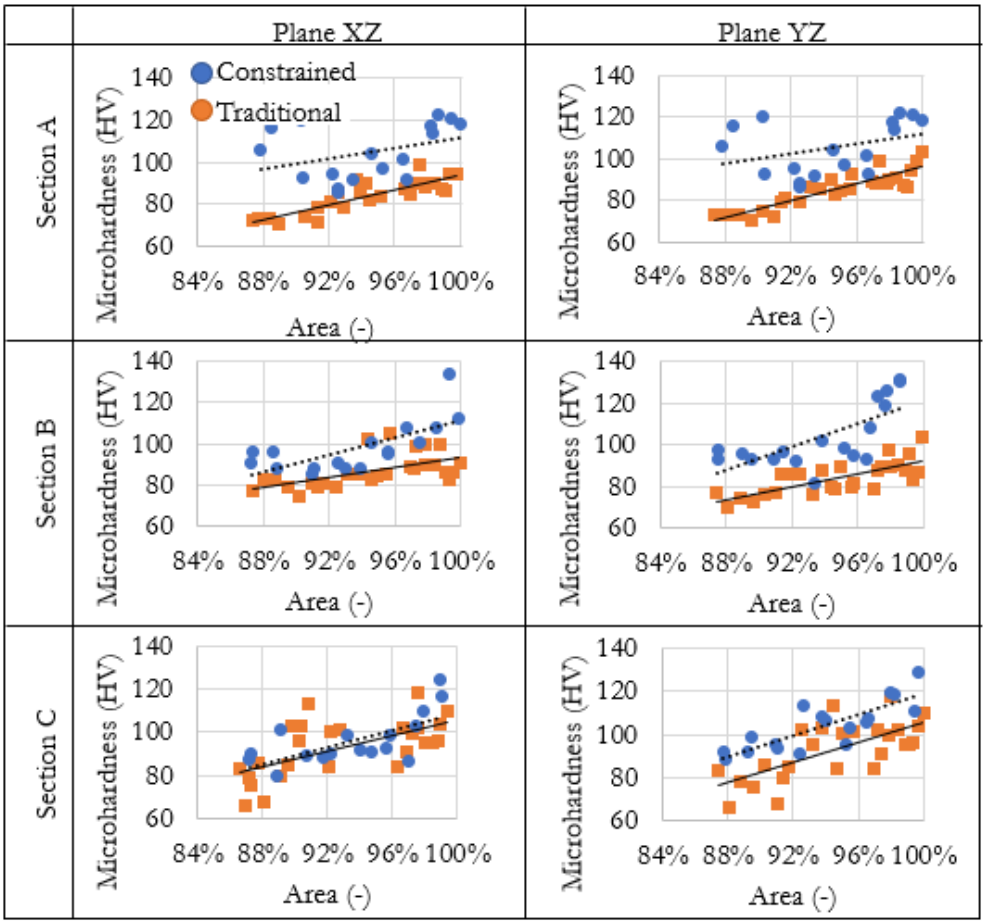

Fig. 7.13 *- Comparison between traditional and constrained setup considering XZ and YZ planes.*

In Fig. 7.13, the microhardness values obtained using the traditional setup and the radially constrained one were compared, showing a gradually greater difference as the distance from the free end of the tube increases. This reasonably means that the first sections deformed by the rollers are not affected by the presence of the radial constraint, while moving the radial constraint axially, following what was found in the numerical simulations, allows reaching higher deformation values and consequently higher mechanical properties. The main remaining results are reported in Appendix.

7.2.2 Microstructure analysis

The graphs reported in Fig. 7.14 allow us to compare the grain size values in the YZ plane and the XZ plane of the samples, after a thickness reduction of 30% using the traditional setup, considering different rotational speeds, equal to a) 240 rpm, b) 420 rpm and c) 600 rpm. Also in this case, due to the results related to the microhardness, are reported an intermediate process result, and was analysed the trend of variation of the grain size increasing the equivalent plastic strain, while the results regarding the various thickness reductions are reported in the Appendix in terms of

percentage increases. In reporting the average values, the tube section was divided into three parts, grouping the results for each part. The error bars represent the standard deviation of the grain size for each position, obtained using the four Heyn intercept lines results, as reported in Section 6.2.3.

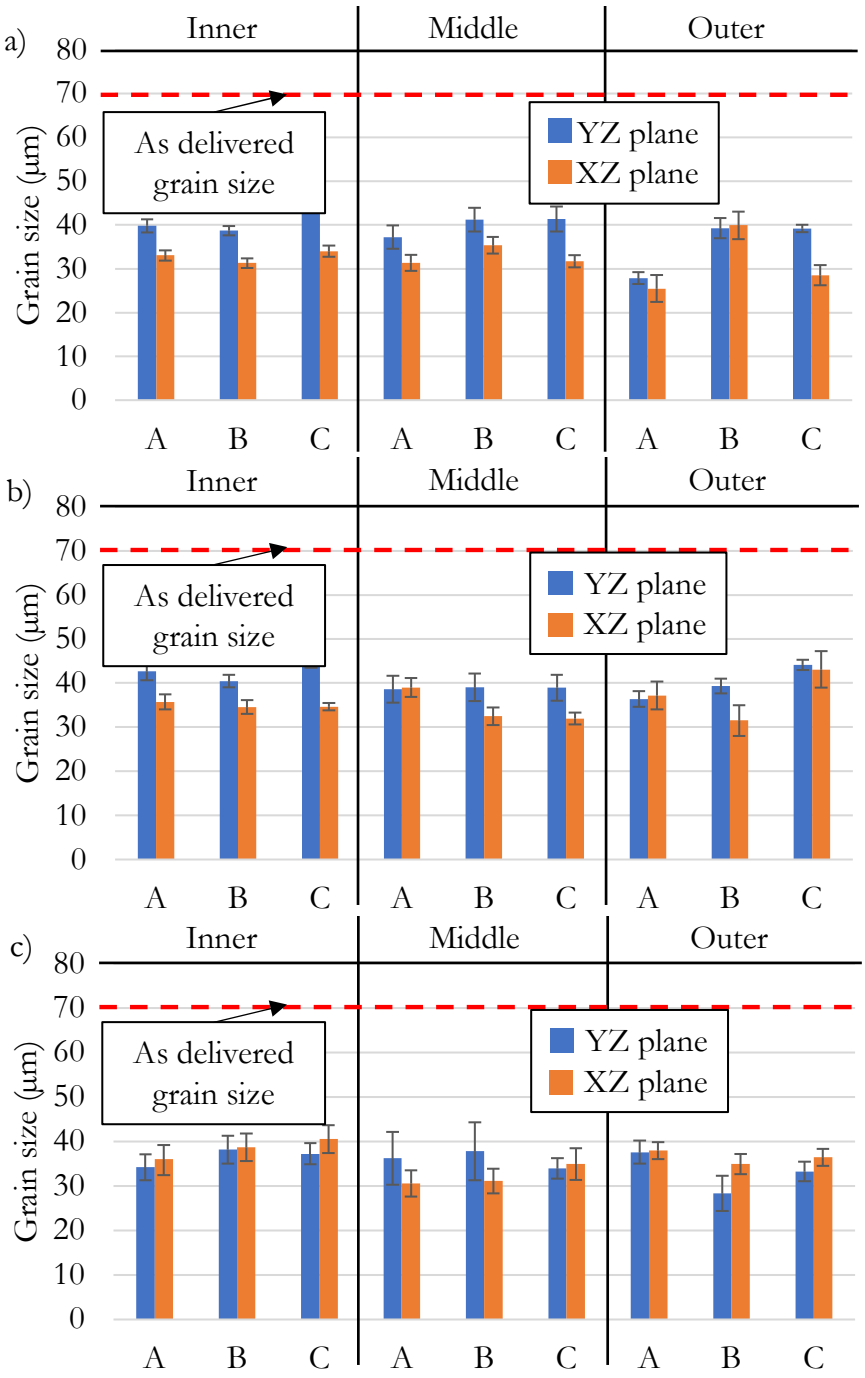

Fig. 7.14 *- Grain size comparison among different mandrel speeds after a th. reduction equal to 30% for sections: A - 10 mm, B - 20 mm, C - 30 mm, considering a) 240 rpm, b) 420 rpm, c) 600 rpm.*

It is possible to notice that, concerning the as-delivered microstructure, reported

with the line in the graphs, in the entire tube, there is a refinement in the grain size and increasing the rotation speed, comparable grain sizes are obtained. Considering the YZ and the XZ planes, it is possible to notice how the grain sizes are similar in the middle and outer portions of the tube, while in the inner layer, considering a rotational speed equal to 420 rpm and 420 rpm, the YZ plane grain size is larger than XZ. Looking at the dispersion of results, it is possible to notice how increasing the rotational speed, there is an increase in the result dispersion. This result is related to a technical issue: augmenting the rotational speed, the vibrations become increasingly more significant, causing an intermittent contact between the tube and the roller.

For a thickness reduction equal to 30%, the grain size variations are reported in Tab. 7.10. The average is comprised between -45% and -47% considering the internal radius of the tube, -48% and -51% considering the middle radius, and between -45% and -52% considering the outer portion. Considering the entire tube, the grain size decreases from 70±17 μm to an average value of 36±10 μm, equivalent to -48%.

Tab. 7.10 *- Grain size considering different rotational speeds.*

ω (rpm)	Inner	Middle	Outer	$Av._{rot\ speed}$
240	-47%	-48%	-52%	-49%
420	-45%	-48%	-45%	-46%
600	-46%	-51%	-50%	-49%
$Av._{layer}$	-46%	-49%	-49%	**-48%**

The graphs reported in Fig. 7.15 allow us to compare the grain size values in the YZ plane and the XZ plane of the samples, after a thickness reduction of 24% using the constrained solution, considering different rotational speeds, equal to a) 240 rpm, b) 420 rpm and c) 600 rpm. These values have been reported here because they are comparable with those obtained with the traditional setup with the same thickness reduction (grey column). For simplicity, the average value between the value of the XY and YZ planes has been reported.

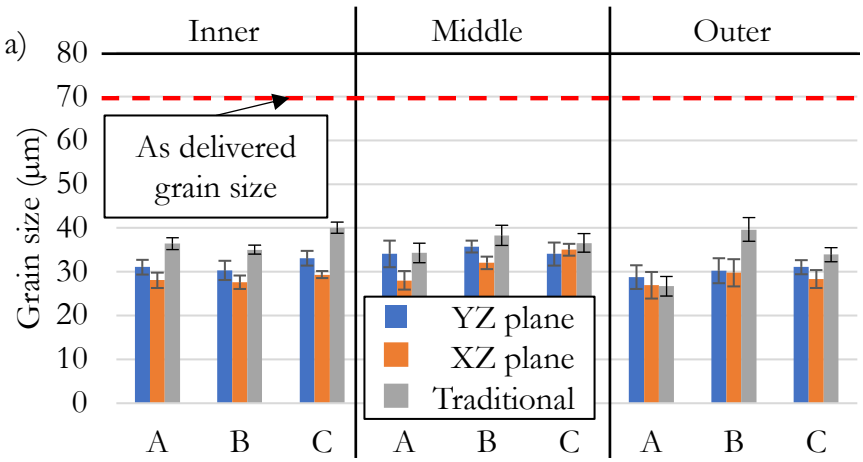

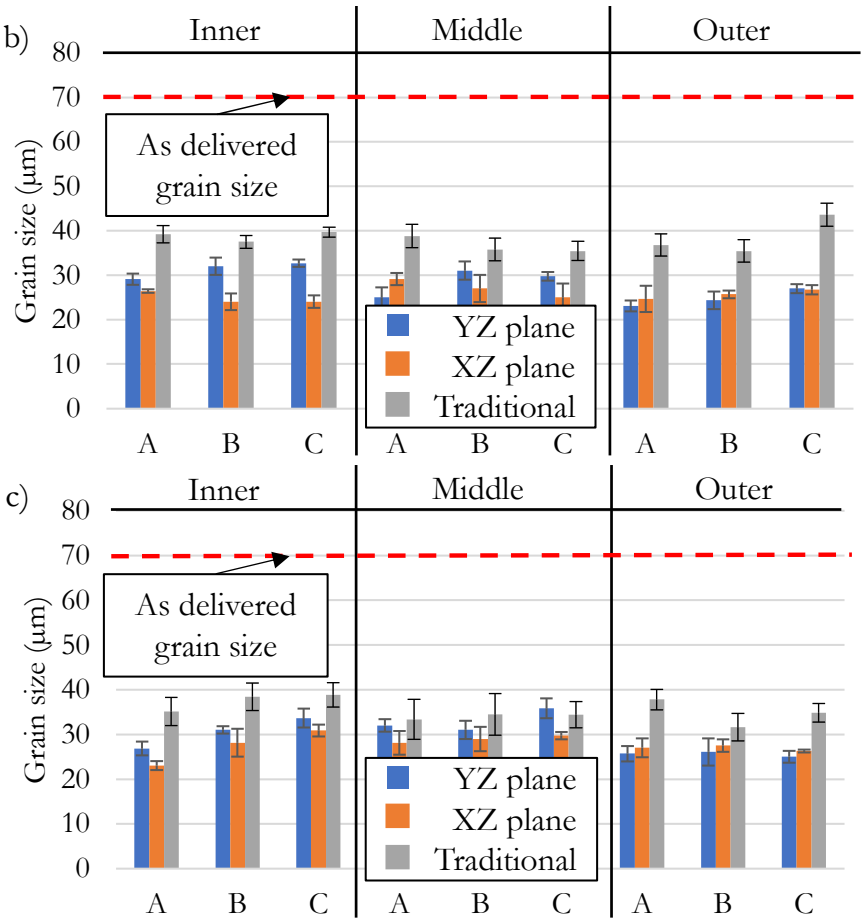

Fig. 7.15 *- Grain size comparison among different mandrel speeds after a th. reduction equal to 24% for sections: A - 10 mm, B - 20 mm, C - 30 mm, considering a) 240 rpm, b) 420 rpm, c) 600 rpm.*

It is possible to notice that, concerning the as-delivered microstructure, reported with the line in the graphs, in the entire tube, there is a refinement in the grain size and increasing the rotation speed, comparable grain sizes are obtained, accordingly with the microhardness measurements. Considering the YZ and the XZ planes, it is possible to notice how the grain sizes are similar, according to the results obtained in the microhardness analysis. Looking at the dispersion of results, like the microhardness results, it is possible to notice how this value remains low due to the low influence of vibrations damped by the constrained setup.

Tab. 7.11 *- Grain size considering different rotational speeds.*

ω (rpm)	Inner	Middle	Outer	$Av._{rot\ speed}$
240	-57%	-53%	-58%	-56%
420	-60%	-60%	-64%	-61%
600	-59%	-56%	-62%	-59%
$Av._{layer}$	-59%	-56%	-62%	**-59%**

Considering a thickness reduction equal to 24%, the grain size variations are

reported in Tab. 7.11. The average is between -57% and -60% considering the internal radius of the tube, -53% and -60% considering the middle radius, and between -58% and -64% considering the outer portion. Considering the entire tube, the grain size decreases from 70±17 μm to an average value of 28±7 μm, equivalent to -59%. The error related to the average grain size comprehends the dispersion of the results, from the minimum to the maximum value.

The graphs reported in Fig. 7.16 allow us to compare the grain sizes in the YZ plane and the XZ plane of the samples, after a thickness reduction of 30% using the traditional solution, considering different feed rates, equal to a) 1 mm/s, b) 1,5 mm/s and c) 2 mm/s. The error bars represent the dispersion of the results for each group, considering the minimum and maximum values as the upper and lower limits. It is possible to observe that also in this case, for each cross-section, there is a decrease in the grain size between the internal and external portion of the specimens, and by increasing the feed rate, higher grain refinement is obtained, accordingly with the numerical simulation and microhardness results.

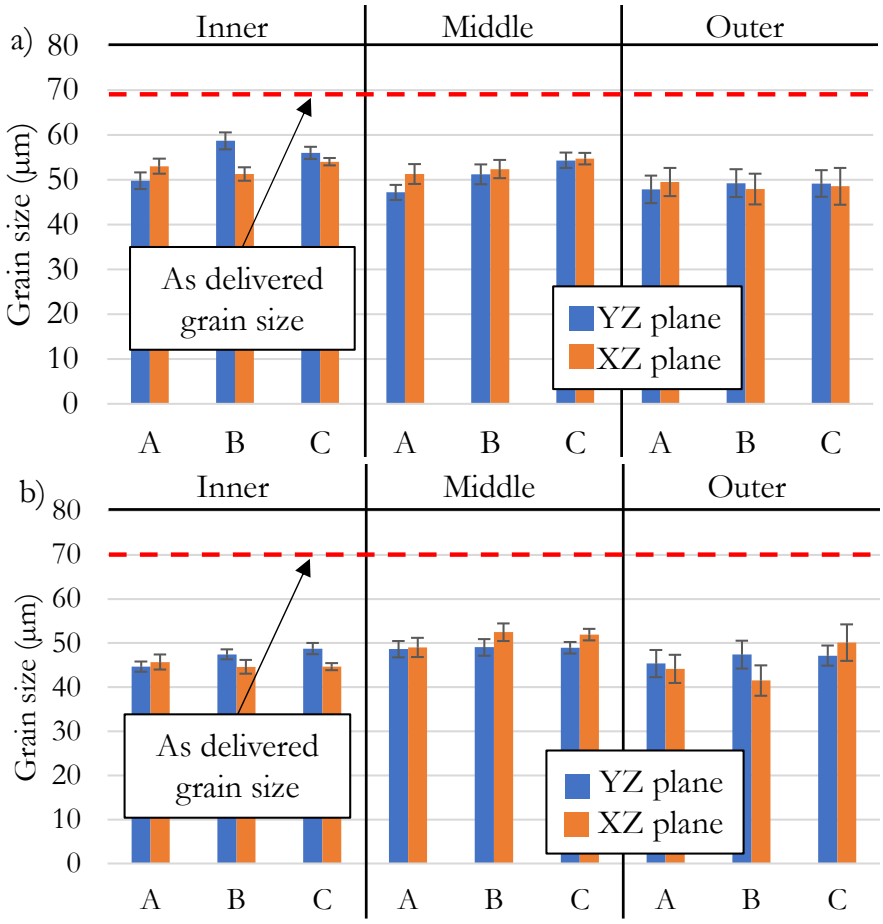

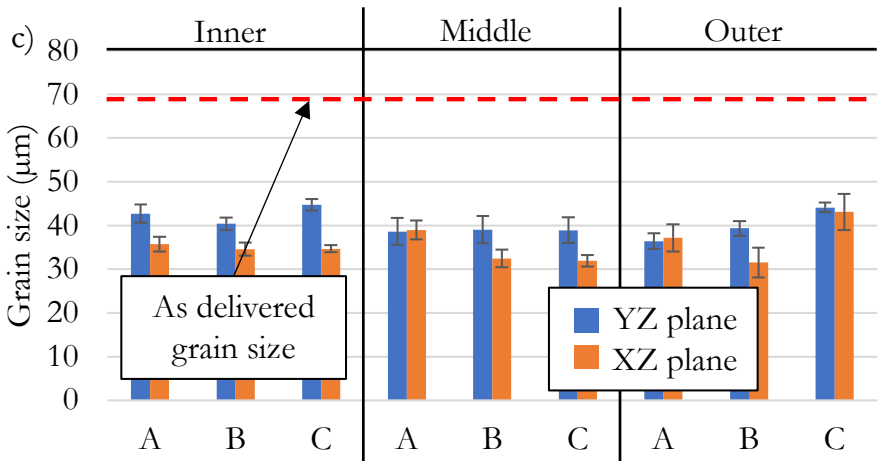

Fig. 7.16 *- Grain size comparison among different feed rates after a th. reduction equal to 30% for sections: A - 10 mm, B - 20 mm, C - 30 mm, considering a) 1 mm/s, b) 1,5 mm/s, c) 2 mm/s.*

Considering a thickness reduction equal to 30%, the feed rate's grain size variations are reported in Tab. 7.12. The average is between -23% and -45% considering the internal radius of the tube, -26% and -48% considering the middle radius, and between -30% and -45% considering the outer portion. Considering the entire tube, the grain size decreases from 70±17 µm to an average value of 45.6±10 µm, equivalent to -35%. The error related to the average grain size comprehends the dispersion of the results, from the minimum to the maximum value.

Tab. 7.12 *- Grain size considering different feed rates.*

***f*(mm/s)**	**Inner**	**Middle**	**Outer**	**Av.$_{\text{feed rate}}$**
1.0	-23%	-26%	-30%	-26%
1.5	-34%	-29%	-34%	-32%
2.0	-45%	-48%	-45%	-46%
Av.$_{\text{layer}}$	-34%	-34%	-37%	**-35%**

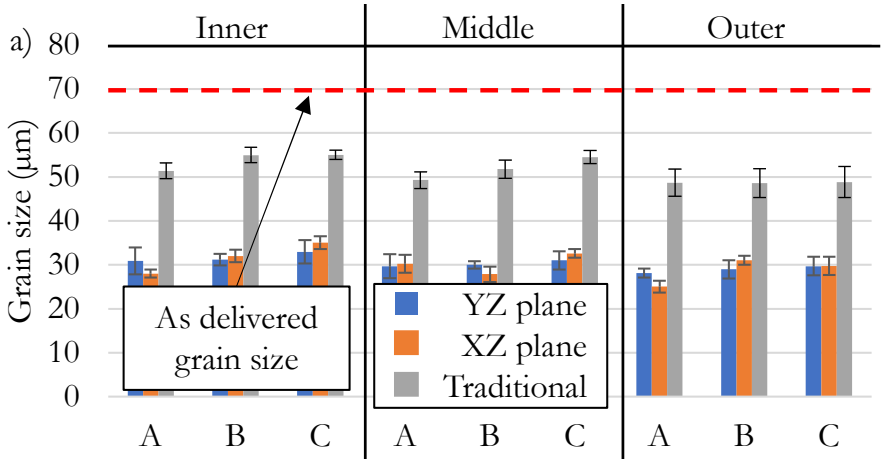

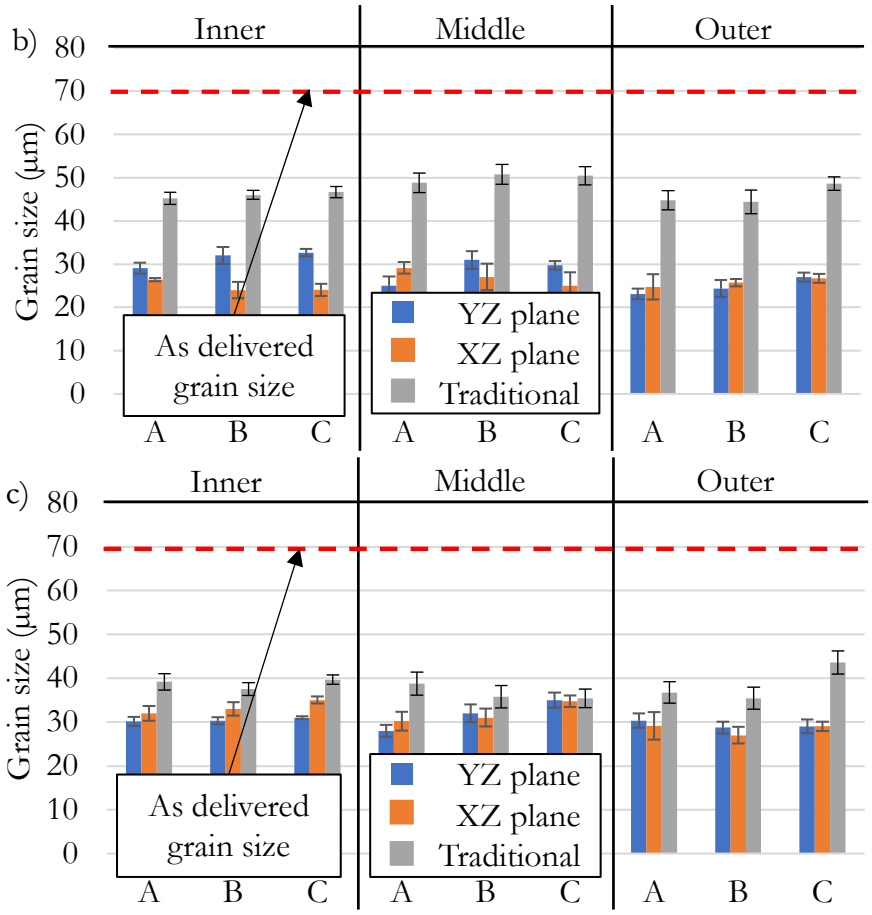

Fig. 7.17 *- Grain size comparison among different feed rates after one pass for sections: A - 10 mm, B - 20 mm, C - 30 mm, considering a) 1 mm/s, b) 1,5 mm/s, c) 2 mm/s.*

The graphs reported in Fig. 7.17 allow us to compare the grain sizes in the YZ plane and the XZ plane of the samples, after a thickness reduction of 24% using the constrained setup, considering different feed rates, equal to a) 1 mm/s, b) 1,5 mm/s and c) 2 mm/s. It is possible to observe that in this case, there is a decrease in the grain size between the internal and external portions of the specimens for each cross-section. The influence of the feed rate in grain refinement is not linear: as this kinematic parameter increases, a high refinement is reached for a value of 1.5 mm/s, but then similar results are obtained considering a feed rate of 1 mm/s and 2 mm/s.

It is possible to observe that in this case, there is a decrease in the grain size between the internal and external portions of the specimens for each cross-section. The influence of the feed rate in grain refinement is not linear: as this kinematic parameter increases, a high refinement is reached for a value of 1.5 mm/s, but then similar results are obtained considering a feed rate of 1 mm/s and 2 mm/s. The variations of the grain size varying the feed rate are reported in Tab. 7.13. The average is between -54% and -60% considering the internal radius of the tube, -55% and -60% considering the middle radius, and between -59% and -64% considering the outer

portion. Considering the entire tube, the grain size decreases from 70±17 μm to an average value of 29±6 μm, equivalent to -58%.

Tab. 7.13 *- Grain size considering different feed rates.*

***f*(mm/s)**	**Inner**	**Middle**	**Outer**	**Av.$_{\text{feed rate}}$**
1.0	-55%	-57%	-59%	-57%
1.5	-60%	-60%	-64%	-61%
2.0	-54%	-55%	-59%	-56%
Av.$_{\text{layer}}$	-56%	-57%	-61%	**-58%**

Since the data relating to a 48% reduction in thickness are not available for the traditional setup, the values relating to the grain refinement obtained with the constrained process are summarized in Tab. 7.14 and Tab. 7.15 in terms of average results. There is a similar grain refinement for each cross-section between the internal and external portions of the specimens, but consistent results are obtained even by varying the rotation speed. As for the traditional setup, also in this case, the feed rate influences the grain refinement, however with a different trend: while in the traditional flowforming higher the feed rate, higher the grain refinement, in the constrained solution, the refinement increases until a feed rate equal to 1.5 mm/s and then decreases for higher values of feed rate. However, this innovative solution guarantees a higher grain refinement increasing the thickness reduction, not having the saturation behaviour typical of the traditional setup. The average grain size is equal to 13±7 μm, with a decrease of -80% with respect to the as-delivered conditions.

Tab. 7.14 *- Grain size considering different rotational speeds.*

ω (rpm)	**Inner**	**Middle**	**Outer**	**Av.$_{\text{rot speed}}$**
240	-77%	-79%	-81%	-79%
420	-81%	-81%	-84%	-82%
600	-76%	-80%	-79%	-78%
Av.$_{\text{layer}}$	-78%	-80%	-81%	**-80%**

Tab. 7.15 *- Grain size considering different feed rates.*

***f*(mm/s)**	**Inner**	**Middle**	**Outer**	**Av.$_{\text{feed rate}}$**
1.0	-75%	-77%	-73%	-75%
1.5	-81%	-81%	-84%	-82%
2.0	-74%	-81%	-80%	-78%
Av.$_{\text{layer}}$	-77%	-80%	-79%	**-78%**

The graphs of Fig. 7.18 describe the variation in the grain size as the thickness reduction varies, considering the YZ and XZ planes, using the traditional setup. Comparing with the as-delivered grain size equal to 70±17 μm, it is possible to notice a gradient moving from the outer portion to the inner portion of the tube. As for the

microhardness, also in this case, there is a saturation phenomenon: the grain size, while increasing the thickness reduction, does not vary. What varies is the portion of material having the same microstructural characteristic. In this case, due to the different nature of the test, which is not as punctual as the microhardness test, it is not possible to obtain a grain size radius dependence.

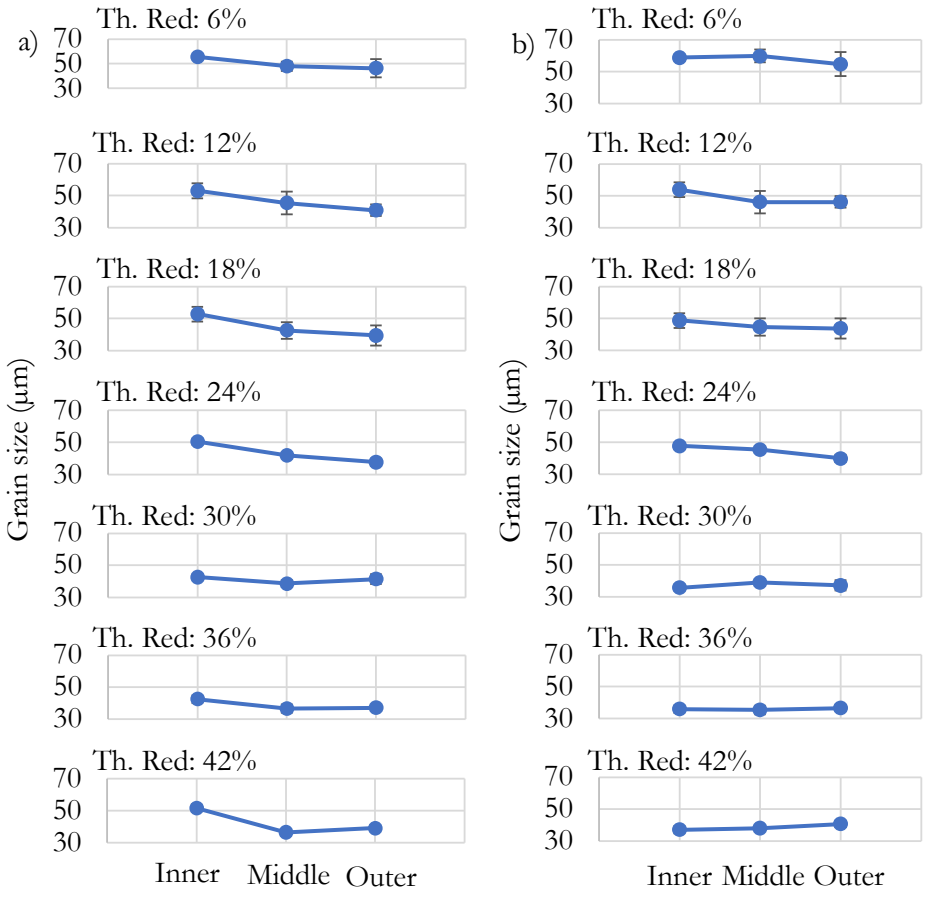

Fig. 7.18 *- Grain size comparison among different thickness reduction using a mandrel speed equal to 420 rpm in the a) YZ and b) XZ planes considering Section A.*

Analysing the grain shape obtained through the traditional and the constrained processes, it is possible to notice how it is different. In Fig. 7.19, the micrographs of the outermost portion of the tube processed via the traditional process are reported, as in these, it is possible to observe the greatest changes in grain size and shape occur. It can be seen how the deformation mechanism involves an elongation of the grain in a direction parallel to the feed direction. Considering the microstructure obtained through the constrained setup (Fig. 7.20) and the smaller grain size, it is possible to notice fewer grains elongation and distortion. To this end, the anisotropy of the grain was evaluated, and all four intercepts were considered, comparing the dimensions of the grain obtained with perpendicular lines.

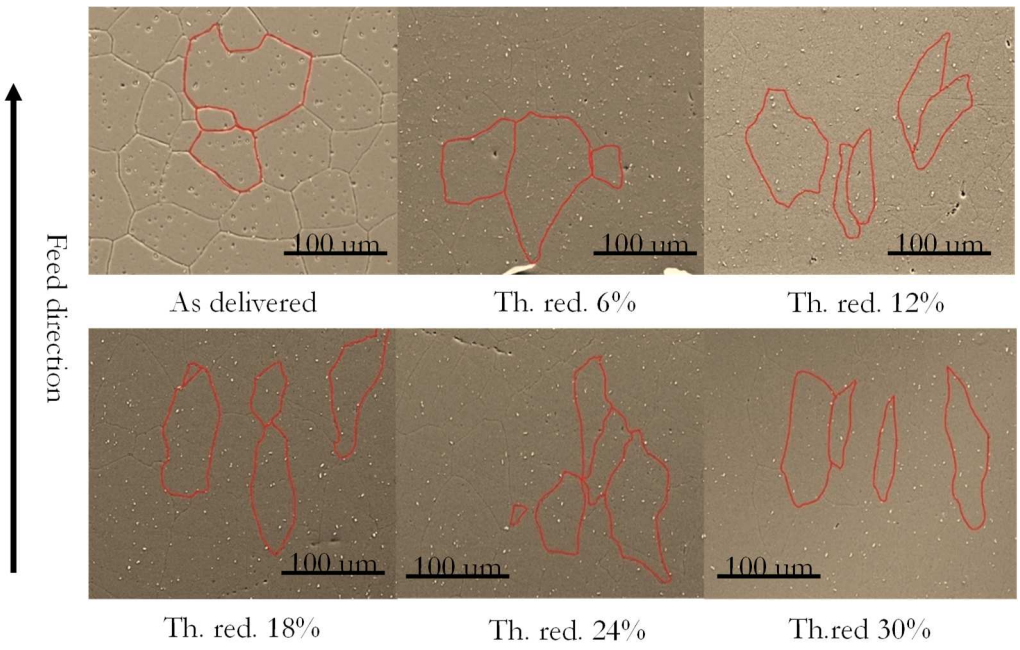

Fig. 7.19 *- Micrographs comparison among different thickness reduction using traditional setup.*

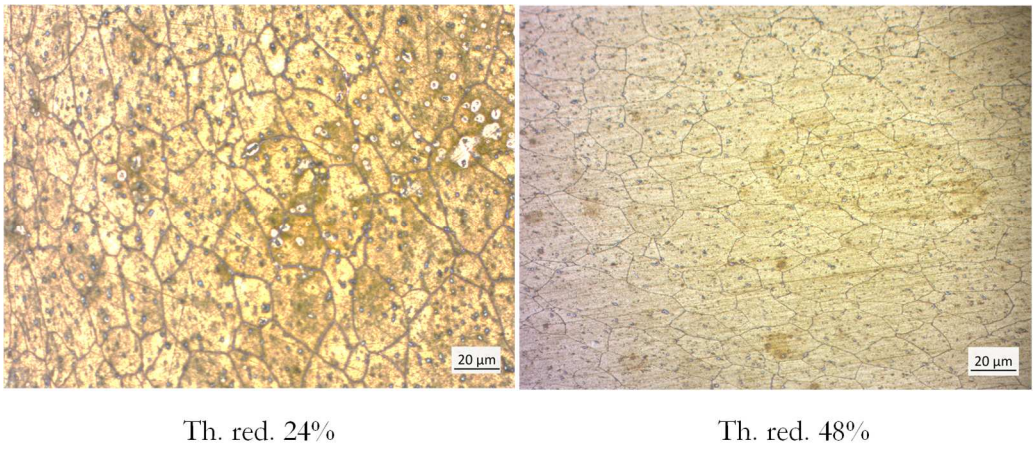

Fig. 7.20 *- Micrographs comparison among different thickness reduction using constrained setup.*

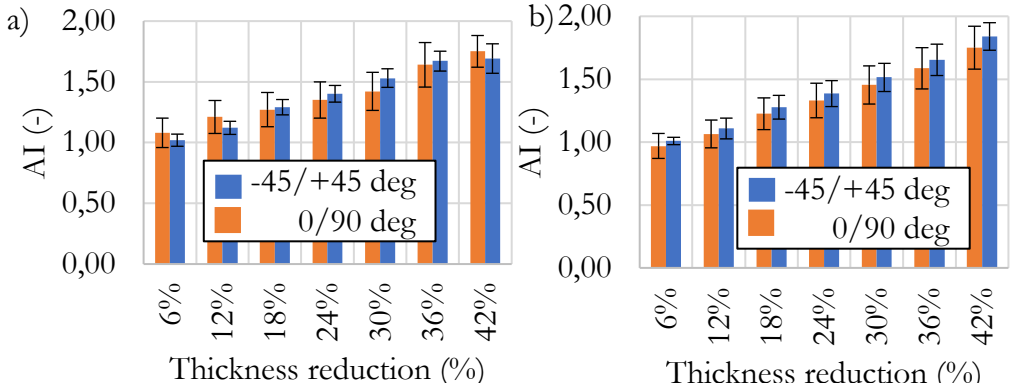

Fig. 7.21 *- AI of grain considering a) XZ and b) YZ plane.*

Considering the traditional setup, it is possible to observe in Fig. 7.21 how the anisotropy index varies from an approximately unitary value (characteristic of an equiaxed structure) to a value equal to approximately 1.7 (characteristic of a very distorted crystalline structure). The error of every single measurement refers to the different micrographs available concerning the same radius, thus considering the dispersion of the results. It is possible to observe how the results obtained considering the lines 0/90 degrees and -45/+45 degrees provide consistent results.

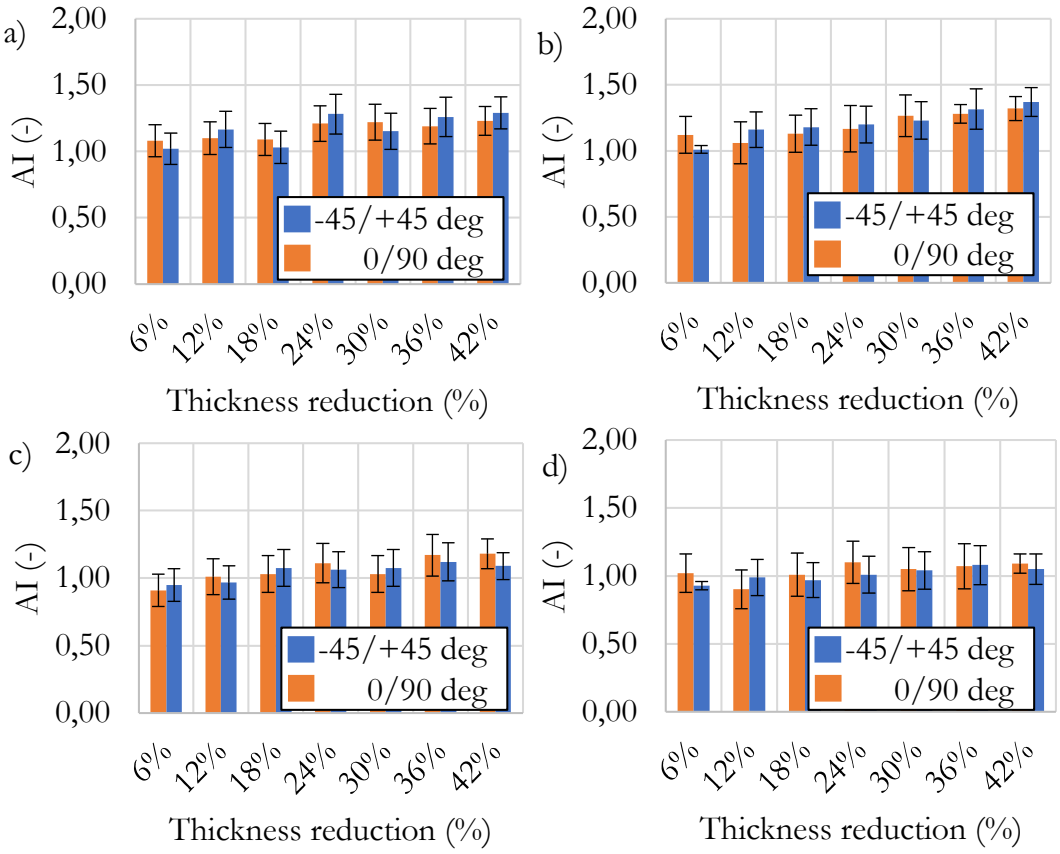

Fig. 7.22 *- AI of grain considering a) XZ and b) YZ plane for the middle radius and AI of grain considering c) XZ and d) YZ plane for the inner radius.*

The variation of the anisotropy index considering the inner and the middle portion of the tube is lower than the outer radius, as reported in Fig. 7.22. Considering the middle radius, the maximum *AI* is 1.37, while considering the inner radius, the maximum *AI* is equal to 1.17. This demonstrates how the grain shape varies both along the radius and increasing the deformation. In addition, analysing the anisotropy in the grain shape and comparing the traditional and the constrained processes, it is possible to notice how the anisotropy increases in the traditional solution, increasing the thickness reduction. In contrast, the anisotropy remains near a unitary value with higher thickness reduction in the constrained solution, as reported in Fig. 7.23.

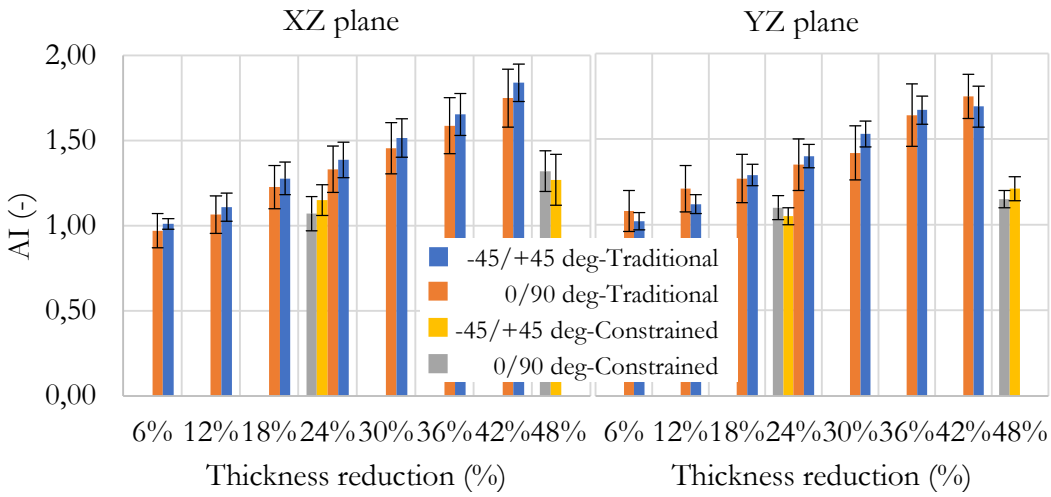

Fig. 7.23 *- AI of grain considering a) XZ and b) YZ plane for the outer radius.*

Tab. 7.16 reports the anisotropy values considering both the XZ plane and the YZ plane, as the thickness reduction varies, considering the outer radius of Section *A*.

Tab. 7.16 *- AI considering XZ and YZ planes for the traditional setup.*

	XZ plane				**YZ plane**			
#	$AI_{0/90}$	$\Delta AI_{0/90}$	$AI_{-45/45}$	$\Delta AI_{-45/45}$	$AI_{0/90}$	$\Delta AI_{0/90}$	$AI_{-45/45}$	$\Delta AI_{-45/45}$
6%	1.08	0.12	1.02	0.05	0.97	0.14	1.01	0.03
12%	1.21	0.13	1.12	0.05	1.07	0.15	1.11	0.13
18%	1.27	0.14	1.29	0.06	1.23	0.18	1.28	0.15
24%	1.35	0.15	1.4	0.07	1.33	0.19	1.39	0.17
30%	1.42	0.16	1.53	0.08	1.46	0.21	1.52	0.18
36%	1.64	0.18	1.67	0.08	1.59	0.23	1.65	0.20
42%	1.75	0.23	1.69	0.12	1.75	0.27	1.84	0.21

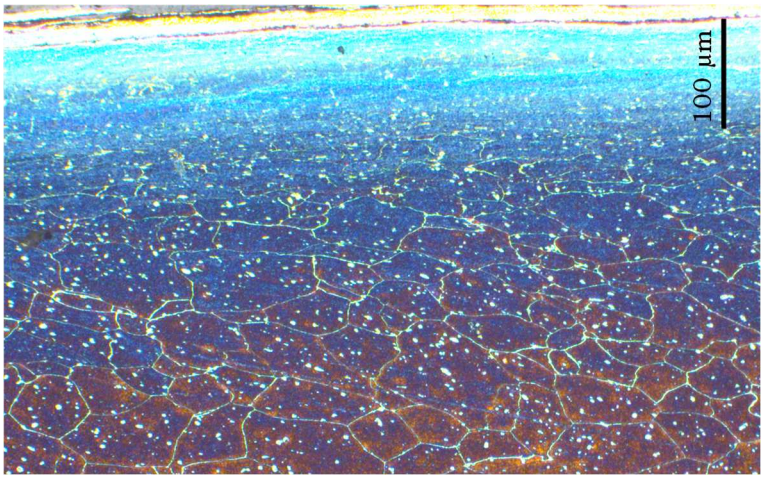

Fig. 7.24 *- Example of a high refined layer.*

Analysing the micrographs (by way of example, the one in Fig. 7.24 is shown), it is possible to see in the external portion of the tube a thickness in which the microstructural analysis is not possible due to the impossibility of recognizing the grain boundaries while varying the time of exposure to chemical etching and also trying different chemical etchings. This layer, containing highly distorted grains, is characterized by grains of submicrometric dimensions, typical of SPD processes, which make the size of the grains shown in the previous graphs greater than the real one. Further investigations on the possible characteristics of this highly refined layer are necessary to evaluate specific uses, such as examples in components for very corrosive environments.

For the sake of completeness, the average thicknesses of these layers are reported as the thickness reduction varies (Fig. 7.25), averaging the results obtained between the various micrographs, distinguish the various sections considered. It can be noted that the thickness of the layer remains close to a constant value for the three sections considered with the same thickness reduction, maintaining a linear trend as the deformation increases. This result can be very useful as it is possible to have the constancy of the properties in the axial direction of the tube or on the same face of the sheet.

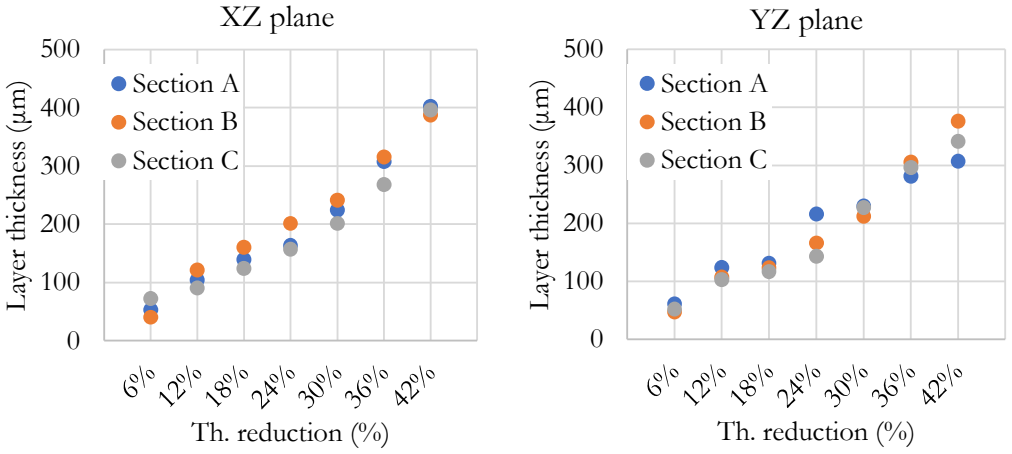

Fig. 7.25 *- High refined thickness (in µm).*

7.2.3 Tensile test

To investigate the variation in the mechanical properties of the entire tube after the flowforming process, three tensile specimens were cut and tested from each sample. Fig. 7.26 reports the results of the tensile tests carried out at room temperature and a strain rate of 1 s^{-1} in terms of the average values of yield strength, UTS, and maximum elongation considering the constrained and the traditional solution. Then the results of the flowformed samples are compared with the results of the as-delivered tubes.

Tab. 7.17 *- Mechanical characteristics for different th. reduction.*

	6%	12%	18%	24%	30%	36%	42%
Yield stress	+4%	+6%	+10%	+20%	+18%	+16%	+15%
UTS	+13%	+18%	+21%	+24%	+23%	+22%	+17%
Elongation	-70%	-71%	-74%	-75%	-76%	-76%	-75%

It is possible to observe that after the traditional flowforming process, the workpiece shows a reduction of the maximum elongation, thus of its ductility, depending on the hardening behaviour of the material, only for a thickness reduction lower than 30%. After this deformation, the maximum elongation augments respect the minimum value, being lower if compared with the as-delivered value. However, the UTS and yield strength values increase until a thickness reduction between 24% and 30%. After these plateaux, these properties decrease, accordingly with a slight increase in the ductility. Following the results of microhardness and grain size, there is no further increase in the mechanical characteristics of the material but a stable value of the quantities considered.

Tab. 7.18 *- Mechanical characteristics for different th. reduction.*

	Traditional	Constrained	Traditional	Constrained
	24%	24%	42%	48%
Yield stress	+20%	+26%	+15%	+31%
UTS	+24%	+31%	+17%	+36%
Elongation	-75%	-79%	-75%	-81%

Analysing the results obtained through the constrained backward tube flowforming, it is possible to observe that the workpiece shows a reduction of the maximum elongation, thus of its ductility, if compared with the traditional process. On the other hand, both the UTS and yield strength values increase, considering a thickness reduction of 48%, following microhardness and grain size refinement.

Considering the larger/smaller values obtained using the traditional solution, the results show an increase up to 35 MPa (+20%) in the value of the yield stress and a reduction of 76% in terms of maximum elongation at fracture. Regarding the UTS values, if compared with the as-delivered values, there is an absolute increment of +48 MPa, corresponding to a percentage increment of +24%. Considering the constrained solution, the results show an increase up to 55 MPa (+31%) in the value of the yield stress and a reduction of 81% in terms of maximum elongation at fracture. Regarding the UTS values, if compared with the as-delivered values, there is an absolute increment of +71 MPa, corresponding to a percentage increment of +36%.

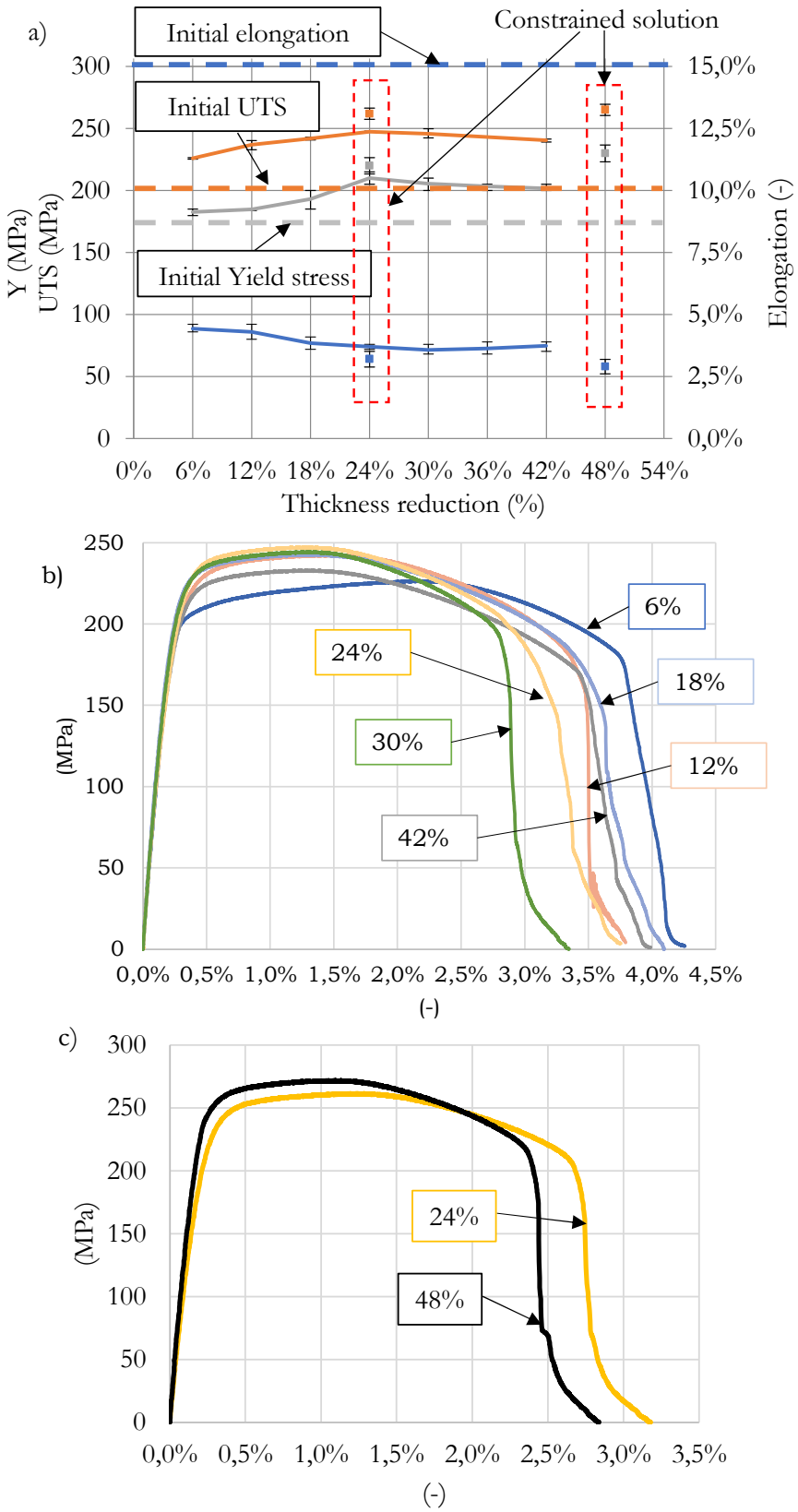

Fig. 7.26 *- a) Tensile test results and tensile test curves of the b) traditional and c) constrained setup.*

7.2.4 Geometrical analysis

To assess the reliability of the FE model, the numerical results were compared to experimental measurements carried out on the flowformed tubes. Fig. 7.27 plots the tube elongation vs. the thickness reduction for the numerical simulations and the experimental CMM measurements obtained considering the traditional setup. The same results were compared with the analytical calculation according to the model developed by Wong *et al.* [93], in which the final length is evaluated using the following equation:

$$L_1 = L_0 \frac{t_0(d_{int}+t_0)}{t_1(d_{int}+t_1)} \qquad Eq.\ 9$$

where L_0 is the initial length, d_{int} is the workpiece's internal diameter, and t_0 and t_1 are the initial and final tube thickness. It is possible to note how the analytical results overestimate the experimental results due to the hypothesis of the absence of tangential flow of the analytical model, which was not detected in the experiments.

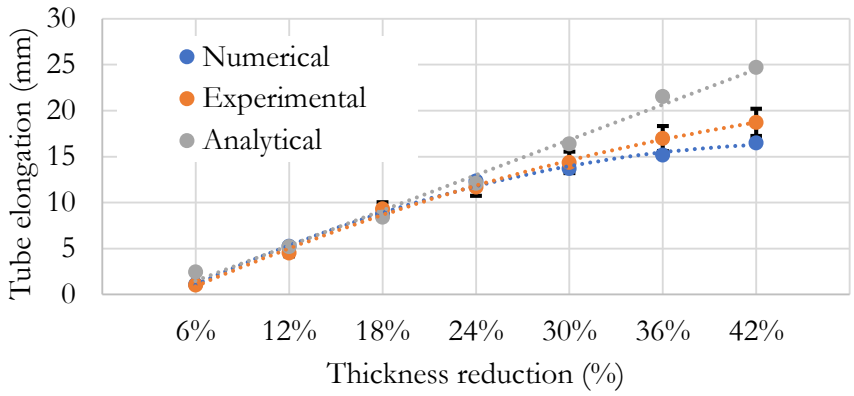

***Fig. 7.27** - Comparison of the tube elongation from simulations, experiments, and analytical model varying the thickness reduction.*

The comparison between the numerical and experimental results shows that the numerical model is coherent since compatible results are obtained by considering the dispersion of the experimental results, expressed with the use of error bands until the thickness reduction is lower than 30%. After this value, the experimental elongation is larger than the numerical, also considering the error bars. In addition, the analytical trend is linear, while both the experimental and numerical results follow a quadratic trend. Furthermore, the cross-section roundness and thickness results were compared, measured by a CMM after each pass. This analysis allows investigating geometrical differences among different tube sections due to process characteristics as the vibrations during the flowforming. Higher values of roundness mean that the deformation imposed by the roller is not stable and that the rollers do not remain in the correct position during the process due to not-stiffness roller shafts. The shape of the tube is similar to the representation in Fig. 7.28a, where the blue circle has three

lobes spaced circumferentially at 120 deg as the rollers. The differences with the nominal circumference, represented by the red line, are lower than 15 µm for Section *A* and *B* and lower than 45 µm for Section *C*, which is the one furthest away from the constrained portion reported in Fig. 7.28b. This means that the stiffness of the developed setup does not allow for dampening the vibrations during the process, affecting the shape of the component and limiting the tube length that can be processed.

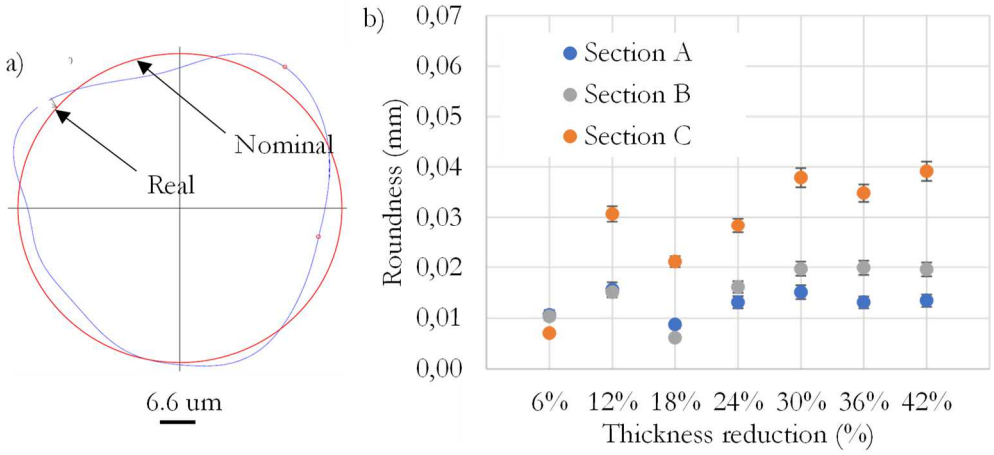

Fig. 7.28 *- a) Comparison between real and nominal shape, b) Roundness values.*

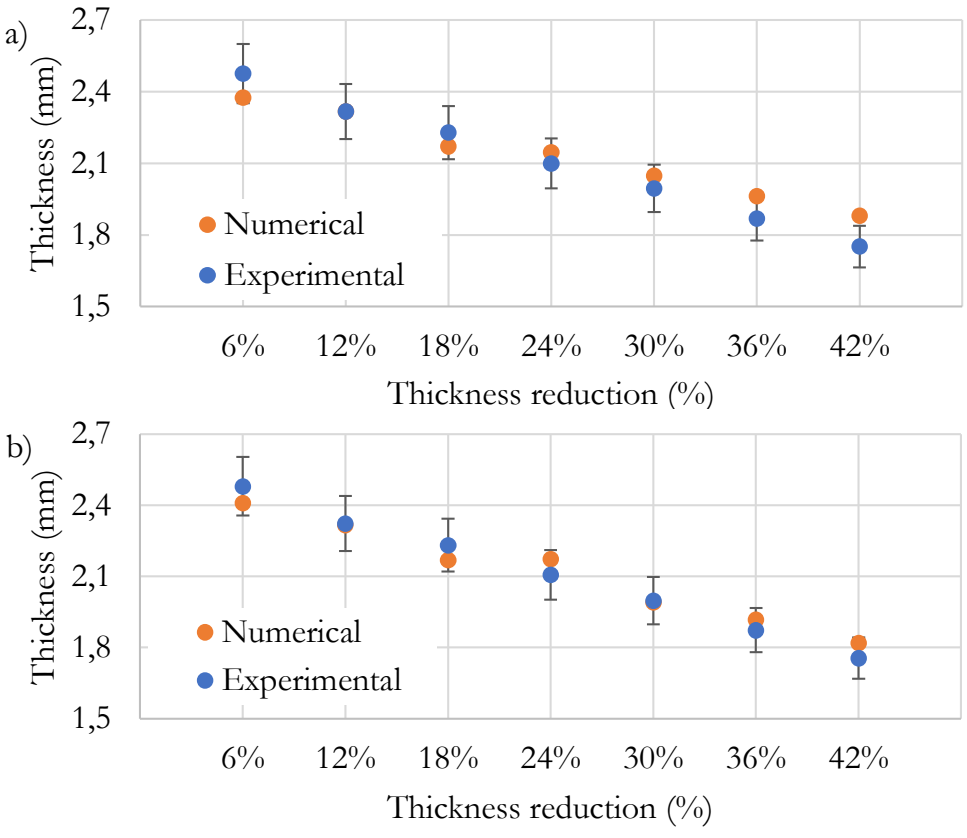

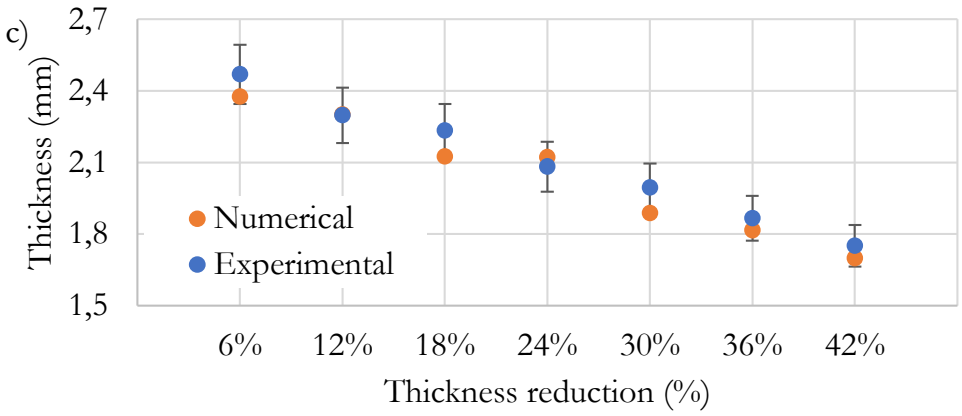

Fig. 7.29 *- Thickness comparison among different thickness reduction considering a) Section A, b) Section B, and c) Section C.*

About the thickness, Fig. 7.29 shows the comparison of the tube thickness of Section a) *A*, b) *B,* and c) *C* between the numerical simulation and the experiments. As for the elongation, the results of the numerical simulations agree with the experimental results regarding thickness.

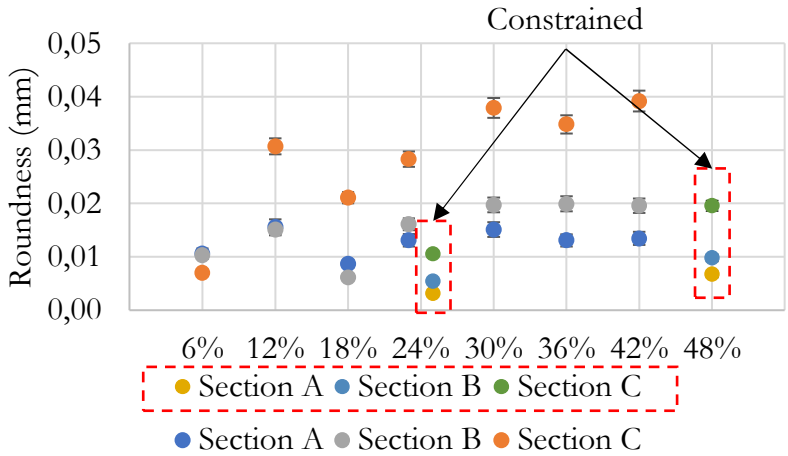

Fig. 7.30 *- Roundness comparison among different thickness reduction.*

The first comparison (Fig. 7.30) that is made to the traditional solution concerns the shape of the tube obtained after the flowforming process, evaluating the roundness of the component. Remember that the higher this value is, the more the tube was subjected to vibrations during the process. It can be noted that the roundness value is lower than the traditional solution: the rigid setup allows for less radial deflection of the shafts on which the rollers are keyed, at the same time dampening the vibratory phenomena.

About the thickness, Fig. 7.31 shows the comparison of the tube thickness of Sections a) *A*, b) *B,* and c) *C* between the numerical simulation and the experiments. As the traditional setup, also in this case, the results of the numerical simulations agree with the experimental results regarding thickness.

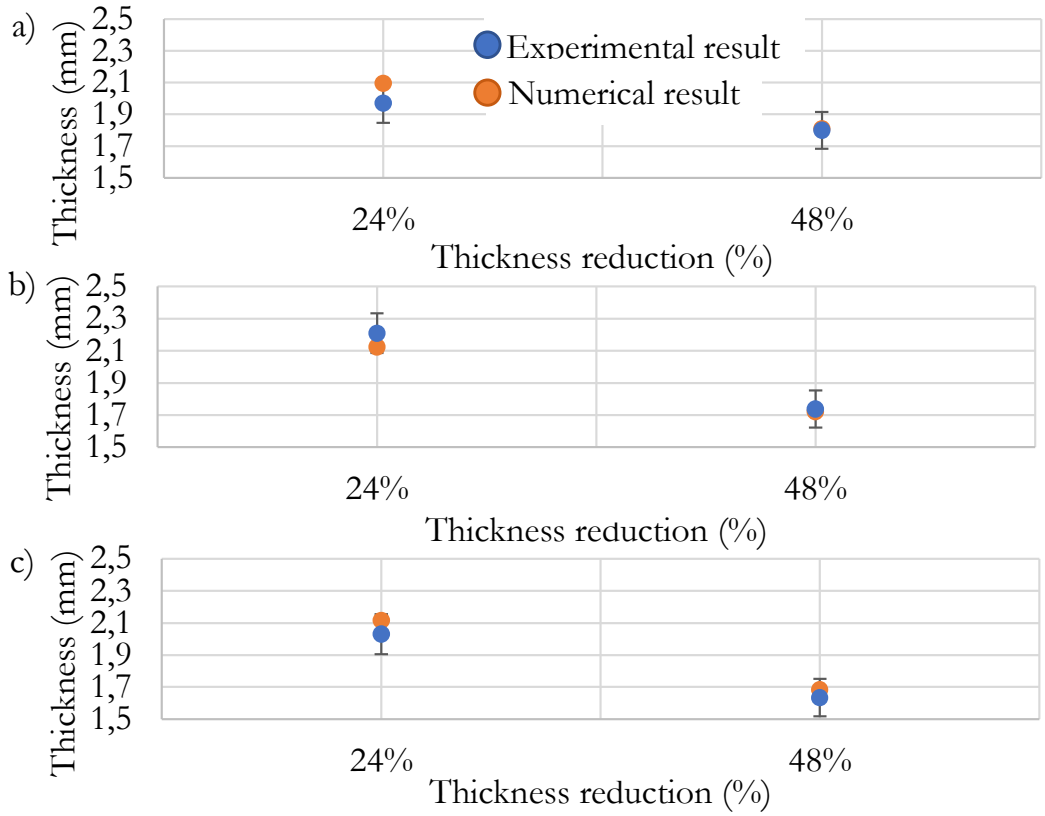

Fig. 7.31 *- Thickness comparison among different thickness reduction considering a) Section A, b) Section B, and c) Section C.*

7.3 Correlation between numerical and experimental results

7.3.1 Strain vs. Microhardness

The graphs in Fig. 7.32 show the comparison between the equivalent plastic strain (the values of Tab. 7.1) calculated through numerical simulations and the microhardness values measured in the experimental tests using the traditional setup, considering results before the saturation phenomenon that occurs after a thickness reduction equal to 30%. Analysing the slopes of the trend lines (reported in Tab. 7.19 for a better understanding), it is possible to observe that they decrease as the distance from the constrained portion increases. This means that there is a smaller increase in microhardness as a function of the equivalent plastic strain, both considering the XZ plane and the YZ plane. Regarding the analysis of the various radial positions, a greater increase in microhardness is noted in correspondence with the external and internal radius, while in the centre line, the increase is smaller, also in this case regardless of the plane considered. Evaluating the relationship between the increase in microhardness in the XZ and YZ plane, it is possible to see that the values are in a neighbourhood of 2 in all three sections considered; this means that the microhardness in the XZ plane

increases twice as compared to that of the YZ plane.

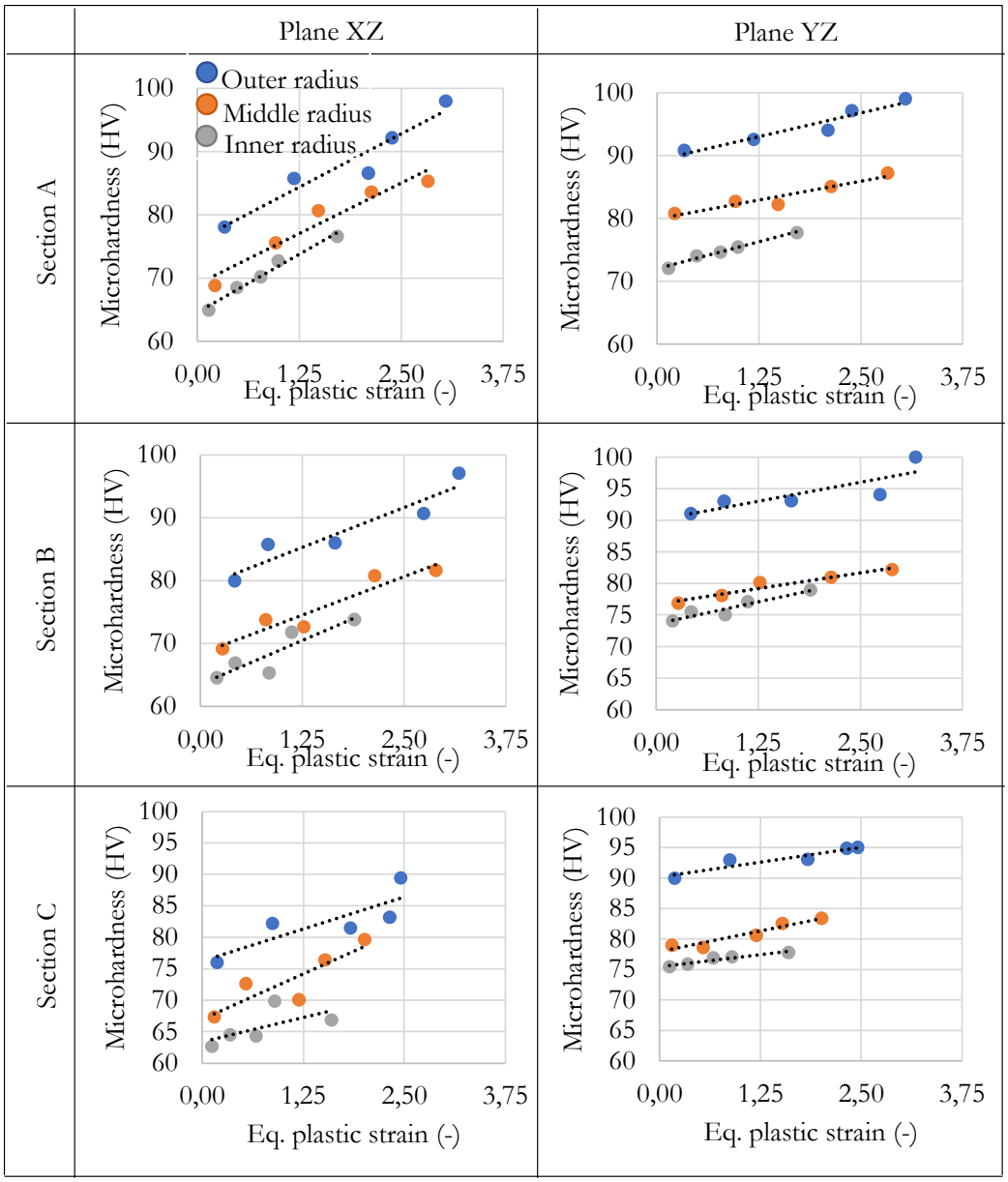

Fig. 7.32 *- Eq. plastic strain vs. Microhardness considering Section A, B and C and planes XZ and YZ.*

Tab. 7.19 *- Slope of the trend lines between strain and microhardness.*

Section	Position	m_{XZ}	m_{YZ}	m_{XZ}/m_{YZ}
A	inner	7,31	3,46	2,11
	middle	6,38	2,39	2,67
	outer	6,73	3,02	2,23
B	inner	5,57	2,79	2,00
	middle	4,91	1,99	2,46
	outer	5,07	2,40	2,11

C	inner	3,11	1,58	1,97
	middle	5,73	2,70	2,12
	outer	4,09	1,94	2,11

Considering the correlation between the equivalent plastic strain calculated through numerical simulations and the microhardness values measured in the experimental tests using the constrained setup, the graphs reported in Fig. 7.33 are obtained. Analysing the slopes of the trend lines (reported in Tab. 7.20 for a better understanding), it is possible to observe that they decrease as the distance from the constrained portion increases, as in the traditional setup. This means that there is a smaller increase in microhardness as a function of the equivalent plastic strain, both considering the XZ plane and the YZ plane. Regarding the analysis of the various radial positions, it is possible to observe an inverse relationship with the radius: a more significant increase in microhardness is noted in correspondence with the internal radius. In contrast, in the central and outer portion, the increase is smaller, also in this case regardless of the plane considered. Evaluating the relationship between the increase in microhardness in the XZ and YZ plane, it is possible to see that the values are in a neighbourhood of 1.2 in all three sections considered; this means that the microhardness in the XZ plane increases slightly more than in the YZ plane.

Tab. 7.20 *- Slope of the trend lines between strain and microhardness.*

Section	**Position**	**m_{XZ}**	**m_{YZ}**	**m_{XZ}/m_{YZ}**
A	inner	3,77	3,56	1,06
	middle	2,57	5,61	0,46
	outer	1,11	1,19	0,93
B	inner	8,02	6,48	1,24
	middle	6,20	5,44	1,14
	outer	0,80	0,63	1,28
C	inner	8,70	5,65	1,54
	middle	5,01	4,31	1,16
	outer	1,17	0,83	1,41

Finally, by evaluating the slope of the outermost portions, it is possible to note that the increase in microhardness is approximately zero: this demonstrates how in the outermost part of the tube, already after the first of the two passes, approximately a maximum value is reached, therefore close to a saturation value. The microhardness of the other sections, on the other hand, increases, homogenizing the microhardness value along the radius.

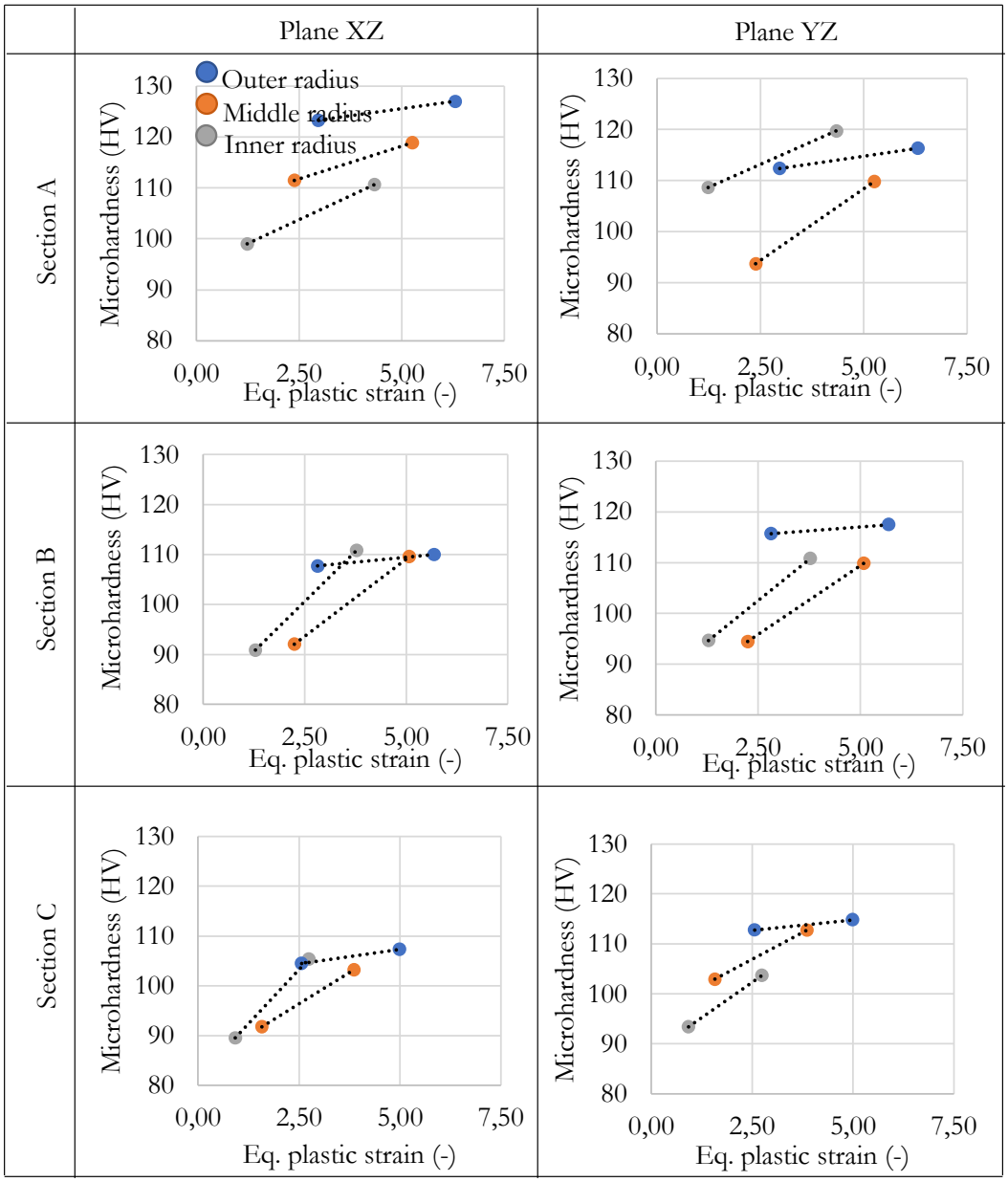

Fig. 7.33 *- Eq. plastic strain vs. Microhardness considering Section A, B, and C and planes XZ and YZ.*

7.3.2 Strain vs. Grain size

The graphs in Fig. 7.34 show the comparison between the equivalent plastic strain (the values of Tab. 7.1) calculated through numerical simulations and the grain size values measured in the experimental tests using the traditional setup, considering results before the saturation phenomenon that occurs after a thickness reduction equal to 30%. Analysing the slopes of the trend lines (reported in Tab. 7.21 for a better understanding), it is possible to observe that they do not maintain a similar value even as the distance from the constrained portion is the same.

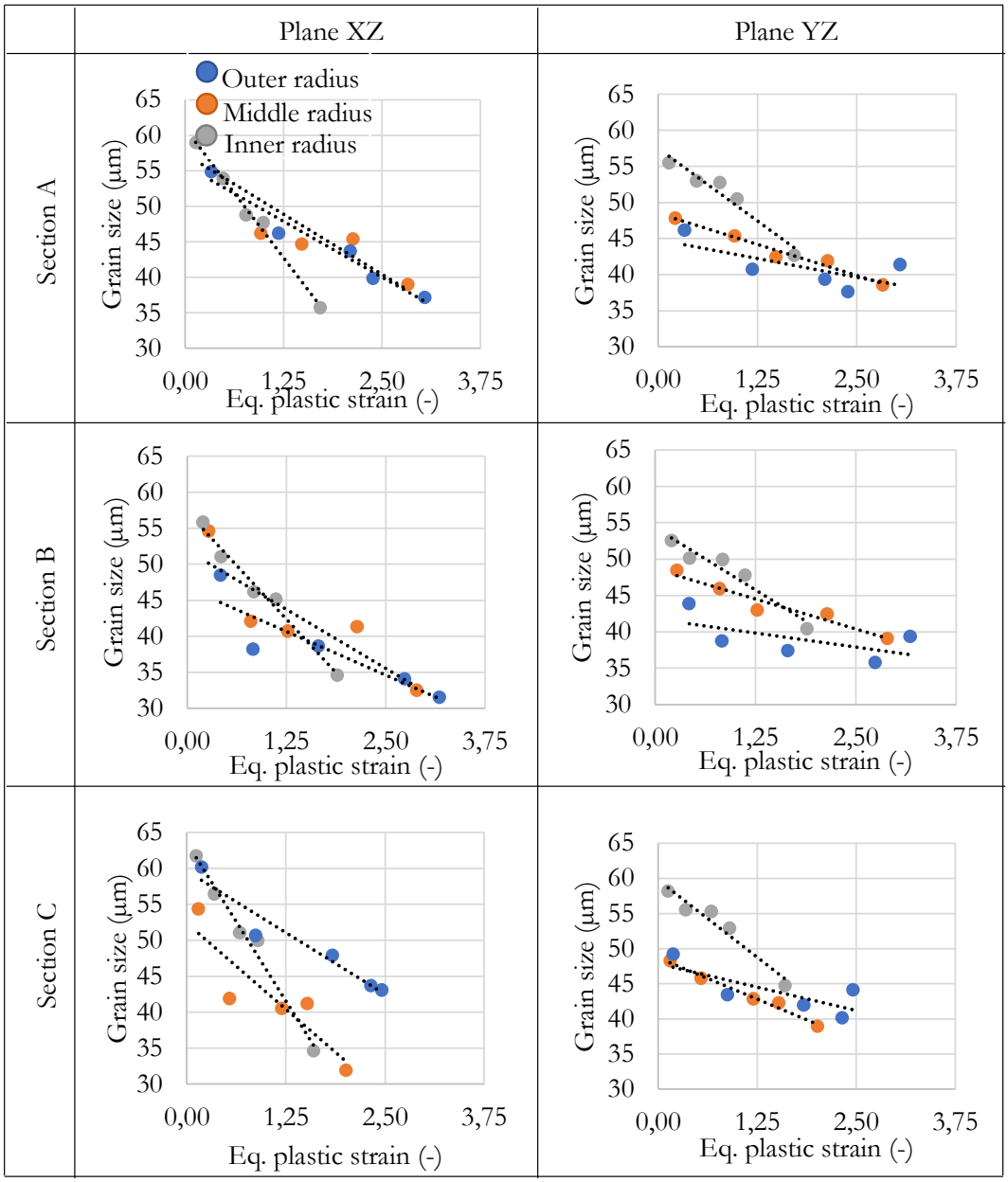

Fig. 7.34 *- Eq. plastic strain vs. Grain size considering Section A, B, and C and planes XZ and YZ.*

Regarding the analysis of the various radial positions, there is generally a greater decrease in the grain size in correspondence with the internal radius, while in the centre and external portions of the tube, the decrease is smaller, regardless of the plane considered. Evaluating the relationship between the decrease in grain size in the XZ and YZ planes, it is possible to see that the ratios are in a neighborhood of 3 in all three outer portions considered, while the ratios are at the inner and central portions around a value of 2. This means that the grain size in the YZ plane decreases 1.5 times slower than that of the XZ plane.

Tab. 7.21 *- Slope of the trend lines between strain and grain size.*

Section	Position	m_{XZ}	m_{YZ}	m_{XZ}/m_{YZ}
A	inner	-14,58	-8,04	1,81
	middle	-6,77	-3,42	1,98
	outer	-6,28	-2,08	3,02
B	inner	-11,87	-1,75	1,75
	middle	-6,57	-3,29	2,00
	outer	-4,84	-1,55	3,12
C	inner	-17,65	-8,76	2,02
	middle	-9,58	-4,72	2,03
	outer	-6,84	-2,66	2,57

The graphs in Fig. 7.35 compare the equivalent plastic strain calculated through numerical simulations and the grain size values measured in the experimental tests using the constrained backward tube flowforming process. Analysing the slopes of the trend lines (reported in Tab. 7.22 for a better understanding), it is possible to observe that in this case, they maintain a similar value even as the distance from the constrained portion is the same.

Tab. 7.22 *- Slope of the trend lines between strain and grain size.*

Section	Position	m_{XZ}	m_{YZ}	m_{XZ}/m_{YZ}
A	inner	-4,49	-3,96	1,14
	middle	-5,88	-4,95	1,19
	outer	-4,19	-5,48	0,76
B	inner	-4,77	-4,30	1,11
	middle	-4,57	-5,77	0,79
	outer	-4,02	-7,48	0,54
C	inner	-5,13	-5,76	0,89
	middle	-4,73	-6,45	0,73
	outer	-5,49	-9,86	0,56

Evaluating the relationship between the decrease in grain size in the XZ and YZ planes, it is possible to see that the ratios are in a neighborhood of 0.5 in all three outer portions considered, while the ratios are at the inner and central portions around a value of 1. This means that the behavior in the entire tube is similar, both considering the different layers and different cross-sections.

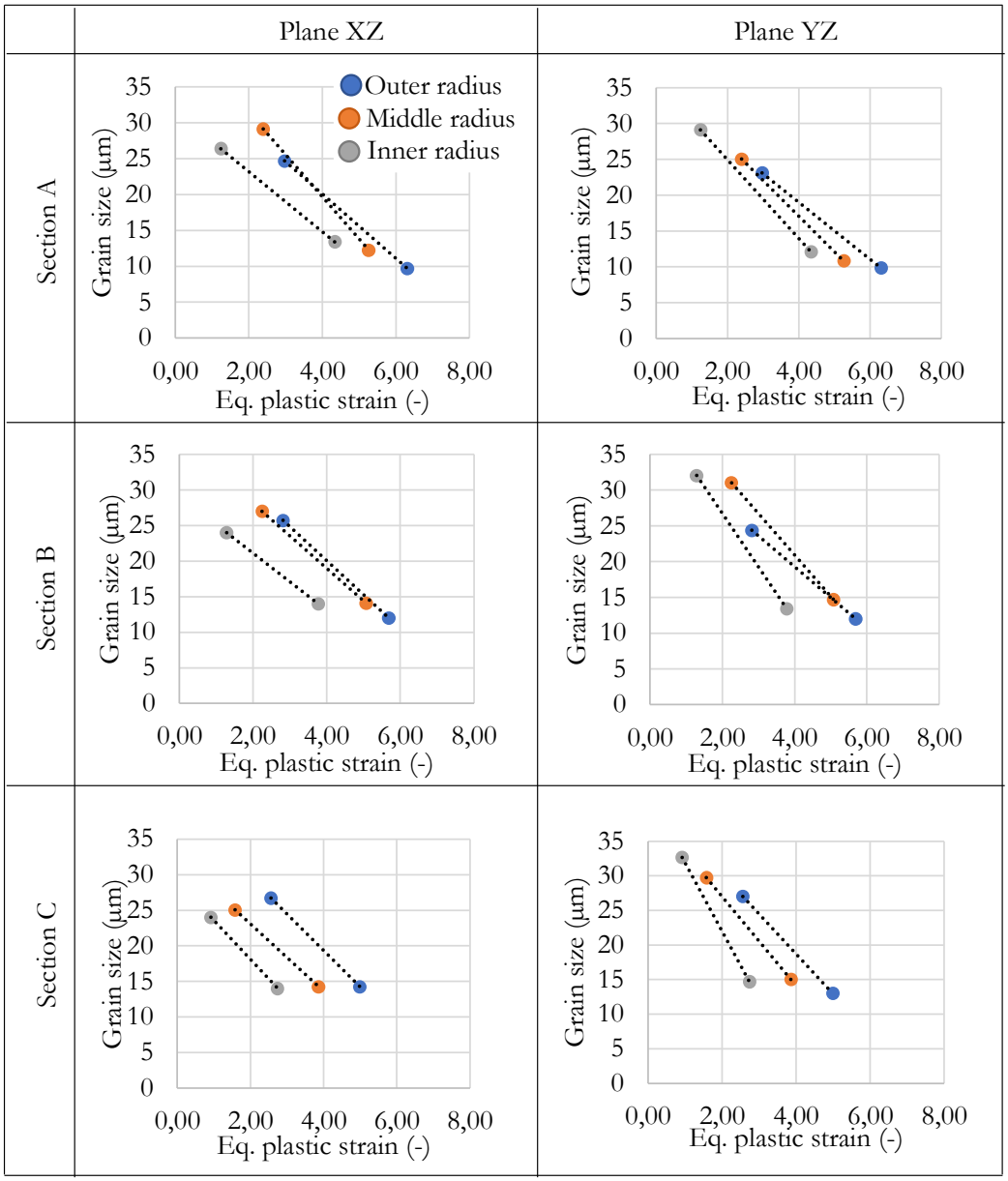

Fig. 7.35 *- Eq. plastic strain vs. Grain size considering Section A, B, and C and planes XZ and YZ.*

7.3.3 Microhardness vs. Grain size

The graphs in Fig. 7.36 show the comparison between the microhardness values and the square root of the grain size obtained using the traditional backward tube flowforming process, considering results before the saturation phenomenon that occurs after a thickness reduction equal to 30%. Analysing the slopes of the trend lines, it is possible to observe that, accordingly with the Hall-Petch relationship, a linear relationship between the inverse of the grain size and the microhardness is established. The trend lines maintain a similar value even as the distance from the constrained portion is the same. Regarding the analysis of the various radial positions, there is

generally a greater slope in correspondence with the central radius, while in the internal and external portions of the tube, the slope is smaller, regardless of the plane considered. Evaluating the relationship between the XZ and YZ planes, it is possible to see that the slope of the XZ plane is higher than that of the YZ plane.

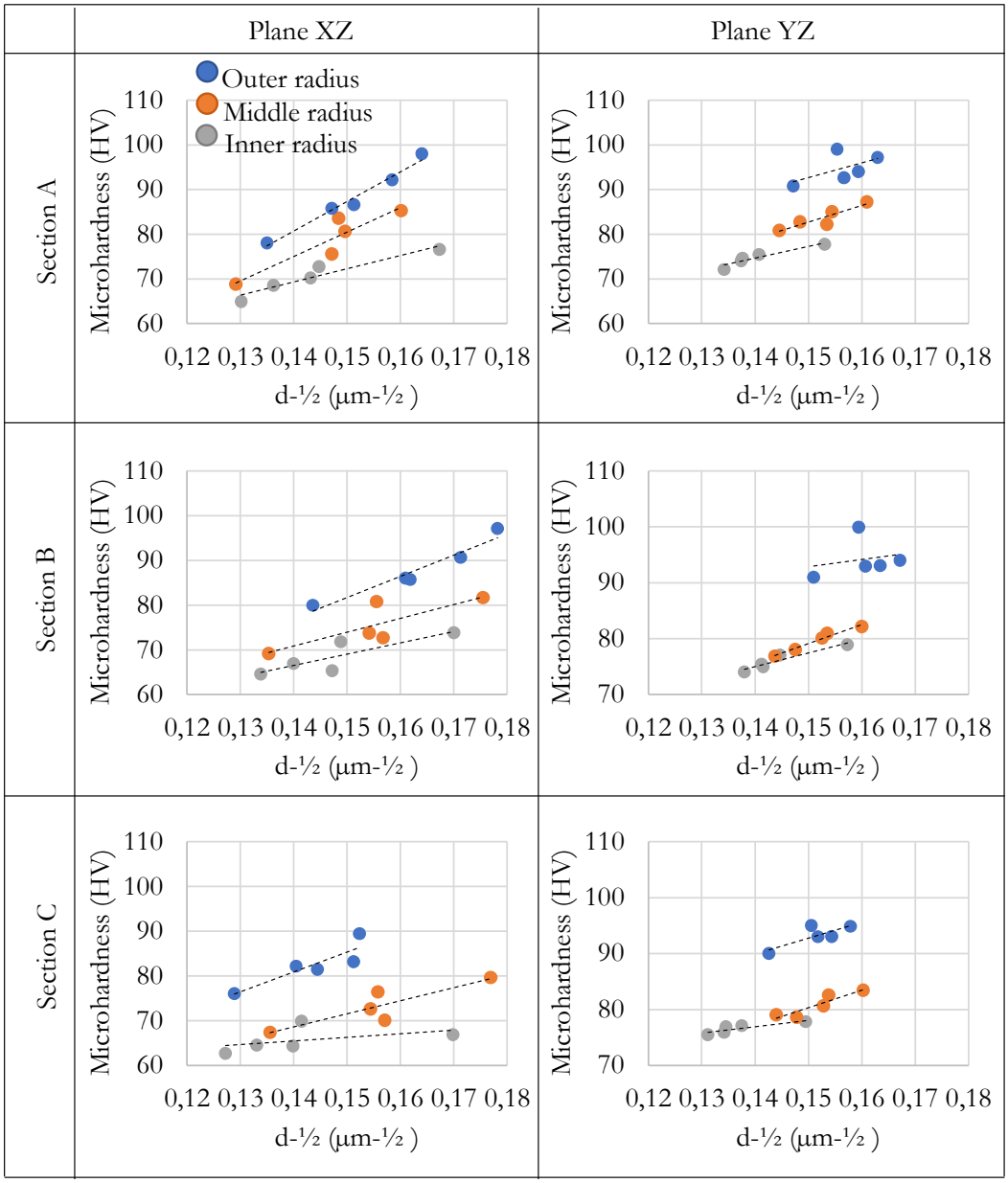

Fig. 7.36 *- Microhardness vs. square root of grain size considering Section A, B, and C and planes XZ and YZ.*

The graphs in Fig. 7.37 compare the microhardness values and the square root of the grain size obtained using the constrained backward tube flowforming process. Analysing the slopes of the trend lines, it is possible to observe that, in this case, accordingly with the Hall-Petch relationship, a linear relationship between the inverse

of the grain size and the microhardness is established. The trend lines maintain a similar value even as the distance from the constrained portion is the same. Regarding the analysis of the various radial positions, there is generally a greater slope in correspondence with the internal and central radius, while in the external portions of the tube, the slope is smaller, regardless of the plane considered. This means that the decrease in the grain size is not linked with a proportional increase in microhardness.

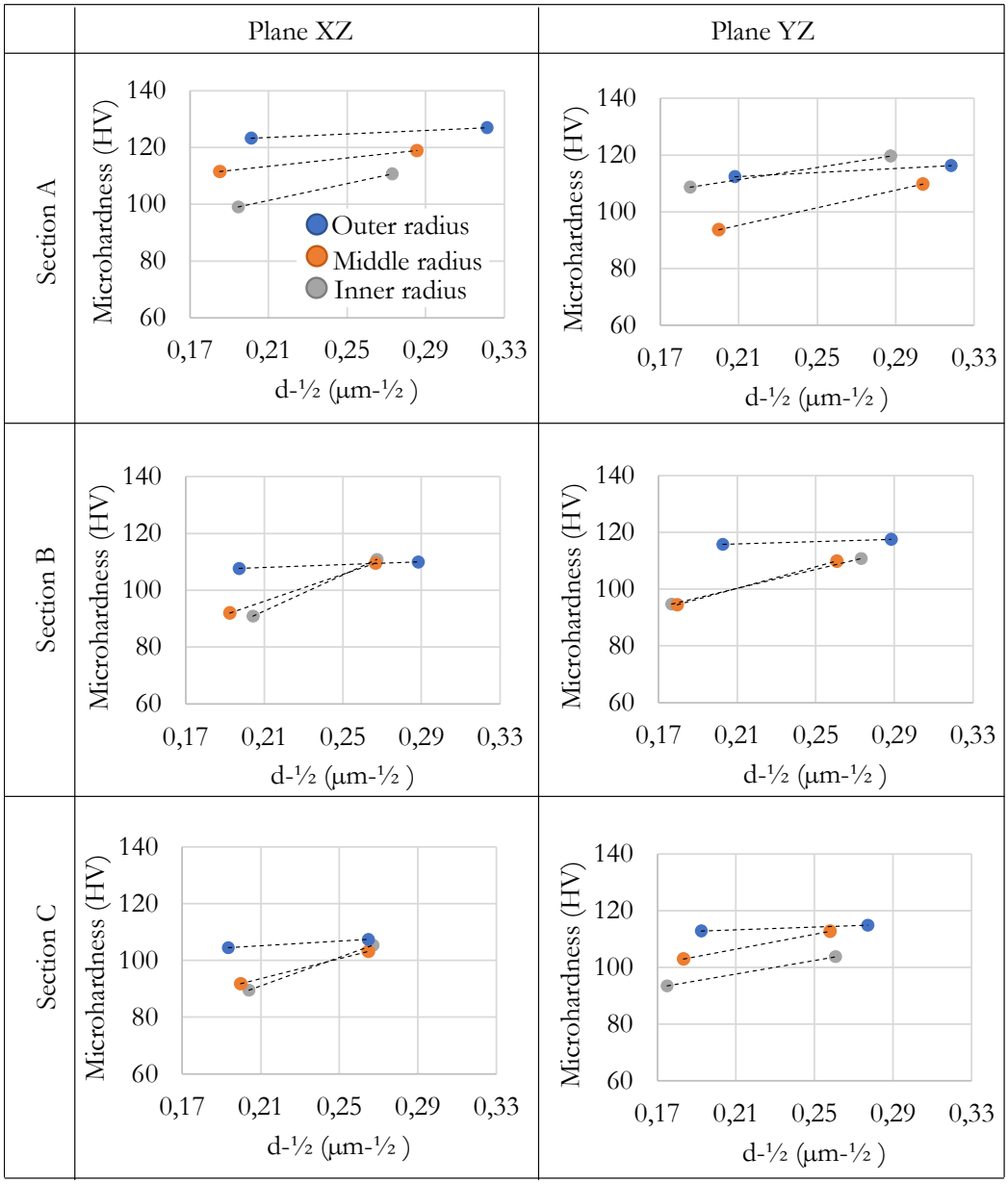

Fig. 7.37 *- Microhardness vs. square root of grain size considering Section A, B, and C and planes XZ and YZ.*

7.3.4 Strain vs. Mechanical characteristics

The graph in Fig. 7.38 shows the comparison between the different mechanical

quantities obtained through tensile tests (yield stress, UTS, and elongation at fracture) and the equivalent plastic strain, calculated through numerical simulations, considering results before the saturation phenomenon that occurs after a thickness reduction equal to 30%, using the traditional solution. Unlike the previous comparisons, in this case, it was decided to use an average strain value for each thickness reduction performed since the comparison is not local but global. The graph shows how the trend of yield stress and UTS is almost the same, while that of the elongation is inverse with respect to these two. As the deformation impressed on the piece increases, yield stress and UTS increase, but the elongation to failure decreases, following the expected theoretical results.

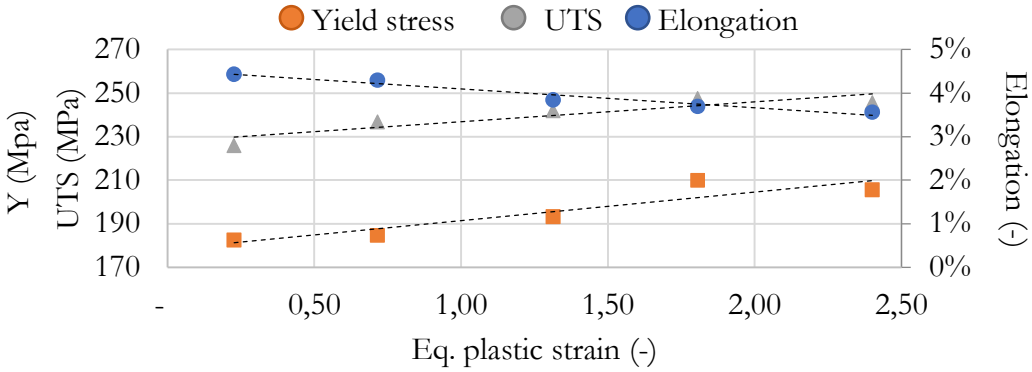

Fig. 7.38 *- Equivalent plastic strain vs. Mechanical characteristics.*

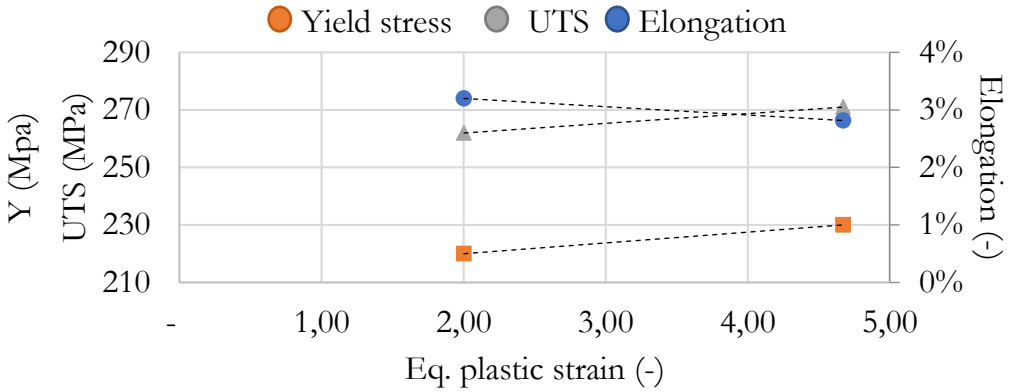

Fig. 7.39 *- Equivalent plastic strain vs. Mechanical characteristics.*

The graph in Fig. 7.39 compares the mechanical quantities obtained through tensile tests (yield stress, UTS and elongation at fracture) and the equivalent plastic strain, calculated through numerical simulations. The graph shows how the trend of yield stress and UTS is almost the same, while that of the elongation is inverse with respect to these two. As the deformation impressed on the piece increases, yield stress and UTS increase, but the elongation to failure decreases according to the expected theoretical results.

Part 4: Conclusions

Chapter 8

Conclusions

This Thesis describes the activities carried out to develop an innovative process chain, which allows obtaining tubes and panels with tailored properties, exploiting materials key characteristics, such as strength, thickness, corrosion protection, and material type, in specific areas of interest of the component, removing the weight where not necessary for performance purposes. Through the considerable refinement of the crystalline grain resulting from the high plastic deformation to which the component is subjected during Severe Plastic Deformation processes, not only does the resistance of the material increase, but it also decreases the presence of internal defects and consequently increases the fatigue resistance. To this aim, two different processes were designed and developed: the traditional backward tube flowforming and a modified version with a radial constraint. These processes were developed in response to lacks highlighted by reviewing the scientific and technical literature to obtain larger dimensions for the tubular components obtained through SPD processes. Although traditionally the tube flowforming process is not catalogued as SPD techniques, it is possible to recognize in them a high refinement of the grain caused by the high plastic deformation generated by the action of the rollers on the tubular element.

The geometrical and kinematic optimizations of the flowforming equipment were performed using FE models developed using the Forge™ software; numerical simulations made it possible to understand the mechanics of deformation, demonstrating the existence of different stress-strain states in different portions of the tube, with both radial gradients and axial directions. This made it possible to establish the feasibility of obtaining tailored components through the backward tube flowforming process. In addition to this result, numerical simulations allow evaluating the feasibility of the process, estimating the load required to perform the deformation

as a function of the thickness reduction imposed during each step of the incremental process. Using an incremental routine made it possible to reduce the loads required to perform the process, allowing several steps to achieve greater deformations, and consequently a higher grain refinement.

The results of the numerical simulations, designed and produced the components necessary to perform the processes, were validated through various geometrical tests, evaluating the results in terms of elongation, tube external and internal diameters, presence or absence of surface defects, using a CMM machine to perform measures. The mechanical properties were evaluated with different tests (microhardness, tensile test, microstructure analysis), both by comparing the values obtained with the starting values and by correlating the experimental results with the numerical ones. From the various tests carried out, a gradient of mechanical properties was noted between the internal and external portions of the tube due to the different deformation states imposed by the mechanics of the process, accordingly with the numerical results. The outer portion of the tube undergoes an increase in the microhardness values concerning the inner and less deformed portion.

However, considering the traditional backward tube flowforming process, a saturation phenomenon typical of SPD processes has been analysed, which does not allow to further increase the mechanical properties in terms of maximum value, even if increasing the deformation imposed through an incremental routine. By analysing the microhardness values according to a radial and an axial pattern, it was possible to understand that while increasing the deformation imposed in the piece by reducing the thickness, the maximum microhardness value is not increased, but the mechanical characteristic is homogenized. Analysing the microstructure, the same gradient was found, linearly correlating the increase in microhardness with the decrease in grain size. From an analysis of the microstructure, it was also possible to observe that the outermost portion of the tube is characterized by a highly refined material with a grain size typical of SPD processes and a high anisotropy value in the grain shape moving from the external to the internal part of the tube. This last result could be used by exploiting the different corrosion resistance characteristics dependent on the grain size (the smaller the crystalline grain, the more corrosion resistant the material). The tensile tests made it possible to evaluate the variations in the mechanical properties and demonstrate an increase in the yield stress and UTS values and a decrease in the material's ductility due to the tube hardening.

The use of an innovative setup, with the use of a radial constraint, has made it possible to achieve a double result: firstly, the build-up defect, typical of the tube flowforming process, has been minimized (Fig. 8.1b), secondly a deformation state has been reached higher, with a more significant increase in the mechanical properties of the material and a higher grain refinement. In addition, this solution allows obtaining better solutions on a geometric level due to the vibration caused by the process that is dampened by the various components of the setup. In particular, the roundness of the

tube is much lower than the traditional solution due to the fixed position of the rollers and the presence of the radial constraint. This result can be exploited to obtain tubes or panels of variable thickness, using interpenetrations of the rollers which vary according to the thickness to be obtained.

Considering the entire tube, the microhardness increases from 60.9±1.5 HV to an average value of 85.7 HV, equivalent to +41%, using the traditional backward tube flowforming, while using the constrained solution the microhardness increases from 60.9±1.5 HV to an average value of 112.6 HV, equivalent to +85%. Considering the microstructure evolution, the grain size decreases from 70±17 μm to an average value of 36±10 μm, equivalent to -48%, using the traditional setup, while the innovative solution guarantees a higher grain refinement, not having the saturation behaviour typical of the traditional setup. The average grain size is equal to 13±7 μm, with a decrease of -80% with respect to the as-delivered conditions.

Regarding the tensile test results, considering the larger/smaller values obtained using the traditional solution, the results show an increase up to 35 MPa (+20%) in the value of the yield stress and a reduction of 76% in terms of maximum elongation at fracture. Regarding the UTS values, if compared with the as-delivered values, there is an absolute increment of +48 MPa, corresponding to a percentage increment of +24%. Considering the constrained solution, the results show an increase up to 55 MPa (+31%) in the value of the yield stress and a reduction of 81% in terms of maximum elongation at fracture. Regarding the UTS values, if compared with the as-delivered values, there is an absolute increment of +71 MPa, corresponding to a percentage increment of +36%.

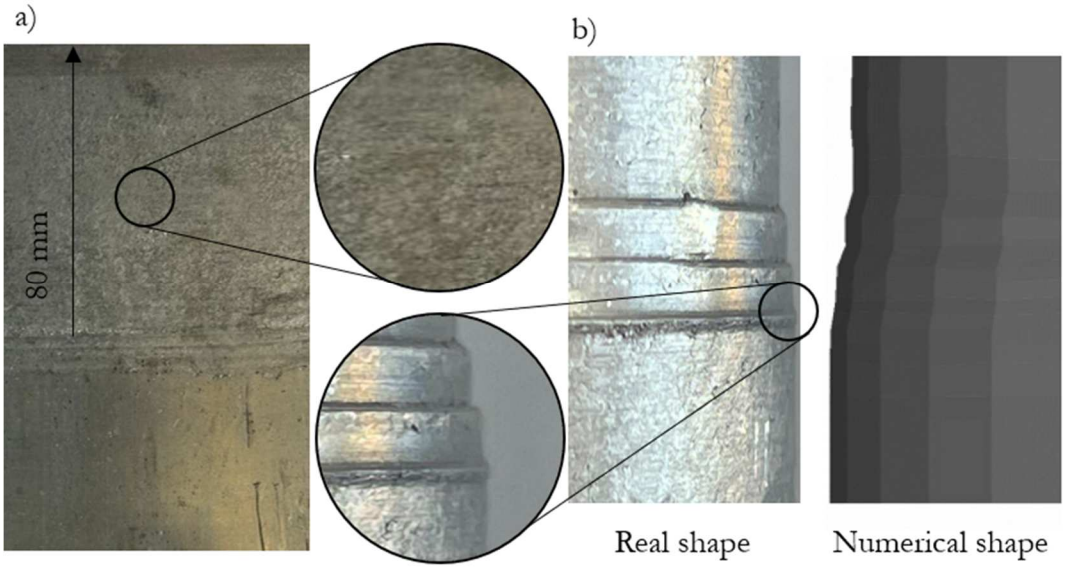

Fig. 8.1 *- a) Panel obtained after the straightening process and b) Comparison between real and numerical shape using constrained setup.*

Focusing on the operations necessary to execute the entire process chain, described in the Introduction of this Thesis, the cutting and straightening operations were performed after the flowforming processes. It is possible to notice in Fig. 8.1a how the cutting and the straightening operations do not create cracks or other defects on the tube surface, making it possible to obtain tailored plate components. From a microhardness point of view, no difference between the flowformed tube and the panel was noted, considering both the internal and external surfaces. While analysing the microstructure, the straightening operation did not affect the grain shape and size due to the constant thickness maintained through the final steps of the process chain. The possibility of obtaining flat elements from tubular elements was therefore demonstrated, guaranteeing the production of both tailored tubes and tailored panels.

All tests were carried out using AA6082-T4 alloy; however, the approach was material-independent: future activities will have to analyse the results obtained from this process chain using aluminium alloys and other alloys such as zinc or magnesium alloys by varying the interpenetration of the rollers and the deformation imposed, starting from microstructures characterized by grain sizes around the micrometre, to evaluate refinements below the micrometric scale. Furthermore, other characterization tests must be carried out on the flowformed component, both tubular and flat, to verify its formability and workability. Preliminary studies [129] carried out using pure zinc (Zn-99.99%) have shown a remarkable refinement of an order of magnitude of the grain size, with the reduction from about 300 μm to 10 μm, while in the outer portion of the tube after a thickness reduction of 6% a layer of 250 μm of ultrafine grains was obtained. The initial high presence of internal porosity caused by inclusions and casting defects of this material usually used to perform galvanizing operations has been significantly reduced with the action of the rollers, however reducing the possibility of performing multiple operations on the same tube. Despite this, a reduction in thickness of 6% made it possible to obtain an average increase of about 30% of the microhardness, with increases of up to more than 50% in correspondence with the outermost layer.

Appendix

Exploded-view drawings

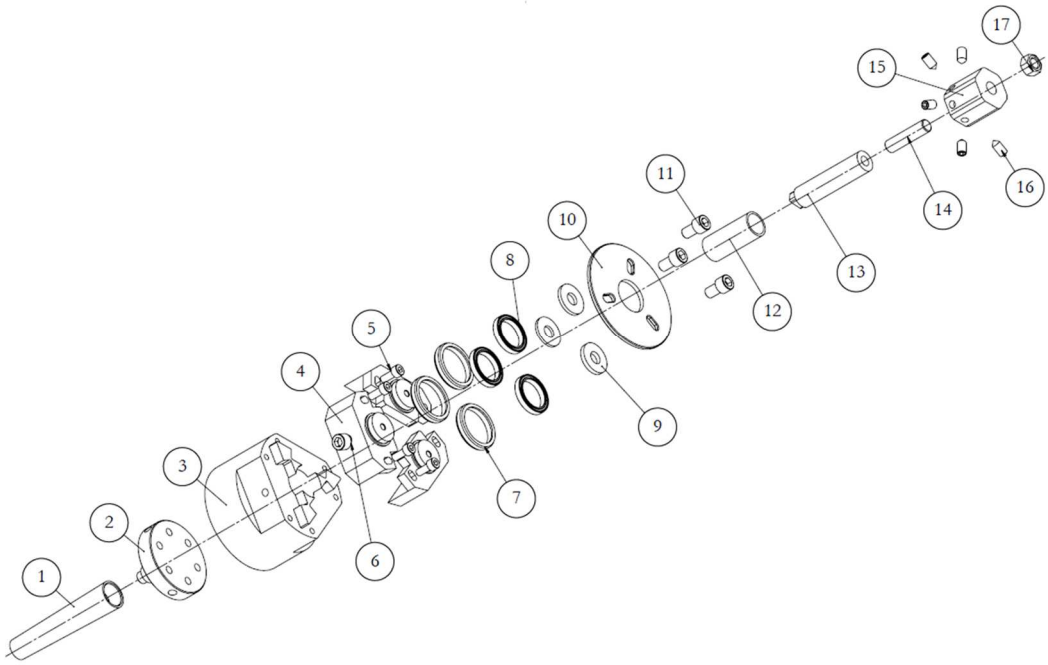

Fig. 1 *- Exploded-view of the traditional backward tube flowforming setup.*

Tab. 1 *- Code and description of the exploded-view of the traditional setup.*

Code	Description
1	Morse taper shank
2	Morse taper shank connection
3	Roller shaft base
4	Roller shafts
5	Screw
6	Screw
7	Roller
8	Roller bearings
9	Gauged width
10	Stiffening element
11	Screw
12	Tube
13	Tube mandrel
14	Threaded bar
15	Tube clamping
16	Fastener
17	Bolt

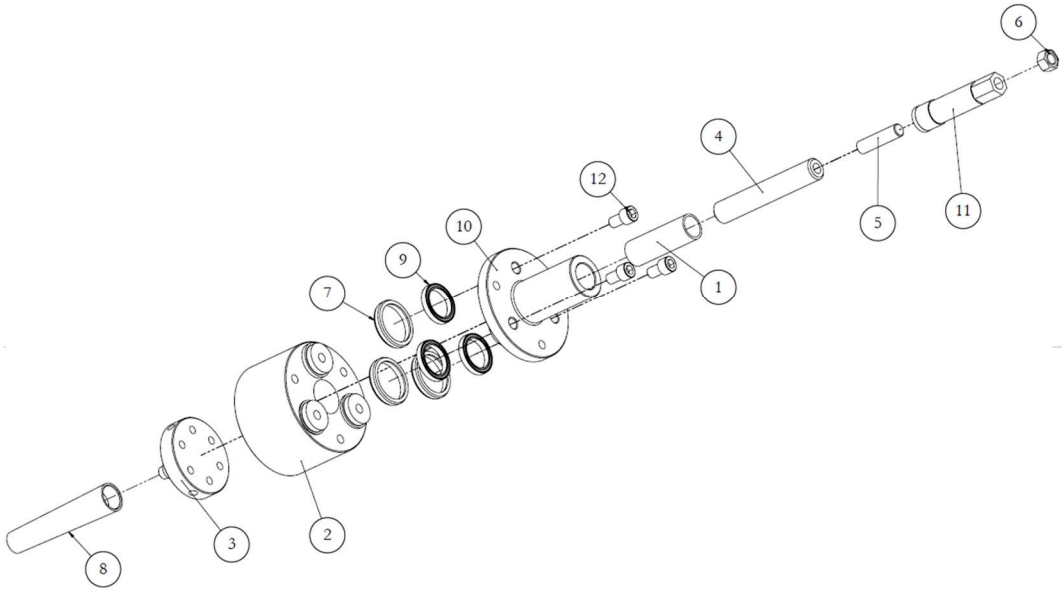

Fig. 2 *- Exploded-view of the constrained backward tube flowforming setup.*

Tab. 2 *- Code and description of the exploded-view of the constrained setup.*

Code	Description
1	Tube
2	Roller's shafts
3	Morse taper shank connection
4	Tube mandrel
5	Threaded bar
6	Bolt
7	Roller
8	Morse taper shank
9	Roller bearings
10	Radial constraint
11	Tube clamping
12	Screw

Equivalent plastic strain

- *Traditional backward tube flowforming*

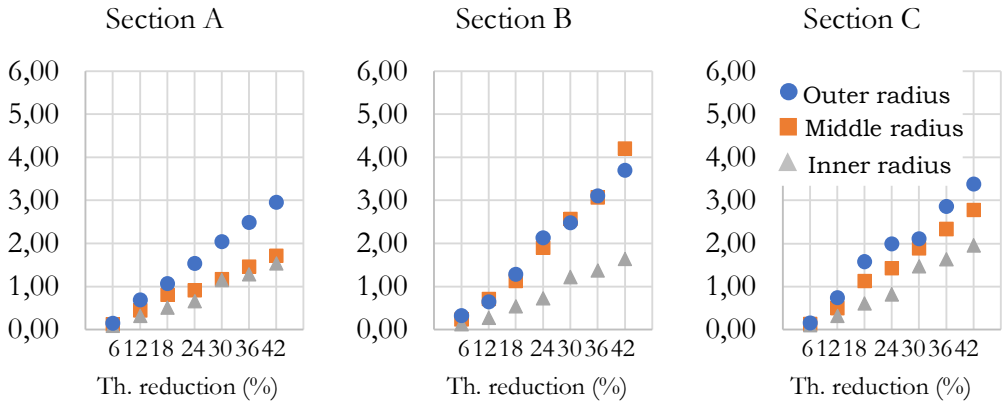

Fig. 3 *- Eq. plastic strain ω=240 rpm, f=2.0 mm/s.*

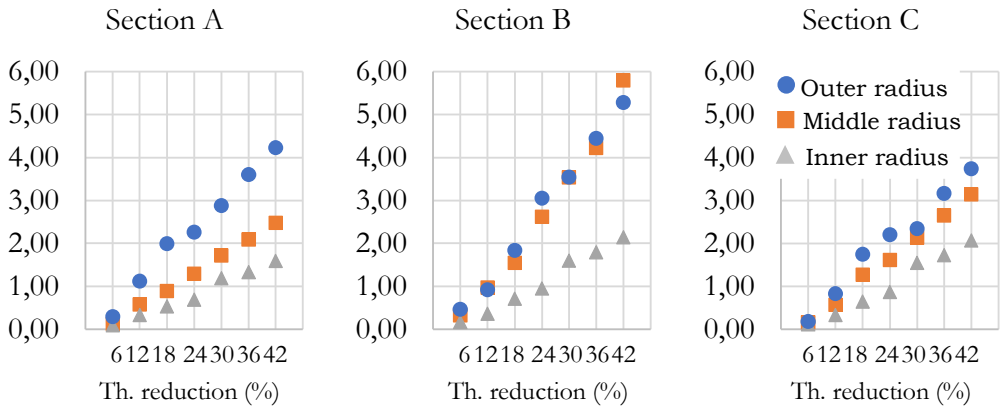

Fig. 4 *- Eq. plastic strain ω=420 rpm, f=1.0 mm/s.*

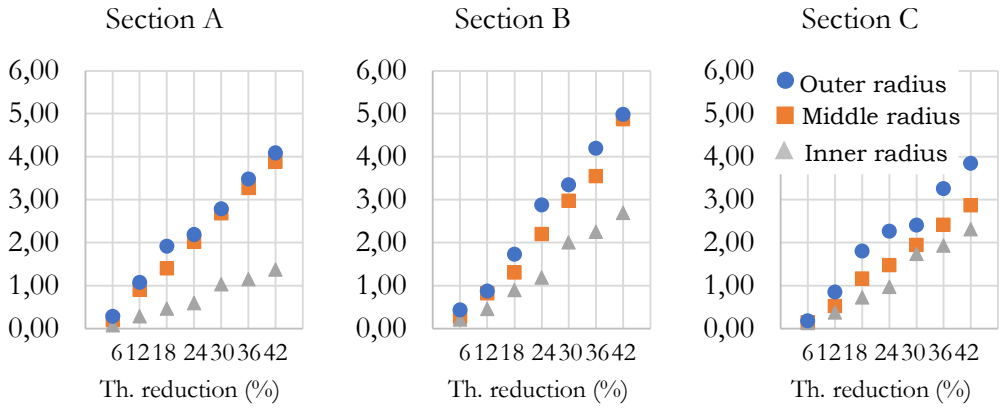

Fig. 5 *- Eq. plastic strain ω=420 rpm, f=1.5 mm/s.*

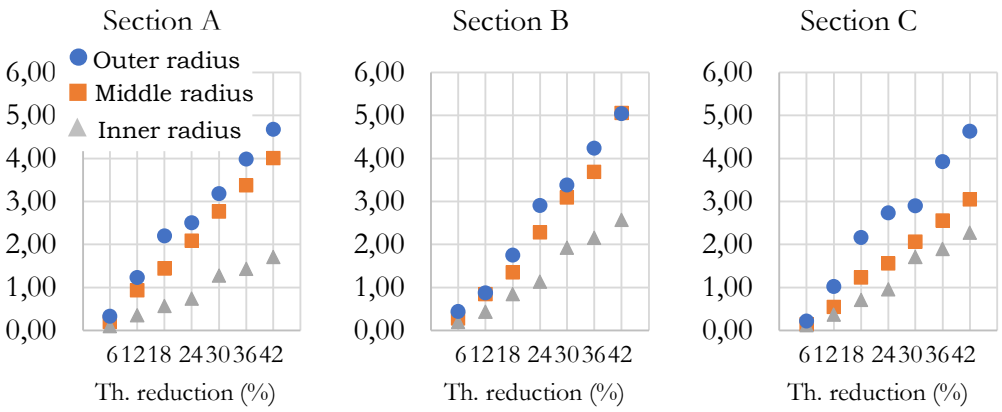

Fig. 6 *- Eq. plastic strain ω=600 rpm, f=2.0 mm/s.*

- *Constrained backward tube flowforming*

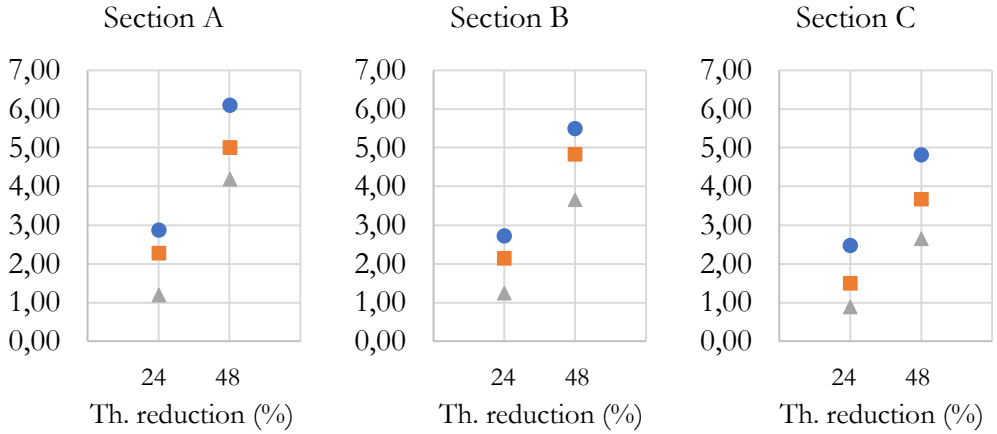

Fig. 7 *- Eq. plastic strain ω=240 rpm, f=1.5 mm/s.*

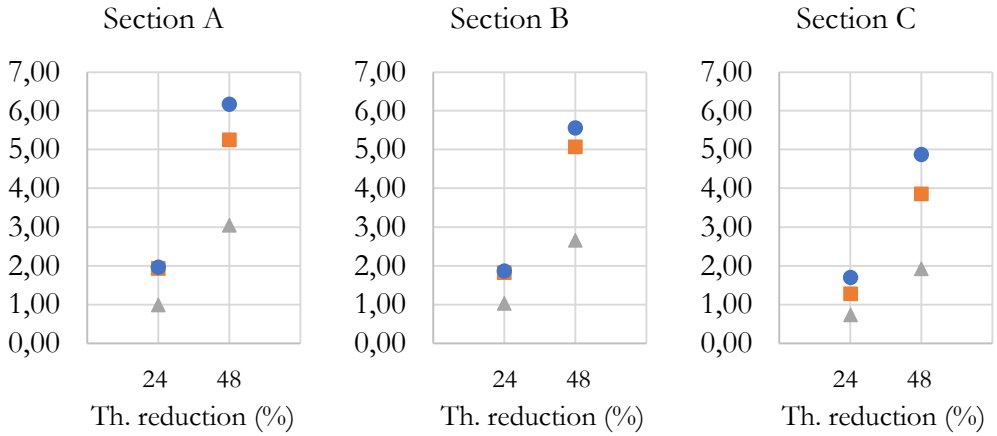

Fig. 8 *- Eq. plastic strain ω=420 rpm, f=1.0 mm/s.*

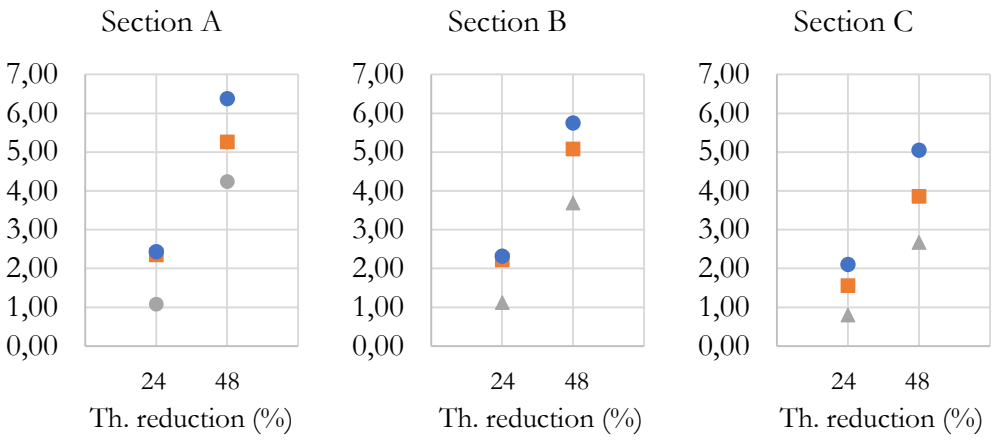

Fig. 9 *- Eq. plastic strain ω=420 rpm, f=2.0 mm/s.*

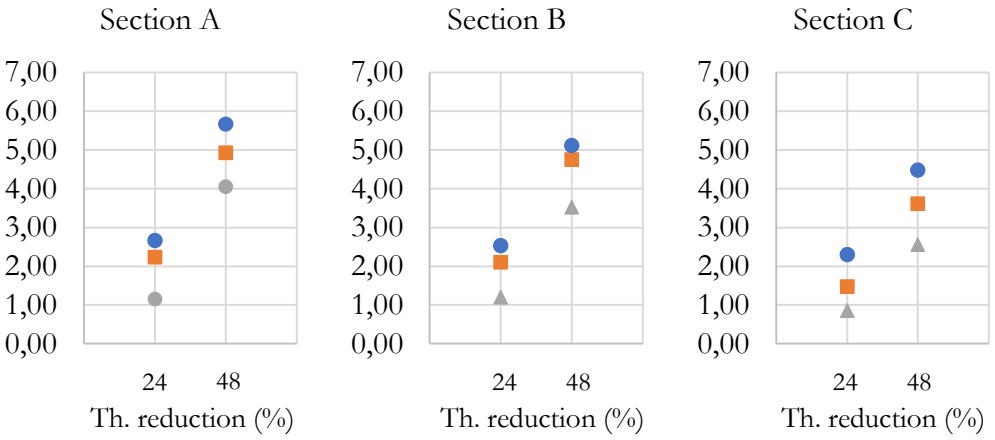

Fig. 10 *- Eq. plastic strain ω=600 rpm, f=1.5 mm/s.*

Microhardness

- *Traditional backward tube flowforming*

***Tab. 3** - Microhardness increment ω=240 rpm, f=1.5 mm/s.*

		XZ plane			YZ plane		
Th. red.	**Section**	**Inner**	**Middle**	**Outer**	**Inner**	**Middle**	**Outer**
6%	A	6%	13%	28%	17%	36%	48%
	B	5%	13%	26%	7%	15%	34%
	C	6%	12%	32%	3%	12%	27%
12%	A	12%	25%	40%	20%	39%	51%
	B	8%	21%	34%	11%	23%	44%
	C	12%	23%	46%	7%	15%	37%
18%	A	15%	33%	41%	21%	39%	53%
	B	9%	27%	35%	12%	25%	44%
	C	11%	18%	44%	10%	20%	36%
24%	A	19%	38%	50%	22%	44%	58%
	B	14%	32%	41%	21%	35%	52%
	C	29%	30%	48%	17%	28%	39%
30%	A	25%	41%	59%	25%	48%	61%
	B	17%	34%	50%	24%	37%	64%
	C	20%	36%	61%	26%	43%	60%
36%	A	27%	43%	61%	27%	47%	60%
	B	19%	35%	52%	26%	38%	61%
	C	21%	37%	63%	24%	40%	52%
42%	A	27%	41%	57%	27%	48%	61%
	B	18%	34%	48%	26%	37%	57%
	C	21%	36%	59%	27%	42%	57%

***Tab. 4** - Microhardness increment ω=420 rpm, f=1.0 mm/s.*

		XZ plane			YZ plane		
Th. red.	**Section**	**Inner**	**Middle**	**Outer**	**Inner**	**Middle**	**Outer**
6%	A	7%	14%	18%	5%	16%	19%
	B	3%	6%	12%	2%	7%	13%
	C	1%	5%	10%	1%	5%	10%
12%	A	8%	16%	19%	6%	18%	20%
	B	5%	10%	16%	4%	11%	17%
	C	3%	9%	13%	2%	10%	15%
18%	A	8%	15%	19%	7%	17%	21%
	B	5%	11%	16%	4%	12%	17%
	C	3%	7%	13%	2%	8%	14%
24%	A	9%	17%	21%	7%	19%	23%
	B	9%	15%	19%	7%	16%	20%
	C	7%	12%	14%	6%	13%	15%
30%	A	10%	19%	22%	8%	21%	24%
	B	11%	15%	23%	9%	17%	25%

	C	10%	16%	20%	8%	18%	22%
36%	A	10%	19%	23%	8%	21%	25%
	B	11%	16%	24%	9%	18%	25%
	C	5%	14%	19%	4%	16%	20%
42%	A	11%	19%	23%	9%	22%	25%
	B	11%	15%	22%	9%	17%	24%
	C	5%	14%	17%	4%	15%	19%

Tab. 5 *- Microhardness increment ω=420 rpm, f=1.5 mm/s.*

		XZ plane			YZ plane		
Th. red.	**Section**	**Inner**	**Middle**	**Outer**	**Inner**	**Middle**	**Outer**
6%	A	11%	20%	30%	8%	18%	27%
	B	3%	8%	19%	5%	8%	21%
	C	2%	7%	16%	2%	6%	15%
12%	A	13%	22%	32%	9%	19%	29%
	B	6%	12%	24%	8%	13%	27%
	C	5%	12%	23%	3%	11%	21%
18%	A	13%	21%	33%	9%	19%	30%
	B	6%	13%	25%	9%	15%	27%
	C	5%	9%	22%	3%	8%	20%
24%	A	14%	24%	36%	10%	22%	33%
	B	10%	18%	29%	15%	20%	32%
	C	12%	16%	24%	8%	14%	22%
30%	A	16%	26%	38%	19%	24%	37%
	B	12%	19%	35%	18%	21%	39%
	C	16%	22%	34%	11%	20%	31%
36%	A	17%	26%	39%	12%	23%	35%
	B	13%	20%	36%	19%	22%	40%
	C	9%	20%	32%	6%	18%	29%
42%	A	17%	27%	39%	12%	24%	36%
	B	13%	19%	34%	19%	21%	38%
	C	9%	19%	30%	6%	17%	27%

Tab. 6 *- Microhardness increment ω=420 rpm, f=2.0 mm/s.*

		XZ plane			YZ plane		
Th. red.	**Section**	**Inner**	**Middle**	**Outer**	**Inner**	**Middle**	**Outer**
6%	A	7%	13%	28%	18%	33%	49%
	B	6%	14%	31%	8%	14%	34%
	C	3%	11%	25%	4%	11%	27%
12%	A	13%	24%	41%	22%	36%	52%
	B	10%	21%	41%	14%	22%	44%
	C	6%	19%	35%	8%	20%	38%
18%	A	15%	32%	42%	23%	35%	54%
	B	7%	19%	41%	15%	24%	45%
	C	6%	15%	34%	8%	15%	36%
24%	A	19%	37%	51%	24%	40%	60%

	B	18%	33%	49%	25%	33%	53%
	C	15%	26%	37%	21%	26%	40%
30%	A	26%	40%	61%	28%	43%	63%
	B	21%	34%	60%	30%	35%	64%
	C	10%	31%	47%	28%	37%	56%
36%	A	28%	41%	63%	29%	43%	64%
	B	23%	35%	61%	32%	36%	66%
	C	11%	32%	48%	15%	33%	52%
42%	A	27%	40%	59%	30%	44%	64%
	B	23%	34%	57%	32%	35%	62%
	C	10%	31%	45%	14%	31%	49%

***Tab. 7** - Microhardness increment ω=600 rpm, f=2.0 mm/s.*

		XZ plane			YZ plane		
Th. red.	**Section**	**Inner**	**Middle**	**Outer**	**Inner**	**Middle**	**Outer**
6%	A	10%	21%	41%	18%	34%	49%
	B	15%	26%	37%	8%	14%	34%
	C	4%	12%	29%	4%	11%	27%
12%	A	6%	19%	35%	21%	38%	51%
	B	26%	40%	61%	13%	22%	44%
	C	9%	21%	40%	8%	17%	38%
18%	A	15%	32%	42%	23%	35%	54%
	B	21%	34%	60%	14%	25%	44%
	C	8%	16%	39%	9%	18%	36%
24%	A	7%	19%	41%	23%	42%	59%
	B	10%	31%	47%	23%	34%	53%
	C	22%	28%	42%	19%	27%	39%
30%	A	6%	15%	34%	26%	45%	62%
	B	19%	34%	55%	27%	36%	64%
	C	15%	33%	54%	22%	28%	58%
36%	A	19%	37%	51%	24%	40%	60%
	B	21%	35%	56%	29%	37%	63%
	C	16%	35%	56%	19%	36%	52%
42%	A	18%	33%	49%	28%	46%	63%
	B	20%	34%	53%	29%	36%	59%
	C	16%	33%	52%	21%	37%	53%

Grain size

- *Traditional backward tube flowforming*

***Tab. 8** - Grain size decrement ω=240 rpm, f=1.5 mm/s.*

		XZ plane			YZ plane		
Th. red.	**Section**	**Inner**	**Middle**	**Outer**	**Inner**	**Middle**	**Outer**
6%	A	-17%	-18%	-29%	-23%	-33%	-50%
	B	-18%	-16%	-20%	-24%	-29%	-37%
	C	-17%	-18%	-27%	-20%	-29%	-31%
12%	A	-25%	-42%	-46%	-27%	-37%	-62%
	B	-26%	-38%	-31%	-28%	-32%	-45%
	C	-24%	-42%	-43%	-24%	-32%	-38%
18%	A	-33%	-45%	-51%	-27%	-41%	-64%
	B	9%	27%	-34%	-28%	-36%	-47%
	C	-32%	-45%	-47%	-24%	-36%	-40%
24%	A	-34%	-44%	-58%	-31%	-42%	-68%
	B	-36%	-39%	-39%	-32%	-37%	-50%
	C	-33%	-43%	-54%	-27%	-37%	-42%
30%	A	-53%	-55%	-64%	-43%	-47%	-60%
	B	-55%	-49%	-43%	-45%	-41%	-44%
	C	-51%	-55%	-59%	-34%	-41%	-44%
36%	A	-53%	-62%	-65%	-44%	-50%	-69%
	B	-55%	-55%	-44%	-45%	-44%	-51%
	C	-51%	-61%	-61%	-39%	-44%	-43%
42%	A	-51%	-57%	-57%	-29%	-50%	-65%
	B	-53%	-51%	-38%	-30%	-44%	-48%
	C	-49%	-57%	-53%	-26%	-44%	-40%

***Tab. 9** - Grain size decrement ω=420 rpm, f=1.0 mm/s.*

		XZ plane			YZ plane		
Th. red.	**Section**	**Inner**	**Middle**	**Outer**	**Inner**	**Middle**	**Outer**
6%	A	-8%	-9%	-14%	-15%	-23%	-26%
	B	-9%	-8%	-15%	-9%	-19%	-25%
	C	-7%	-7%	-14%	-11%	-16%	-25%
12%	A	-11%	-20%	-21%	-18%	-26%	-32%
	B	-13%	-19%	-23%	-10%	-21%	-30%
	C	-11%	-17%	-22%	-12%	-18%	-30%
18%	A	-15%	-22%	-23%	-18%	-29%	-34%
	B	-17%	-21%	-25%	-10%	-24%	-32%
	C	-14%	-18%	-25%	-13%	-20%	-32%
24%	A	-16%	-21%	-27%	-21%	-29%	-36%
	B	-17%	-20%	-29%	-12%	-24%	-34%
	C	-15%	-17%	-28%	-14%	-20%	-34%
30%	A	-24%	-27%	-29%	-29%	-33%	-32%
	B	-27%	-25%	-32%	-16%	-27%	-30%

	C	-23%	-22%	-31%	-20%	-22%	-30%
36%	A	-24%	-30%	-30%	-29%	-35%	-36%
	B	-27%	-28%	-32%	-16%	-28%	-34%
	C	-23%	-24%	-31%	-20%	-24%	-34%
42%	A	-23%	-28%	-26%	-19%	-35%	-34%
	B	-26%	-26%	-28%	-11%	-29%	-32%
	C	-22%	-23%	-27%	-13%	-24%	-32%

Tab. 10 *- Grain size decrement ω=420 rpm, f=1.5 mm/s.*

		XZ plane			YZ plane		
Th. red.	**Section**	**Inner**	**Middle**	**Outer**	**Inner**	**Middle**	**Outer**
6%	A	-11%	-10%	-17%	-19%	-22%	-29%
	B	-12%	-8%	-13%	-17%	-21%	-27%
	C	-12%	-8%	-20%	-16%	-21%	-25%
12%	A	-16%	-23%	-27%	-23%	-24%	-36%
	B	-17%	-19%	-21%	-20%	-23%	-33%
	C	-17%	-20%	-32%	-19%	-24%	-30%
18%	A	-21%	-25%	-30%	-23%	-27%	-38%
	B	-22%	-20%	-23%	-20%	-26%	-34%
	C	-22%	-21%	-35%	-19%	-26%	-32%
24%	A	-23%	-24%	-34%	-26%	-27%	-40%
	B	-24%	-20%	-26%	-23%	-27%	-36%
	C	-24%	-20%	-40%	-22%	-27%	-33%
30%	A	-35%	-30%	-37%	-36%	-31%	-35%
	B	-36%	-25%	-41%	-32%	-30%	-32%
	C	-36%	-26%	-28%	-30%	-30%	-33%
36%	A	-35%	-34%	-38%	-36%	-32%	-40%
	B	-36%	-28%	-29%	-33%	-32%	-37%
	C	-36%	-29%	-45%	-31%	-32%	-34%
42%	A	-33%	-31%	-33%	-24%	-33%	-38%
	B	-35%	-26%	-26%	-22%	-32%	-35%
	C	-35%	-27%	-39%	-20%	-32%	-32%

Tab. 11 *- Grain size decrement ω=420 rpm, f=2.0 mm/s.*

		XZ plane			YZ plane		
Th. red.	**Section**	**Inner**	**Middle**	**Outer**	**Inner**	**Middle**	**Outer**
6%	A	-16%	-14%	-22%	-21%	-32%	-34%
	B	-16%	-17%	-25%	-22%	-31%	-36%
	C	-16%	-18%	-18%	-19%	-31%	-31%
12%	A	-23%	-34%	-34%	-24%	-35%	-42%
	B	-24%	-41%	-40%	-26%	-35%	-45%
	C	-24%	-42%	-28%	-23%	-35%	-38%
18%	A	-30%	-36%	-38%	-25%	-39%	-44%
	B	-31%	-44%	-44%	-27%	-39%	-47%
	C	-31%	-44%	-31%	-23%	-39%	-40%
24%	A	-32%	-35%	-43%	-28%	-40%	-46%

	B	-33%	-43%	-51%	-30%	-40%	-50%
	C	-33%	-43%	-35%	-26%	-40%	-42%
30%	A	-49%	-44%	-47%	-39%	-45%	-41%
	B	-51%	-54%	-55%	-42%	-44%	-44%
	C	-50%	-54%	-38%	-36%	-44%	-37%
36%	A	-49%	-50%	-48%	-39%	-48%	-47%
	B	-50%	-60%	-56%	-43%	-47%	-50%
	C	-50%	-61%	-39%	-36%	-47%	-43%
42%	A	-47%	-46%	-42%	-26%	-48%	-44%
	B	-49%	-55%	-49%	-28%	-47%	-47%
	C	-49%	-56%	-34%	-24%	-47%	-40%

Tab. 12 *- Grain size decrement ω=600 rpm, f=2.0 mm/s.*

		XZ plane			YZ plane		
Th. red.	**Section**	**Inner**	**Middle**	**Outer**	**Inner**	**Middle**	**Outer**
6%	A	-16%	-18%	-21%	-27%	-34%	-39%
	B	-14%	-18%	-23%	-24%	-32%	-50%
	C	-14%	-16%	-22%	-25%	-36%	-44%
12%	A	-23%	-43%	-33%	-32%	-38%	-47%
	B	-21%	-43%	-36%	-28%	-36%	-61%
	C	-20%	-39%	-35%	-29%	-40%	-54%
18%	A	-30%	-46%	-37%	-32%	-42%	-50%
	B	-28%	-45%	-40%	-29%	-40%	-64%
	C	-26%	-41%	-38%	-30%	-45%	-56%
24%	A	-32%	-45%	-42%	-37%	-43%	-52%
	B	-29%	-44%	-46%	-33%	-41%	-67%
	C	-27%	-40%	-44%	-33%	-46%	-59%
30%	A	-49%	-56%	-46%	-51%	-48%	-46%
	B	-45%	-56%	-50%	-46%	-46%	-60%
	C	-42%	-50%	-48%	-47%	-51%	-52%
36%	A	-48%	-63%	-47%	-52%	-51%	-53%
	B	-45%	-62%	-51%	-46%	-49%	-69%
	C	-42%	-56%	-49%	-47%	-55%	-60%
42%	A	-47%	-58%	-41%	-34%	-52%	-50%
	B	-43%	-57%	-45%	-31%	-49%	-64%
	C	-40%	-52%	-43%	-31%	-55%	-57%

List of figures

List of tables

References

[1] E. O. Hall, "The Deformation and Ageing of Mild Steel: III Discussion of Results," *Proceedings of the Physical Society,* vol. 64, no. 9, pp. 747-753, 1951.

[2] R. W. Armstrong, "60 Years of Hall-Petch: Past to Present Nano-Scale Connections," *Materials Transactions,* vol. 55, no. 1, pp. 2-12, 2014.

[3] A. H. Chokshi, A. Rosen, J. Karch and H. Gleiter, "On the validity of the Hall-Petch relationship in nanocrystalline materials," *Scripta Metallurgica,* vol. 23, no. 10, pp. 1679-1683, 1989.

[4] C. S. Pande and K. P. Cooper, "Nanomechanics of Hall-Petch relationship in nanocrystalline materials," *Progress in Materials Science,* vol. 54, pp. 689-706, 2009.

[5] M. A. Meyers, A. Mishra and D. J. Benson, "Mechanical properties of nanocrystalline materials," *Progress in Materials Science,* vol. 51, pp. 427-556, 2006.

[6] R. Z. Valiev, Y. Estrin, Z. Horita, T. G. Langdon, M. J. Zechetbauer and Y. T. Zhu, "Producing Bulk Ultrafine-Grained Materials by Severe Plastic Deformation," *JOM Journal of the Minerals, Metals and Materials Society,* vol. 58, pp. 33-39, 2006.

[7] H. Zahid, A. Awais, M. I. Osama and A.-M. Fahad, "Severe Plastic Deformation and Its Application on Processing Titanium: A Review," *International Journal of Engineering and Technology,* vol. 9, no. 6, pp. 426-431, 2017.

[8] A. Rosochowski, "Processing Metals by Severe Plastic Deformation," *Solid State Phenomena,* Vols. 101-102, pp. 13-22, 2005.

[9] P. Zhang, S. X. Li and Z. F. Zhang, "General relationship between strength and hardness," *Materials Science and Engineering: A,* vol. 529, pp. 62-73, 2011.

[10] A. P. Zhilyaev, A. A. Gimazov and T. G. Langdon, "Recent developments in modelling of microhardness saturation during SPD processing of metals and alloys," *Journal of Materials Science,* vol. 48, pp. 4461-4466, 2013.

[11] J. R. Weertman, "Hall-Petch strengthening in nanocrystalline metals," *Materials Science and Engineering: A,* vol. 166, pp. 161-167, 1993.

[12] R. Z. Valiev, "Strength and Ductility of Nanostructured SPD Metals," *NATO Science Series II: Mathematics, Physics and Chemistry,* vol. 146, pp. 79-90, 2004.

[13] E. N. Borodin, A. Morozova, V. Bratov, A. Belyakov and A. P. Jivkov, "Experimental and numerical analyses of microstructure evolution of Cu-Cr-Zr alloys during severe plastic deformation," *Materials Characterization,* vol. 156, p. 109849, 2019.

[14] I. Sabirov, M. Y. Murashkin and R. Z. Valiev, "Nanostructured aluminium

alloys produced by severe plastic deformation: New horizons in development," *Materials Science and Engineering: A,* vol. 560, pp. 1-24, 2013.

[15] R. Łyszkowski, W. Polkowski and T. Czujko, "Severe Plastic Deformation of Fe-22Al-5Cr Alloy by Cross-Channel Extrusion with Back Pressure," *Materials,* vol. 11, no. 11, pp. 2214-2231, 2018.

[16] A. Azushima, R. Kopp, A. Korhonen, D. Y. Yang, F. Micari, G. D. Lahoti, P. Groche, J. Yanagimoto, N. Tsuji, A. Rosochowski and A. Yanagida, "Severe plastic deformation (SPD) processes for metals," *CIRP Annals,* vol. 57, pp. 716-735, 2008.

[17] G. Faraji and H. Torabzadeh, "An Overview on the Continuous Severe Plastic Deformation Method," *Materials Transaction,* vol. 60, no. 7, pp. 1316-1330, 2019.

[18] M. Furukawa, Z. Horita and T. G. Langdon, "Developing Ultrafine Grain Sizes Using Severe Plastic Deformation," *Adv. Eng. Mater.,* vol. 3, pp. 121-125, 2001.

[19] G. Faraji, H. S. Kim and H. T. Kashi, Severe Plastic Deformation: Methods, Processing and Properties, 1 ed., Elsevier, 2018.

[20] A. P. Zhilyaev, D. L. Swisher, K. Oh-ishi, T. G. Langdon and T. R. McNelley, "Microtexture and microstructure evolution during processing of pure aluminium by repetitive ECAp," *Materials Science and Engineering: A,* vol. 429, pp. 137-148, 2006.

[21] V. M. Segal.USSR Patent 575892, 1977.

[22] V. M. Segal, "Materials processing by simple shear," *Materials Science and Enginnering: A,* vol. 197, pp. 157-164, 1995.

[23] A. Azushima and K. Aoki, "Properties of ultrafine-grained steel by repeated shear deformation of side extrusion process," *Materials Science and Engineering: A,* vol. 337, pp. 45-49, 2002.

[24] R. Z. Valiev and T. G. Langdon, "Principles of equal-channel angular pressing as a processing tool for grain refinement," *Progress in Materials Science,* vol. 51, pp. 881-981, 2006.

[25] J. Huang, Y. T. Zhu, D. J. Alexander, X. Liao, T. C. Lowe and R. J. Araro, "Development of repetitive corrugation and straightening," *Materials Science and Engineering: A,* vol. 371, pp. 35-39, 2004.

[26] P. W. Bridgman, "Effects of High Shearing Stress Combined with High Hydrostatic Pressure," *Physical Review Letters,* vol. 48, pp. 825-847, 1935.

[27] R. Z. Valiev, "Structure and mechanical properties of ultrafine-grained metals," *Materials Science and Engineering: A,* vol. 234, pp. 59-66, 1997.

[28] C. Xu, Z. Horita and T. G. Langdon, "The evolution of homogeneity in processing by high-pressure torsion," *Acta Materialia,* vol. 55, pp. 203-212,

2007.

[29] Y. H. Zhao, Z. Horita, T. G. Langdon and Y. T. Zhu, "Evolution of defect structures during cold rolling of ultrafine-grained Cu and Cu-Zn alloys: Influence of stacking fault energy," *Materials Science and Engineering: A,* vol. 474, pp. 342-347, 2008.

[30] G. Kapoor, Y. Huang, V. S. Sarma, G. T. Langdon and J. Gubicza, "Effect of Mo addition on the microstructure and hardness of ultrafine-grained Ni alloys processed by a combination of cryorolling and high-pressure torsion," *Materials Science and Engineering: A,* vol. 688, pp. 92-100, 2017.

[31] N. Tsuji, Y. Saito, H. Utsonomiya and S. Tanigawa, "Ultra-fine grained bulk steel produced by accumulative roll-bonding (ARB) process," *Scripta Materialia,* vol. 40, 1999.

[32] R. Ma, L. Wang, N. Y. Wang and D. Z. Zhou, "Microstructure and mechanical properties of the AZ31 magnesium alloy sheets processed by asymmetric reduction rolling," *Materials Science and Engineering: A,* vol. 638, pp. 190-196, 2015.

[33] A. Azimi, S. Tutunchilar, G. Faraji and M. K. Besharati Givi, "Mechanical properties and microstructural evolution during multi-pass ECAR of Al 1100-O alloy," *Materials and Design,* vol. 42, pp. 388-394, 2012.

[34] M. Mahmoodi and S. Lohrasbi, "Investigation of residual stresses distribution in equal channel angular rolled aluminum alloy by means of the slitting method," *The Journal of Strain Analysis for Engineering Design,* vol. 52, no. 6, pp. 389-396.

[35] D. H. Shin, J.-J. Park, Y.-S. Kim and K.-T. Park, "Constrained groove pressing and its application to grain refinement of aluminum," *Materials Science and Engineering: A,* vol. 328, pp. 98-103, 2002.

[36] A. K. Gupta, T. S. Maddukuri and S. K. Singh, "Constrained groove pressing for sheet metal processing," *Progress in Materials Science,* vol. 84, pp. 403-462, 2016.

[37] S. S. S. Kumar and T. Raghu, "Mechanical behaviour and microstructural evolution of constrained groove pressing nickel sheets," *Journals of Material Processing Technology,* vol. 213, pp. 214-220, 2013.

[38] F. Djavanroodi, A. A. Zolfaghari, M. Ebrahimi and K. Nikbin, "Route Effect on Equal Channel Angular Pressing of Copper Tube," *Acta Metallurgica Sinica,* vol. 27, pp. 95-100, 2014.

[39] A. Zangiabadi and M. Kazeminezhad, "Development of a novel severe plastic deformation method for tubular materials: Tube Channel Pressing (TCP)," *Materials Science and Engineering: A,* vol. 528, pp. 5066-5072, 2011.

[40] G. Faraji and H. S. Kim, "Review of principles and methods of severe plastic

deformation for producing ultrafine-grained tubes," *Materials Science and Technology,* vol. 33, pp. 905-923, 2016.

[41] E. Bagherpour, N. Pardis, M. Reihanian and R. Ebrahimi, "An overview on severe plastic deformation: research status, techniques classification, microstructure evolution, and applications," *The International Journal of Advanced Manufacturing Technology,* vol. 100, pp. 1647-1694, 2019.

[42] A. V. Nagasekhar, Y. Tick-Hon and K. S. Ramakanth, "Mechanics of single pass equal channel angular extrusion of powder in tubes," *Applied Physics,* vol. 85, pp. 185-194, 2006.

[43] G. Faraji, "Tubular Channel Angular Pressing". Iran Patent 389110832, 12 Feb 2011.

[44] F. Djavanroodi, A. A. Zolfaghari and M. Ebrahimi, "Experimental investigation of three different tube equal channel angular pressing techniques," *Metallic Materials,* vol. 63, pp. 27-34, 2015.

[45] D. M. Jafarlou, E. Zalnezhad, M. A. Hassan, M. A. Ezazi, N. A. Mardi, A. M. S. Hamouda, M. Hamdi and G. H. Yoon, "Severe plastic deformation of tubular AA 6061 via equal channel angular pressing," vol. 90, pp. 1124-1135, 2016.

[46] F. Djavanroodi, A. A. Zolfaghari, M. Ebrahimi and K. M. Nikbin, "Equal Channel Angular Pressing of Tubular Samples," *Acta MEtallurgica Sinica,* vol. 26, no. 5, pp. 574-580, 2013.

[47] G. Faraji, M. M. Mashhadi and H. S. Kim, "Tubular channel angular pressing (TCAP) as a novel severe plastic deformation method for cylindrical tubes," *Materials Letters,* vol. 65, pp. 3009-3012, 2011.

[48] M. Ebrahimi, C. Gode, S. Attarilar and R. Berjis, "Concurrent Enhancement of Strength and Corrosion Resistance in Ultrafine-grained Al6083 Tubes," *Transactions of the Indian Institute of Metals ,* vol. 74, pp. 753-766, 2021.

[49] A. Srivastava, M. W. Vaughan, B. Mansoor, W. Nasim, R. E. Barber, I. Karaman and K. T. Hartwig, "Tube equal channel angular extrusion (TECAE) of Mg-3Al-1Zn alloy," *Materials Science and Engineering: A,* vol. 814, p. 141236, 2021.

[50] J. Zhang, W. Han, W. Rui, J. Li, Z. Huang and F. Sui, "Deformation Mechanisms of 316L Austenitic Stainless Steel Tubes under Equal CHannel Angular Pressing," *Journal of Materials Engineering and Performance,* vol. 29, pp. 1253-1261, 2020.

[51] R. Neugebauer, M. Kolbe and R. Glass, "New warm forming processes to produce hollow shafts," *Journal of Materials Processing Technology,* vol. 119, pp. 277-282, 2001.

[52] R. Neugebauer, R. Glass, M. Kolbe and M. Hoffman, "Optimisation of

processing routes for cross rolling and spin extrusion," *Journal of Materials Processing Technology,* Vols. 125-126, pp. 856-862, 2002.

[53] S. Winter, S. Fritsch and M. F. X. Wagner, "Microstructural evolution and mechanical properties of beta-titanium Ti-10V-2Fe-3Al during incremental forming," *Materials Processing and Interfaces,* vol. 1, pp. 833-840, 2012.

[54] R. Neugebauer, L. M. Meyer, T. Halle, M. Popp, S. Fritsch and C. John, "Manufacture of a beta-titanium hollow shaft by incremental forming," *Production Engineering Research Development,* vol. 5, pp. 227-232, 2011.

[55] M. M. Savarabadi, G. Faraji and E. Zalnezhad, "Hydrostatic tube cyclic expension extrusion (HTCEE) as a new severe plastic deformation method for producing long nanostructured tubes," *Journal of Alloys and Compounds,* vol. 785, pp. 163-168, 2019.

[56] M. Bodkhe, S. Sharma, A.-H. I. Mourad and P. B. Sharma, "A review on SPD processes used to produce ultrafine-grained and multilayer nanostructured tubes," *Materials Today: Proceedings,* 2021.

[57] G. Faraji, A. Babaei, M. M. Mashhadi and K. Abrinia, "Parallel tubular channel angular pressing (PTCAP) as a new severe plastic deformation method for cylindrical tubes," *Materials Letters,* vol. 77, pp. 82-85, 2012.

[58] H. Abdolvand, G. Faraji, J. S. Karami and M. Beniasadi, "Microstructure and mechanical properties of fine-grained thin-walled AZ91 tubes processed by a novel combined SPD process," *Bulletin of Materials Science,* vol. 40, pp. 1471-1479, 2017.

[59] N. Sadasivan and M. Balasubramanian, "Severe plastic deformation of tubular materials - Process methodology and its influence on mechanical properties - A review," *Materials Today: Proceedings,* vol. 46, pp. 3460-3468, 2021.

[60] C. J. Luis Pérez, "On the correct selection of the channel die in ECAP processes," *Scripta Materialia,* vol. 50, no. 3, pp. 387-393, 2004.

[61] X. Che, Q. Wang, B. Dong, M. Meng and Z. Zhang, "Numerical and Experimental Analysis of Rotating Backward Extrusion as a New SPD Process," *Metals and Materials Internationals,* vol. 26, pp. 1786-1796, 2020.

[62] N. A. Koneva, N. A. Popova, L. N. Ignatenko, E. E. Pekarskaya, Y. R. Kolobov and E. V. Kozlov, "Structure of Grains and Internal Stress Fields in Ultrafine Grained Ni Produced by Severe Plastic Deformation," *NATO Science Series,* vol. 80, pp. 121-126.

[63] M. Ensafi, G. Faraji and H. Abdolvand, "Cyclic extrusion compression angular pressing (CECAP) as a novel severe plastic deformation method for producing bulk ultrafine grained metals," *Materials Letters,* vol. 197, pp. 12-16, 2017.

[64] H. Abdolvand, H. Sohrabi, G. Faraji and F. Yusof, "A novel combined severe plastic deformation method for producing thin-walled ultrafine grained

cylindrical tubes," *Materials Letters,* vol. 143, pp. 167-171, 2015.

[65] O. Renk and R. Pippan, "Saturation of Grain Refinement during Severe Plastic Deformation of Single Phase Materials: Reconsiderations, Current Status and Open Questions," *Material Transaction,* vol. 60, no. 7, pp. 1270-1282, 2019.

[66] R. Pippan, F. Wetscher, M. Hafok, A. Vorhauer and I. Sabirov, "The Limits of Refinement by Severe Plastic Deformation," *Advanced Engineering Materials,* vol. 8, no. 11, pp. 1046-1056, 2006.

[67] R. B. Figueiredo and T. G. Langdon, "Deformation mechanisms in ultrafine-grained metals with an emphasis on the Hall-Petch relationship and strain rate sensitivity," *Journal of Materials Research and Technology,* vol. 14, pp. 137-159, 2021.

[68] D. H. Shin, J.-J. Pak, Y. K. Kim and K.-T. K. Y.-S. Park, "Effect of pressing temperature on microstructure and tensile behaviour of low carbon steels processed by equal channel angular pressing," *Materials Science and Engineering: A,* vol. 323, pp. 409-415, 2002.

[69] V. N. Chuvil'deev, M. M. Myshlyaev, A. V. Nokhrin, V. I. Kopylov, Y. G. Lopatin, O. E. Pirozhnikova, A. V. Piskunov, A. V. Semenycheva and A. A. Bobrov, "Effect of the Severe Plastic Deformation Temperature on the Diffusion Properties of the Grain Boundaries in Ultrafine-Grained Metals," *Russian Metallurgy,* vol. 2017, no. 5, pp. 413-425, 2017.

[70] G. I. Raab, E. P. Soshnikova and R. Z. Valiev, "Influence of temperature and hydrostatic pressure during equal-channel angular pressing on the microstructure of commercial-purity TI," *Materials Science and Engineering: A,* Vols. 387-389, pp. 674-677, 2004.

[71] F. A. Mohamed, "A dislocation model for the minimum grain size obtainable by milling," *Acta Materialia,* vol. 51, no. 14, pp. 4107-4119, 2003.

[72] Y. T. Zhu, X. Z. Liao and X. L. Wu, "Deformation twinning in nanocrystalline materials," *Progress in Materials Science,* vol. 57, pp. 1-62, 2012.

[73] E. Bruder, P. Braun, H. ur Rehman, R. K. W. Marceau, A. S. Taylor, R. Pippan and K. Durst, "Influence of solfute effects om the saturation grain size and rate sensitivity in Cu-X alloys," *Scripta Materialia,* vol. 144, pp. 5-8, 2018.

[74] Y. Cao, S. Ni, X. Liao, M. Song and Y. Zhu, "Structural evolutions of metallic materials processed by severe plastic deformation," *Materials Science and Engineering: R,* vol. 133, pp. 1-59, 2018.

[75] X. N. An, S. D. Wu, Z. G. Wang and Z. F. Zhang, "Significance of stacking fault energy in bulk nanostructured materials: Insights from Cu and its binary alloys as model systems," *Progress in Materials Science,* vol. 101, pp. 1-45, 2019.

[76] Y. Zhang, N. R. Tao and K. Lu, "Effects of stacking fault energy, strain rate and temperature on microstructure and strength of nanostructured Cu–Al

alloys subjected to plastic deformation," *Acta Materialia,* vol. 59, no. 15, pp. 6048-6058, 2011.

[77] Y. Iwahashi, Z. Horita, M. Nemoto and T. G. Langdon, "Factors influencing the equilibrium grain size in equal-channel angular pressing: Role of Mg additions to aluminium," *Metallurgical and Materials Transaction: A,* vol. 29, pp. 2503-2510, 1998.

[78] H. J. Roven, H. Nesboe, J. C. Werenskiold and T. Seibert, "Mechanical properties of aluminium alloys processed by SPD: Comparison of different alloy systems and possible product areas," *Materials Science and Engineering: A,* Vols. 410-411, pp. 426-429, 2005.

[79] I. J. Beyerlein and L. S. Toth, "Texture evolution in equal-channel angular extrusion," *Progress in Materials Science,* vol. 54, pp. 427-510, 2009.

[80] V. Tavakkoli, M. Afrasiab, G. Faraji and M. M. Mashhadi, "Severe plastic anisotropy of high-strength ultrafine grained Cu-Zn tubes processed by parallel tubular channel angular pressing (PTCAP)," *Materials Science and Engineering: A,* vol. 625, pp. 50-55, 2015.

[81] G. G. Yapici, I. J. Beyerlein, I. Karaman and C. N. Tomé, "Tension-compression asymmetry in severely deformed pure copper," *Acta Materialia,* vol. 55, no. 14, pp. 4603-4613, 2007.

[82] J. Eckert, J. C. Holzer, C. E. Krill III and W. L. Johnson, "Structural and thermodynamic properties of nanocrystalline fcc metals prepared by mechanical attrition," *Journal of Materials Research,* vol. 7, no. 7, pp. 1751-1761, 1992.

[83] S. Qu, X. H. An, H. J. Yang, C. X. Huang, G. Yang, Q. S. Zang, Z. G. Wang, S. D. Wu and Z. F. Zhang, "Microstructural evolution and mechanical properties of Cu-Al alloys subjected to equal channel angular pressing," *Acta Materialia,* vol. 57, no. 5, pp. 1586-1601, 2009.

[84] I. E. Volokitina, "Evolution of the Microstructure and Mechanical Properties of Copper under ECAP with Intense Cooling," *Metal Science and Heat Treatment,* vol. 62, pp. 253-258, 2020.

[85] O. Renk, P. Ghosh, R. K. Sabat, J. Eckert and R. Pippan, "The role of crystallographic texture on mechanically induced grain boundary migration," *Acta Materialia,* vol. 200, pp. 404-416, 2020.

[86] T. Sakai, A. Belyakov, R. Kaibyshev, H. Miura and J. J. Jonas, "Dynamic and post-dynamic recrystallization under hot, cold and severe plastic deformation conditions," *Progress in Materials Science,* vol. 60, pp. 130-207, 2014.

[87] C. J. Barr and K. Xia, "Grain refinement in low SFE and particle-containing nickel aluminium bronze during severe plastic deformation at elevated temperatures," *Journal of Materials Science and Technology,* vol. 82, pp. 57-68, 2021.

[88] O. F. Higuera and J. M. Cabrera, "Microstructure influencing physical and mechanical properties of electrolytic tough pitch copper produced by equal channel angular pressing," *Mechanics of Materials,* vol. 67, pp. 9-14, 2013.

[89] R. Z. Valiev, I. V. Alexandrov, N. A. Enikeev, M. Y. Murashkin and I. P. Semenova, "Towards enhancement of properties of UFG metals and alloys by grain boundary engineering using SPD processing," *Reviews on Advanced Materials Science,* vol. 25, no. 1, pp. 1-10, 2010.

[90] H. Liu, W. Pantleon and L. J. Mishnaevsky, "Non-equilibrium grain boundaries in titanium nanostructured by severe plastic deformation: Computational study of sources of material strengthening," *Computational Materials Science,* vol. 83, pp. 318-330, 2014.

[91] J. A. Munoz, R. E. Bolmaro, A. Moreira Jorge, A. Zhilyaev and J. M. Cabrera, "Prediction of Generation of High- and Low-Angle Grain Boundaries (HAGB and LAGB) During Severe Plastic Deformation," *Metallurgical and Materials Transaction: A,* vol. 51, pp. 4674-4684, 2020.

[92] X. Zeng, X. G. Fan, H. W. Li, M. Zhan, S. H. Li, K. Q. Wu and T. W. Ren, "Heterogeneous microstructure and mechanical property of thin-walled tubular part with cross inner ribs produced by flow forming," *Materials Science and Engineering: A,* vol. 790, p. 139702, 2020.

[93] C. C. Wong, T. A. Dean and J. Lin, "A review of spinning, shear forming and flow forming processes," *International Journal of Machine Tools and Manufacture,* vol. 43, pp. 1419-1435, 2003.

[94] D. Marini, D. Cunningham, P. Xirouchackis and J. R. Corney, "Flow forming: a review of research methodologies, prediction models and their applications," *International Journal of Mechanical Engineering and Technology,* vol. 7, no. 5, pp. 285-315, 2016.

[95] X. X. Wang, M. Zhan, M. W. Fu, P. F. Gao, J. Guo and F. Ma, "Microstructure evolution of Ti-6Al-2Zr-1Mo-1V alloy and its mechanism in multi-pass flow forming," *Journal of Materials Processing Technology,* vol. 261, pp. 86-97, 2018.

[96] H. R. Molladavoudi and F. Djavanroodi, "Experimental study of thickness reduction effects on mechanical properties and spinning accuracy of aluminum 7075-O, during flow forming," *The International Journal of Advanced Manufacturing Technology ,* vol. 52, pp. 949-957, 2011.

[97] Y. Zhang, F. Wang, J. Dong, L. Jin, C. Liu and W. Ding, "Grain refinement and orientation of AZ31B magnesium alloy in hotflow forming under different thickness reductions," *Journal of Materials Science and Technology,* vol. 34, pp. 1091-1102, 2018.

[98] G. Xiao, Q. Xia and X. Cheng, "Research on the grain refinement method of cylindrical parts by power spinning," *The International Journal of Advanced*

Manufacturing Technology, vol. 78, pp. 971-979, 2015.

[99] D. Tsivoulas, G. Timar, M. Tuffs, J. Quinta da Fonseca and M. Preuss, "Texture Formation in Flow Formed Ferritic Steel Tubes and the Influence of the Process Parameters," *Materials Science Forum,* Vols. 783-786, pp. 2602-2607.

[100] M. S. Mohebbi and A. Akbarzadeh, "Accumulative spin-bonding (ASB) as a novel SPD process for fabrication of nanostructured tubes," *Materials Science and Engineering: A,* vol. 528, pp. 180-188, 2010.

[101] M. Zhan, X. Wang and H. Long, "Mechanism of grain refinement of aluminium alloy in shear spinning under different deviation ratios," *Materials and Design,* vol. 108, pp. 207-216, 2016.

[102] A. Ghiotti, M. Brun, E. Simonetto, S. Bruschi and G. Muffato, "Insights in Strain and Stress States of Conical Shapes Flow Forming," *Procedia Manufacturing,* vol. 47, pp. 335-341, 2020.

[103] K. Xue, L. Yan and Z. Xianming, "A study of the rotational matching relationship amongst technical parameters in stagger spinning," *Journal of Materials Processing Technology,* vol. 69, pp. 167-171, 1997.

[104] Y. Xu, S. H. Zhang, P. Li, K. Yang, D. B. Shan and Y. Lu, "3D rigid-plastic FEM numerical simulation on tube spinning," *Journal of Materials Processing Technology,* vol. 113, pp. 710-713, 2001.

[105] M. Sivanandini, S. S. Dhami and B. S. Pabla, "Flow Forming of Tubes - A Review," *International Journal of Scientific and Engineering Research,* vol. 3, 2012.

[106] R. J. Bhatt and H. Raval, "Comparative Study of Forward and Backward Flow Forming Process using Finite Element Analysis," *Bonfring International Journal of Industrial Engineering and Management Science,* vol. 5, pp. 46-50, 2015.

[107] L. Yuebing, W. Fang, C. Lu, Z. Gao, X. Ma, W. Jin, Y. Ye and F. Wang, "Microstructure and Mechanical Properties of 34CrMo4 Steel for Gas Cylinders Formed by Hot Drawing and Flow Forming," *Materials,* vol. 12, no. 8, pp. 1351-1364, 2019.

[108] Q. Xia, G. Xiao, H. Long, X. Cheng and B. Yang, "A study of manufacturing tubes with nano/ultrafine grain structures by stagger spinning," *Materials and Design,* vol. 59, pp. 516-523, 2014.

[109] V. Bedekar, P. Pauskar, R. Shivpuri and J. Howe, "Microstructure and texture evolutions in AISI 1050 steel by flow forming," *Procedia Engineering,* vol. 81, pp. 2355-2360, 2014.

[110] S. Mizunuma, "Large Straining Behavior and Microstructure Refinement of Several Metals by Torsion Extrusion Process," *Materials Science Forum,* Vols. 503-504, pp. 185-192, 2006.

[111] Z. Cao, F. Wang, Q. Wan, Z. Zhang, L. Jin and J. Dong, "Microstructure and

mechanical properties of AZ80 magnesium alloy tube fabricated by hot flowforming," *Materials and Design,* vol. 67, pp. 64-71, 2015.

[112] F. A. Hua, Y. S. Yang, Y. N. Zhang, M. H. Gu, W. H. Tong and Z. Q. Hu, "Three-dimensional finite element analysis of tube spinning," *Journal of Materials Processing Technology,* vol. 168, pp. 68-74, 2005.

[113] X. Wang, P. Gao, M. Zhan, K. Yang, Y. Dong and Y. Li, "Development of microstructural inhomogeneity in multi-pass flow forming of TA15 alloy cylindrical parts," *Chinese Journal of Aeronautics,* vol. 33, pp. 2088-2097, 2020.

[114] R. J. Bhatt and H. Raval, "Influence of Operating Variables During Flow Forming Process," *Procedia CIRP,* vol. 55, pp. 146-151, 2016.

[115] M. H. Parsa, A. M. A. Pazooki and M. N. Ahmadabadi, "Flow-forming and flow formability simulation," *The International Journal of Advanced Manufacturing Technology,* vol. 42, 2009.

[116] N. Kim, H. Kim and K. Jin, "Minimizing the Axial Force and the Material Build-up in the Tube Flow Forming Process," *International Journal of Precision Engineering and Manufacturing,* vol. 14, pp. 259-266, 2013.

[117] N. A. Razani, A. J. Aghchai and B. M. Dariani, "Flow-forming optimization based on hardness of flow-formed AISI321 tube using response surface method," *The International Journal of Advanced Manufacturing Technologies,* vol. 70, pp. 1463-1471, 2014.

[118] M. Srinivasulu, M. Komaraiah and S. K. P. Rao, "Experimental studies on the characteristics of AA6082 flow formed tubes," *Journal of Mechanical Engineering Research,* vol. 4, pp. 192-198, 2012.

[119] H. Shinde, P. Mahajan, A. K. Singh, R. Singh and K. Narasimhan, "Process modeling and optimization of the staggered backward flow forming process of maraging steel via finite element simulations," *The International Journal of Advanced Manufacturing Technology,* vol. 87, pp. 1851-1864, 2016.

[120] T. Magro, A. Ghiotti, S. Bruschi and E. Simonetto, "Accuracy in microstructure measurements in highly directional processes," 2021.

[121] G. F. Vander Voort, "Examination of Some Grain Size Measurement Problems," in *Metallography Past, Present and Future (75th Anniversary Volume) ASTM STP 1165*, A. S. f. T. a. Materials, Ed., Philadelphia, G. F. Vander Voort; F. J. Warmuth; S. M. Purdy; A. Szirmae, 1993, pp. 266-294.

[122] G. F. Vander Voort, "Grain Size Measurement," in *ASTM STP 839*, A. S. f. T. a. Materials, Ed., Philadelphia, Steel, J. and McCall, J., 1984, pp. 85-131.

[123] G. F. Vander Voort, "Grain size measurements by the triple point count method," *Practical Metallography,* vol. 51, no. 3, pp. 201-207, 2014.

[124] E. Heyn, "Short reports from the metallurgical laboratory of the Royal Mechanical and Testing Institute of Charlottenburg," *The Metallographist,* vol.

5, pp. 39-64, 1903.

[125] J. Hilliard, "Specification and measurement of microstructural anisotropy," *Transaction AIME,* vol. 224, pp. 1201-1212, 1962.

[126] J. E. Hilliard, "Estimating grain size by the intercept method," *Metal Progress,* vol. 85, 1964.

[127] H. Abrams, "Grain size measurements by the intercept method," *Metallography,* vol. 4, pp. 59-78, 1971.

[128] Z. Jeffries, A. H. Kline and E. B. Zimmer, "The determination of the average grain size in metals," *Transactions, American Institute of Mining and Metallurgical Engineers,* vol. 54, pp. 594-607, 1917.

[129] T. Magro, A. Ghiotti and S. Bruschi, "Manufacturing thin-walled 99.99% pure Zn tubes with ultrafine grained structures by flowforming," *Procedia Manufacturing,* vol. 50, pp. 337-344, 2020.

[130] R. Z. Valiev, R. K. Islamgaliev and I. V. Alexandrov, "Bulk nanostructured materials from severe plastic deformation," *Progress in Materials Science,* vol. 45, pp. 103-189, 2000.

[131] *Standard Test Methods for Determining Average Grain Size,* West Conshohocken, Pennsylvania: ASTM International, 2010.

[132] M. Naito, T. Yokoyama, K. Hosokawa and K. Nogi, "Evaluation Methods for Properties of Nanostructured Body," in *Nanoparticle Technology Handbook*, Elsevier, 2018, pp. 301-363.